Single molecule tracking with light sheet microscopy

Dissertation zur Erlangung des Grades
Doktor der Naturwissenschaften (Dr. rer. nat.)

vorgelegt von

Jörg Ritter

Institut für Physikalische und Theoretische Chemie
Mathematisch-Naturwissenschaftliche Fakultät der
Rheinischen Friedrich-Wilhelms-Universität
Vorgelegt von Jörg Ritter aus Wolfsberg, AUT

Bonn, März 2011

Diese Arbeit wurde mit Genehmigung der
Mathematisch-Naturwissenschaftlichen Fakultät
der Rheinischen Friedrich-Wilhelms-Universität Bonn angefertigt.

Erstgutachter: Prof. Dr. Ulrich Kubitscheck
Zweitgutachter: Prof. Dr. Rudolf Merkel

Tag der mündlichen Prüfung: 19.07.2011
Erscheinungsjahr: 2011

IN DER DISSERTATION EINGEBUNDEN:

Zusammenfassung

Für meine Familie

Summary

The work presented here concentrates on light sheet based fluorescence microscopy (LSFM) and its application to single molecule tracking.

In LSFM the sample is illuminated perpendicular to the detection axis with a thin light sheet. In this manner a simple optical sectioning microscope is created, because only the focal plane of the detection optics is illuminated and no out-of-focus fluorescence is generated. This results in an enhancement of the signal-to-noise-ratio and combined with the high acquisition speed of a video microscopy a powerful tool is created to study single molecule dynamics on a millisecond timescale,

A completely new setup was designed and constructed, that combines light sheet illumination technique with single molecule detection ability. Theoretical calculations and quantitative measurements of the illumination light sheet thickness (2-3 µm thick) and the microscope point spread function were performed. A direct comparison of LSFM and epi-illumination of model samples with intrinsic background fluorescence illustrated the clear contrast improvement of LSFM for thick samples.

Single molecule detection is limited by the number of photons emitted by a single fluorophore per observation time. So, the ability to track single molecules is dependent on molecule speed, background, detection sensitivity and frame rate. The imaging speed with the concomitant high signal-to-noise ratio that could be realized within the setup was unprecedented until then. It permitted the observation of single protein trajectories in aqueous solution with a diffusion coefficient greater than 100 µm²/s. The *in vivo* imaging of single molecules in thick biological samples was demonstrated in living salivary gland cell nuclei of *Chironomus tentans* larvae. These cell nuclei afford exceptional possibilities for the study of RNA mobility, but provide a microscopic challenge with a diameter of 50-75 µm and up 200 µm deep within the sample. To image the intranuclear mobility of individual messenger RNA particles, they were indirectly labeled via the fluorescently labeled RNA binding protein hrp36. Thus it was possible to identify at least three different diffusion modes of the mRNA particles and indirectly measure the nuclear viscosity.

A high flexibility and easy adaptation of the optical sectioning thickness is required to visualize biological samples of various sizes. Often, however, the sheet geometry is fixed, whereas it would be advantageous to adjust the sheet geometry to specimens of different dimensions. Therefore, an afocal cylindrical zoom lens system comprising only 5 lenses and a total system length of less than 160 mm was developed. Two movable optical elements were directly coupled, so that the zoom factor could be

adjusted from 1x to 6.3x by a single motor. Polytene chromosomes of salivary gland cell nuclei of C.tentans larvae were imaged in vivo to demonstrate the advantages in image contrast by imaging with different light sheet dimensions.

The light sheet microscope introduced in this thesis proofed its suitability for *in vivo* single molecule imaging deep within a biological sample. It has the potential to reveal new dynamic single molecule interactions *in vivo* and enables new studies and experiments of intracellular processes.

Publications

The results presented in this thesis have previously been published:

Articles

(1) **J.G. Ritter**, J.H. Spille and Ulrich Kubitscheck (2011) *A cylindrical zoom lens for adjustable optical sectioning thickness in light sheet based microscopy.* Biomedical Optics Express 2(1): 185-193

(2) **J.G. Ritter**, R.Veith, A. Veenendaal, J.-P. Siebrasse and U. Kubitscheck (2010) *Light Sheet Microscopy for single molecule tracking in living tissue*. PLoS ONE 5(7): 11639

(3) **J.G. Ritter**, R. Veith, J. P. Siebrasse and U. Kubitscheck (2008) *High-contrast single-particle tracking by selective focal plane illumination microscopy*. Optics Express 16(10): 7142-52

Book chapter

(1) U. Kubitscheck, R. Veith, **J.G. Ritter**, and J.-P. Siebrasse. Messenger-RNA Trafficking in Living Cells. In "Single Particle Tracking and Single Molecule Energy Transfer: Applications in the Bio and Nano Sciences", eds. C. Bräuchle, J. Michaelis, D.C. Lamb. 2009 Wiley-VCH, Weinheim

Invited talk

(1) **J.G. Ritter**. *In vivo single molecule tracking with Selective focal Plane Illumination Microscopy (SPIM)*. 23.03.2009 National Institute of Health, Washington D.C. USA

Conference platform presentations

(1) **J.G. Ritter**, Jan-Hendrik Spille, Eugen Baumgart and Ulrich Kubitscheck *Adjustable light-sheet dimensions produced by a cylindrical zoom lens.* The Second Light Sheet based Fluorescence Microscopy Workshop, 28.06. – 01.07.2010 Dublin, Ireland

(2) **J.G. Ritter**, J.H. Spille, R. Veith, J.-P. Siebrasse and U. Kubitscheck *Single molecule imaging with light sheet-based microscopy in living tissue.* Microscience 2010, 28.06. – 01.07.2010 London, Großbritannien

(3) **J.G. Ritter**, R. Veith, J.-P. Siebrasse und U. Kubitscheck. *In vivo single molecule tracking with light sheet-based microscopy.* Focus on Microscopy, 05. – 08.04.2009 Krakau, Polen

(4) **J.G. Ritter**, R. Veith, J.-P. Siebrasse und U. Kubitscheck. *Single molecule tracking with light sheet-based microscopy in vivo.* 53rd Annual Meeting of the Biophysical Society, 28.02. – 04.03.2009 Boston (MA), USA. Biophys. J. 2009. 96(3):17a

(5) **J.G. Ritter**, R. Veith und U. Kubitscheck. *High-Contrast single molecule microscopy by selective focal plane illumination.* Workshop on Cell Biology & Microscopy, 02. – 06.06.2008 Altleiningen

(6) **J.G. Ritter**, R. Veith und U. Kubitscheck. *High-Contrast single molecule microscopy by selective focal plane illumination.* 52nd Annual Meeting of the Biophysical Society, 02. – 06.02.2008 Long Beach (CA), USA. Biophys. J. Supp. 2008, 94:2661

Poster presentations

(1) **J.G. Ritter**, T. Kaminski, J.H. Spille, R. Veith, J.P. Siebrasse and U. Kubitscheck. *Light sheet microscopy for single molecule imaging in living tissue.* Annual meeting of the German biophysical society. 03. – 06.10.2010 Bochum, Germany

(2) **J.G. Ritter**, W. Wendler and U. Kubitscheck. *Single molecule microscopy using focal plane illumination*. Focus on Microscopy 10. – 14.04.2007 Valencia, Spanien

(3) **J.G. Ritter**, W. Wendler and U. Kubitscheck. *Single molecule microscopy using focal plane illumination*. Frühjahrstagung der Deutschen Physikalischen Gesellschaft. 26. – 30.03.2007 Regensburg

(4) **J.G. Ritter**, W. Wendler and U. Kubitscheck. *Single molecule microscopy using focal plane illumination*. Optical Analysis of Biomolecular Machines. 13. – 16.06.2006 Max-Delbrück Center, Berlin

Coauthored conference abstracts

(1) J.H. Spille, **J.G. Ritter**, T. Kaminski and U. Kubitscheck. *3D tracking of single fluorescent molecules with astigmatic imaging of a light sheet illuminated sample*. Annual meeting of the German biophysical society. 03. – 06.10.2010 Bochum, Germany

(2) T. Kaminski, J.P. Siebrasse, **J.G. Ritter** and U. Kubitscheck. *Imaging Export of Single Native mRNP Particles in Live Cells.* Annual meeting of the German biophysical society. 03. – 06.10.2010 Bochum, Germany

(3) J.H. Spille, **J.G. Ritter** and U. Kubitscheck. *Light sheet based microscopy for 3D single particle tracking*. EMBO Workshop Advances Light Microscopy 10th International ELMI Meeting. 18.05. – 21.05.2010 EMBL Heidelberg

(4) **J.G. Ritter**, R.Veith, J.P. Siebrasse und U. Kubitscheck. *Real-time observation of single, native mRNA molecules in living tissue by LSFM*. The First Light Sheet based Fluorescence Microscopy Workshop. 24.09. – 25.09.2009 MPI-CBG in Dresden

(5) J.P. Siebrasse, **J.G. Ritter**, R. Veith, B. Daneholt und U. Kubitscheck. *Exploring the nuclear export of single native mRNP particles in living cells*. EMBO Conference Series on Nuclear Structure and Dynamics. 30.09. – 04.10.2009 L'Isle sur la Sorgue, Frankreich

(6) R. Veith, **J.G. Ritter**, J.-P. Siebrasse, A. Dobay, H. Leonhardt, B. Danhold and U. Kubitscheck. *Discontinuous movement of mRNPs in nucleoplasmic regions devoid* of chromatin. 53rd Annual Meeting of the Biophysical Society, 28.02. – 04.03.2009 Boston (MA), USA

(7) J.P. Siebrasse, **J. G. Ritter**, R. Veith and U. Kubitscheck. *Single-molecule microscopy and SPIM of single nanoparticles and mRNA molecules in vivo.* Focus on Microscopy. 13. – 16.04.2008 Osaka-Awaji, Japan

(8) R. Veith, **J.G. Ritter**, J.-P. Siebrasse and U. Kubitscheck. *In-vivo Analysis of Intranuclear Nanoparticle Movement using FPIM*. 20th Wilhelm Bernhard Workshop: International conference on the cell nucleus. 27. – 31.08.2007 St. Andrews, Schottland

Contents

Abbreviations

AOTF	Acousto optical tunable filter
BR	Balbiani ring
BSA	Bovine serum albumin
CCD	Charged coupled device
DIC	Differential interference contrast
DSLM	Digital scanned light sheet microscopy
DSLM-SI	DSLM - structured illumination
DTT	Dithiothreitol
EGTA	Ethylene glycol tetraacetic acid
EMCCD	Electron multiplying CCD
FCS	Fluorescence correlation spectroscopy
FWHM	Full width at half maximum
GFP	Green fluorescent protein
HEPES	4-(2-hydroxyethyl)-1-piperazineethanesulfonic acid
HILO	Highly inclined laminated sheet optic
LSFM	light sheet based fluorescence microscopy
mRNA	messenger ribonucleic acid
mRNP	messenger ribonucleoprotein particles
MW	Molecular weight
MSD	Mean square displacement
MVR	Multi view reconstruction
NA	Numerical aperture
OCPI	Objective coupled planar illumination
PALM	Photoactivated localization microscopy
PBS	Phosphate buffered saline
PSF	Point spread function
ReAsH	biarsenical dye 4,5-bis(1,3,2-dithiarsolan-2-yl)resorufin
SMT	Single molecule tracking
SNR	Signal to noise ratio
SPIM	Selective plane illumination microscopy
STED	Stimulated emission depletion
STORM	stochastic optical reconstruction microscopy
TIRF	Total internal reflection fluorescence

1 Introduction

''One picture is worth ten thousand words''

Advertisement for the use of pictures
in advertisements on streetcars, Fred R. Barnad (1927)

Sight is regarded as the single most important channel through which the human mind perceives its surrounding world. For the human being the visual sense is of greatest importance since it is its guiding sense and allows a secure orientation in the world. It seems to be such an important source of information, that objects are often not considered existent unless they can be visualized. "I won't believe it till I see it" is a common phrase and therefore it is no wonder that imaging techniques which provide a picture of the object under investigation are key tools for the sciences. The researchers wish for visualizing the objects of study, whether galaxies light years away or crystalline structures composed of single atoms, inspired over centuries the development of imaging instruments like space telescopes or electron microscopes. Nowadays especially in the life sciences optical microscopy techniques are successfully used and well established, due to the fact that they permit studying of live specimens in a non-invasive and non-destructive way.

1.1 Challenges in optical microscopy

The image quality in optical microscopy is dependent on numerous parameters. An important evaluation criterion in optical microscopy is the resolution, not only in terms of image characterization but also to compare different microscopy techniques. In general the overall performance of the microscope is determined by three major factors: (1) Used light wavelengths to illuminate the sample, but also the wavelength the microscope detects in response upon illumination of the sample. (2) The imaging technique and the optics used. (3) The imaged sample itself.

An easy method to increase resolution is to use shorter wavelengths, but the optics and imaging techniques used certainly have a bigger influence. For centuries the resolution has been limited by the diffraction barrier with an achievable lateral resolution of d_{xy} ~250 nm for optical microscopy [1].

$$d_{xy} = \frac{0.61\lambda_0}{NA} \qquad , NA = n \sin \alpha \tag{1.1}$$

λ_0 is the wavelength, and NA the numerical aperture with n the refractive index and α half the opening angle of the objective.
With modern microscopy techniques, e.g. stimulated emission depletion microscopy (STED) [2] or stochastic optical reconstruction microscopy (STORM) [3], it became possible to circumvent the diffraction barrier and to achieve resolutions down to only a few nanometers. However, the influence of the sample itself is often underestimated. The properties of the observed specimen, in particular in biology, can severely limit the achievable resolution. So the resolution of a microscope is heavily dependent on the homogeneity of the sample. For inhomogeneous samples refractive index changes or light scattering cause a degradation of resolution. The overall resolution of an instrument is therefore often worse than the theoretically calculated resolution where only the factors (1) and (2) are considered. These effects severely increase for higher penetration depths. Generally for imaging large samples, resolution and penetration depth are not independent of each other and have to be finely balanced.

Even though it is obvious that high resolution is worth to strive for, it is by far not the only important characteristic of a microscope. The signal-to-noise-ratio (SNR) is also crucial for the quality of a measurement and the performance of a system. In general the SNR represents the ratio of the measured light signal above background I_{Signal} to the combined noise σ_{Total} [1].

$$SNR = \frac{I_{Signal}}{\sigma_{Total}} \tag{1.2}$$

The noise σ_{Total} is due to inherent statistical variation of the incident photon flux $\sigma_{\mathrm{Fluorescence}}$, statistically varying background fluorescence $\sigma_{\mathrm{Background}}$, or consists of undesirable signal components arising in the microscopic system such as read-out noise of the used photon detector $\sigma_{\mathrm{Detector}}$ [1].

$$\sigma_{Total} = \sqrt{\sigma^2_{Fluorescence} + \sigma^2_{Background} + \sigma^2_{Detector}} \tag{1.3}$$

The SNR is influenced by the same major factors as the resolution and therefore control of the SNR is not easily achieved. For example, at the first glance in fluorescence microscopy more fluorescent markers at the observed structures lead to more signal photons, but the background signal from out-of-focus fluorophores might increase as well. In the worst case, no structures can be discriminated and only homogenous background is visualized. For this reason especially techniques, which provide an intrinsic optical sectioning effect have the capability to boost the signal-to-noise-ratio due to the reduction of background noise. Only a high signal-to-noise ratio allows the discrimination between dim and bright structures. Hence it is important to achieve the best signal-to-noise-ratio in each experiment.

1.2 Biological fluorescence microscopy

The practical use of a microscope is determined by both its physical parameters and its biocompatibility. The goal of light microscopy must be the provision of the ideal tool, in terms of resolution, contrast, speed, biocompatibility etc, to investigate a given (biological) problem. An increase in popularity of optical microscopy in the last thirty years is due to the advent of fluorescence microscopy. Fluorescence microscopy is well established in the life sciences, because it allows non-invasive and *in vivo* observation of specimens with an excellent image contrast.

The absorption and subsequent emission of light by organic and inorganic specimens is typically the result of well-established physical phenomena described as being either fluorescence or phosphorescence [4]. Fluorescence microscopy takes advantage of this phenomenon as a contrast technique. A structure of interest (e.g. protein, receptor) in the specimen is labeled specifically with a fluorescent molecule. Upon illumination with light of a specific wavelength the light is absorbed and re-emitted by the molecule with a longer wavelength. By spectral discrimination between excitation and emission light, the fluorescent molecule, and thus the structure of interest, can be visualized. In a properly configured microscope, only the emission light should reach the eye or detector so that the resulting fluorescent structures are superimposed with high contrast against a very dark (or black) background.

Fluorescent markers are usually the only interference in the biological system under examination. Genetically engineering allows the incorporation of fluorescent proteins, such as the green fluorescent protein (GFP), which is even less intrusive than labeling with artificial chemical fluorophores [1]. However, when looking at live specimens with light at high intensities the impact of light on the sample is crucial. Heating and photo-toxicity can easily damage the sample or lead to abnormal behavior. Light induced photo-destruction can result in free radicals, which might kill living cells within seconds [1,5]. Additionally, when looking at fluorescent markers, intensive excitation has a destructive effect on the fluorophores, which ultimately results in a permanent loss of signal. This photochemical destruction of the fluorophore, called photo-bleaching, is especially problematic in time-lapse imaging, where the observation time is limited by the life time of the fluorophore. In consequence the photon load on the sample should be minimized by using only the minimal necessary excitation intensity and imaging techniques which avoid unnecessary photon exposure should be preferred. However, some microscope techniques take advantage of photo-bleaching. For instance, fluorescence recovery after photo-bleaching (FRAP)[6] exploits the effect to reveal the dynamics of single molecules.

For some fixed specimens high resolution might be the ultimate goal, if acquisition speed and possible photo-bleaching are of minor interest. But for many applications, in particular dynamic studies *in vivo*, the microscope has to meet challenging demands. Live specimens are dynamic systems, and the image acquisition speed in terms of frames per second (fps) of the microscope has to keep up with the processes under investigation. But the number of collected signal photons N is proportional to the exposure time t_{Exposure} and thus inverse proportional to the acquisition speed.

$$SNR \propto N \propto t_{Exposure} \propto \frac{1}{fps} \tag{1.3}$$

Since a higher acquisition speed automatically results in a reduced signal-to-noise-ratio both parameters have to be finely tuned to achieve the desired result. For example, imaging the dynamics of single molecules requires the microscope to collect a high amount of fluorescent photons to locate the molecules as precisely as possible at a high acquisition speed. The 2D-localization precision can be formulated as [7],

$$\sigma_{2D-\mathrm{Pr}ecision} = \sqrt{\frac{s^2}{N} + \frac{a^2}{12N} + \frac{8\pi s^4 b^2}{a^2 N^2}} \tag{1.4}$$

where s is the standard deviation of the point-spread function, a the pixel size, b the standard deviation of the background and N the total number of photons contributing to a signal.

Reducing the exposure time for an increased acquisition speed automatically results in fewer detected photons and a trade-off between acquisition speed and localization precision exists. In order to keep the photon count constant at higher acquisition speeds, the illumination power could be increased; thereby the number of emitted photons would remain constant. But higher illumination intensity is not always an option since it increases photo-bleaching and photo-toxicity or might lead to fluorophore saturation.

Investigating biological specimens under the microscope has its own special pitfalls. Biological specimens are inhomogeneous, strongly scatter light and usually emit autofluorescence upon illumination, which is a major source of unwanted background. Matters get worse for imaging deep inside structures. The achievable resolution and signal strengths degrade with increasing penetration depth. Therefore imaging deep inside a specimen is a real challenge but desirable since three dimensional information is indispensable for an accurate measurement of biologic relevant processes.

Obviously biological specimens develop and grow in all three dimensions and can rarely be considered as flat, two dimensional objects. But this is exactly the limitation a lot of microscope users have to accept, because all imaging techniques require the user

to mount the specimen in some appropriate way with respect to the microscope and its objective lens. This demands often to prepare the sample on hard glass cover slips introducing an unnatural boundary to a living specimen. For larger objects it might be even necessary to cut and destroy the specimen and prepare two-dimensional slices to observe the region of interest. It is a compromise between the possibility to observe a certain phenomenon or specimen at all and confining the specimen on an unnatural two-dimensional surface, therefore altering its physiology. This might lead to investigating an artificial biology. Even though it might have no effect on most studies, it can result in producing artifacts and the influence of the preparation method on the biological system under investigation has to be checked for each new experiment. Even in a more basic system like genetically identical cultured cells the culture conditions, such as the growth on flat hard surfaces, have a profound effect on the physiology of the cell [8]. Thus it has been shown, that cells from three dimensional multi-cellular organisms are very distinct in terms of their biological activity [9] [10]. For these reasons three-dimensional mounting procedures are becoming increasingly popular. Three dimensional mounting and investigation of the sample should provide conditions closer to physiological conditions and lead to results better representing reality.

1.3 Motivation of this thesis

From the variety of applications for biological fluorescence microscopy the visualization of a single bio-molecule is one of the most challenging, but also one of the most rewarding. Imaging individual molecules *in vivo* is the way to directly see the behavior of bio-molecules influenced by the interaction with their molecular proximate and the native environment. It allows the observation of native processes such as viral infections of cells [11], receptor binding on cell surfaces [12] or protein-DNA interactions [13] with high spatial resolution. Unraveling complex biological processes at the single molecule level in multi-cellular organisms is an even more demanding challenge, but essential to deepen our understanding of life.

Single molecule tracking (SMT) is the observation of the motion of individual molecules within a medium over time. The set of coordinates of a certain molecule over a series of time steps is referred to as trajectory. The information obtained from this trajectory can then provide useful information for understanding the mechanisms that drive and constrain the molecular motions [14]. Other single molecule techniques such as fluorescence correlation spectroscopy (FCS) [15] provide only information about the ensemble average of many molecules. SMT instead reveals the eventual presence of different types of diffusion behavior within each single trajectory. Given a sufficient time resolution, SMT has the ability to observe intermediate states or rare events of physiological processes. Thus it is possible to visualize the time evolution of processes and to show e.g. the sequence of events a single molecule undergoes in its pathway.

This time resolved observation can yield essential clues to unravel the mechanisms causing for example subdiffusion in complex environments. This is a direct consequence of the fact that single molecules can be localized with nanometer precision (see Eq. 1.4).

The real-time visualization of single molecule dynamics is difficult. Intrinsically weak fluorescent signals and fast moving molecules require a high detection sensitivity, combined with a high spatio-temporal resolution. Whereas *in vitro* SMT techniques have well been established as powerful biochemical tools that can reveal the dynamic nature of proteins and nucleic acids [16], the application of SMT *in vivo* is still limited. One major drawback is the low SNR, which is primarily caused by cellular autofluorescence. In spite of theses difficulties several techniques were developed, which were capable of *in vivo* imaging of single molecules in cells on the millisecond time scale [17,18].

To study processes as for example protein transport between cells or among cell organelles it is necessary to observe single molecules deep in living, intact, large biological objects such as tissue or embryos. The internal background fluorescence and heterogeneity of the three dimensionally extended specimen is simply so high, that it renders single molecule imaging exceedingly difficult [19,20]. At the same time, the observation time is often limited due to photo-bleaching of the marker fluorophore. This optically challenging situation can be tackled by applying clever illumination schemes, combining high-speed video microscopy with an optical sectioning effect.

Two techniques, total internal reflection fluorescence microscopy (TIRF) [21] and highly inclined laminated sheet microscopy (HILO)[22,23], fulfill these prerequisites of a high spatio-temporal resolution and an optical sectioning effect. In combination with an epi-detection both techniques are perfectly suitable for imaging and tracking of fast single molecule dynamics *in vivo* and have been successfully applied to it [19]. But both techniques have their own limitations, which make them unsuitable for single molecule tracking in intact, large biological objects in three dimensions. TIRF excites only a thin slice of the sample near the cover slip in an evanescent field close to the surface [24]. Because the evanescent field falls off exponentially within approximately 100 nm, TIRF is only applicable when the region of interest is very close the cover slip. In a variation called HILO (also colloquially referred to as “dirty-TIRF") a highly inclined beam exits the objective and illuminates the sample in a slice with a thickness of approximately 4-6 µm [22,23]. The applicable working distance for HILO is roughly 10 µm which is two magnitudes larger than in TIRF, but nevertheless not high enough to image deep inside larger biological specimens, such as tissue or embryos, where penetration depths of 100 µm and more are required. Hence, TIRF and HILO provide a highly selective

illumination and yield good signal-to-noise-ratios, but are restricted to excitation volumes close to the cover slip (**Figure 1.1**).

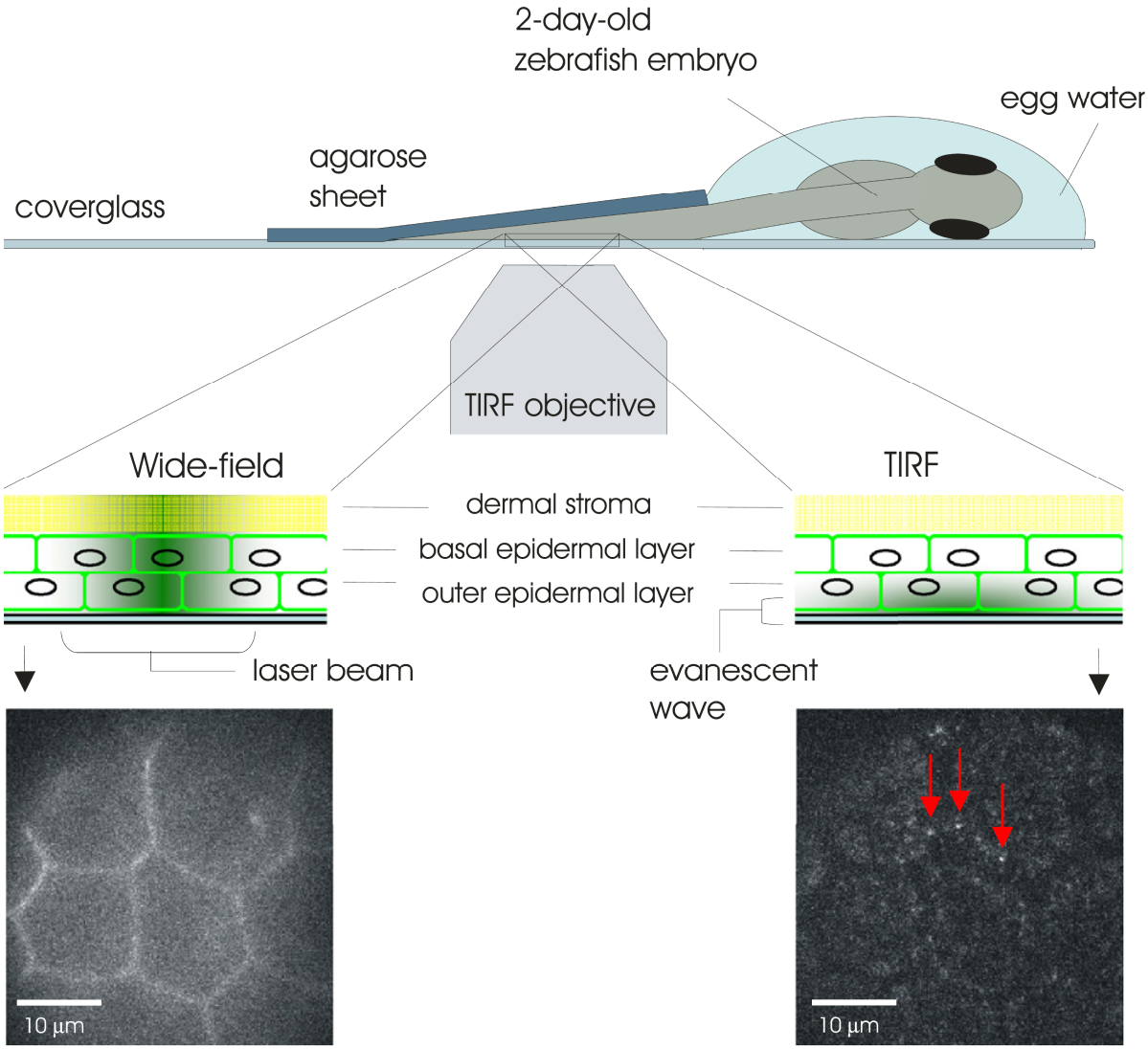

Figure 1.1 Single molecule imaging in living zebrafish. Single molecule microscopy in a living zebrafish embryo demonstrates the limitations of a wide-field and TIRF illumination. A zebrafish embryo was injected with YFP-C10H-Ras mRNA and placed on a coverslip in a drop of egg water. A sheet of agarose (0.75 mm thick) was placed over the embryo covering the tail region, and the coverslip was mounted on a microscopy setup suitable for wide-field and TIRF microscopy. In the left part of the figure, a wide-field microscopic image of the outer layer of the epidermis is shown, displaying membrane localization of the fluorescent signal. Due to the lack of an optical sectioning effect the internal background fluorescence was too high and no single YFP molecules could be visualized. On the right, the acquisition of an image of the same region by TIRF microscopy is shown. Individual YFP molecules (red arrows) were imaged, but the observation volume was limited to a region close to the cover slip. Sketch and parts of the figure legend from [19].

Apart from TIRF or HILO microscopy, light sheet microscopy provides another way to perform single molecule tracking *in vivo* with high spatio-temporal resolution. In light sheet microscopy the sample is illuminated perpendicular to the detection axis with a thin light sheet. In this manner an optical sectioning effect is created and can be combined with a fast and sensitive epi-detection. Light sheet microscopy provides efficient fluorescence excitation, reduced photo-bleaching and a high acquisition speed. These instrumental characteristics produce an improved contrast and allow very long observation times of sensitive samples, which makes light sheet microscopy presumably the ideal solution for single molecule tracking far away from the cover slip.

The goal of this thesis was to realize single molecule imaging and tracking in a light sheet microscope. Before the start of this thesis no such experimental setup existed. worldwide Existing light sheet microscopes lacked the required sensitivity (Chapter 1.5). Therefore, it was intended to design, build and evaluate a new light sheet microscope with the necessary sensitivity. The potential and limits of light-sheet single molecule microscopy should be explored, and finally it should be demonstrated that single molecule imaging with greatly improved contrast is feasible in living, three dimensionally extended biological samples.

1.4 Principle of light sheet microscopy

The basic idea behind light sheet based fluorescence microscopy (LSFM) is the combination of optical sectioning with wide-field detection by illuminating a single thin plane of the focal volume of the detection optics (**Figure 1.2a**). This sheet of light illuminates the complete lateral focal plane (xy-plane) of the detection optics in a direction perpendicular to the observation axis (z-axis), and only a thin section of it along the axial direction (z-axis). Illumination and detection light paths are completely separated from each other. The light sheet is a focused elliptically Gaussian beam [25] (**Figure 1.2b**, see chapter 2.4 for more details), whose focus is aligned to coincide with the focal plane of the detection optics. Thus, only signals in the overlapping region are detected and no out-of-focus fluorescence contributes to the image, which results in an optical sectioning effect (**Figure 1.2b**). Both light paths can have different numerical apertures and working distances. The sample region of interest is placed in the overlapping area of illumination and detection focus. Fluorescence excited in the illuminated focal plane is collected by the detection optics and imaged by a camera in a parallel manner. To change the region of interest, the sample is moved through the observation volume independently from the optics. By this means, three dimensional image stacks can be acquired. The thickness of the light sheet corresponds to its full-width-at-half-maximum (FWHM) extension along the z-axis, the height of the light sheet to its extension along the y-axis and the width along the x-axis is defined by the Rayleigh length of the illumination Gaussian beam (**Figure 1.2**).

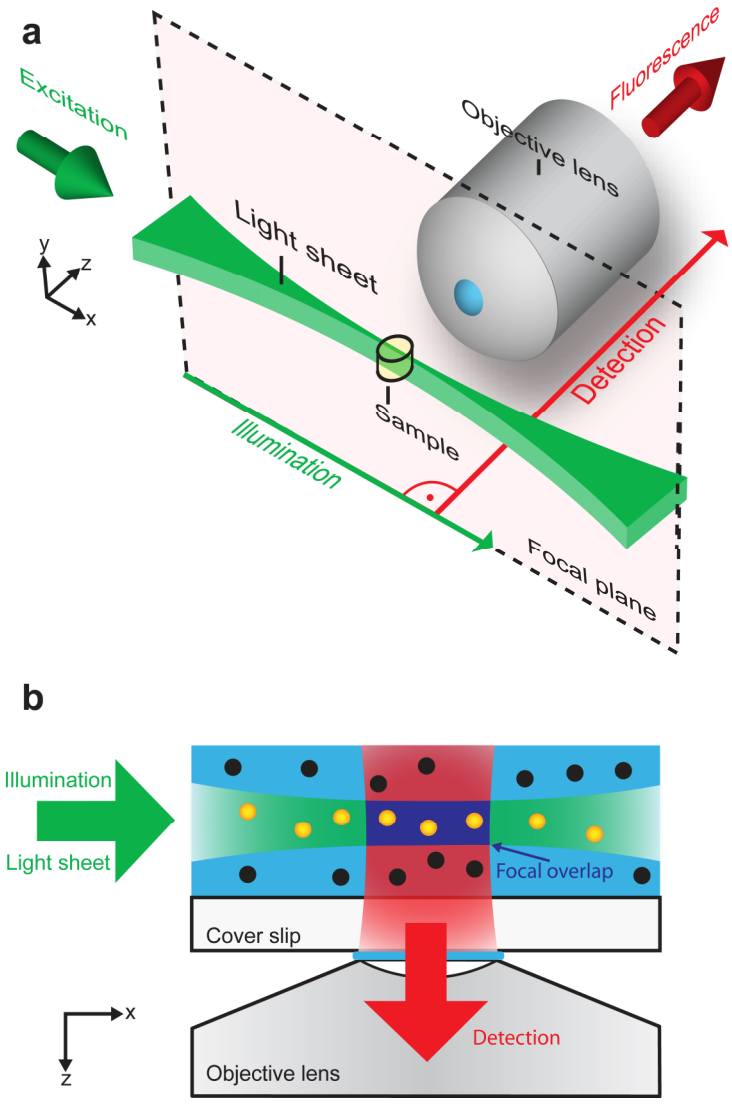

Figure 1.2 Principle of light sheet microscopy. (**a**) In light sheet microscopy, the fluorescence excitation and the detection are split into two separate light paths. The illumination axis is perpendicular to the detection axis. An objective lens is used to collect fluorescence from the complete field-of-view and maps it on a CCD (not shown). (**b**) Configuration of illumination and detection for an inverted microscope. The light sheet illuminates only a thin volume and is aligned to be centered at the focal plane of the detection objective. Only fluorescence signals from the focal overlap region (blue) are detected. No out-of-focus fluorescence contributes to the image and an optical sectioning effect is created. (a) modified from [26].

Light sheet illumination has several advantages over standard epi-illumination and over other optical sectioning schemes [9]. Due to the optical sectioning effect no out-of-focus fluorescence is detected, what significantly enhances the signal-to-noise-ratio. Unlike in confocal microscopy, where an image is usually acquired by point-scanning an image pixel by pixel, LSFM combines the optical sectioning effect with parallel imaging of the complete focal plane (**Figure 1.3**). This makes data acquisition extremely fast and efficient in comparison to confocal or other scanning microscopes. In speed-demanding

applications, for example single molecule tracking, frame rates of up to 500 Hz with a sufficiently large field-of-view can be achieved in combination with fast and sensitive cameras such as electron multiplication CCD (EMCCD) cameras. Raster scanning microscopes, for example confocal or two-photon microscopes hardly achieve such speeds. Although the speed at which the scanning itself can be carried out may be the limiting factor, it is usually not sufficient to increase scanning speed to obtain satisfactory images at high frame rates. Faster scanning reduces the dwell time of the laser beam on any one pixel and, as a consequence, the signal level [27]. In order to keep the photon count per pixel constant when increasing the frame rate, the illumination power must be increased as well. Thereby, fluorophore excitation and the number of emitted photons would remain constant. However, high illumination intensity increases the risk of fluorophore saturation, photo-bleaching and photo-toxicity. Multi point or line scanning techniques allow higher acquisition speeds with lower excitation intensities through parallel illumination and acquisition of multiple points. However, these techniques are still not competitive with parallel data acquisition. Moreover, when fast, dynamic processes are observed, the inherent time delay between adjacent raster introduces artifacts into the image while scanning.

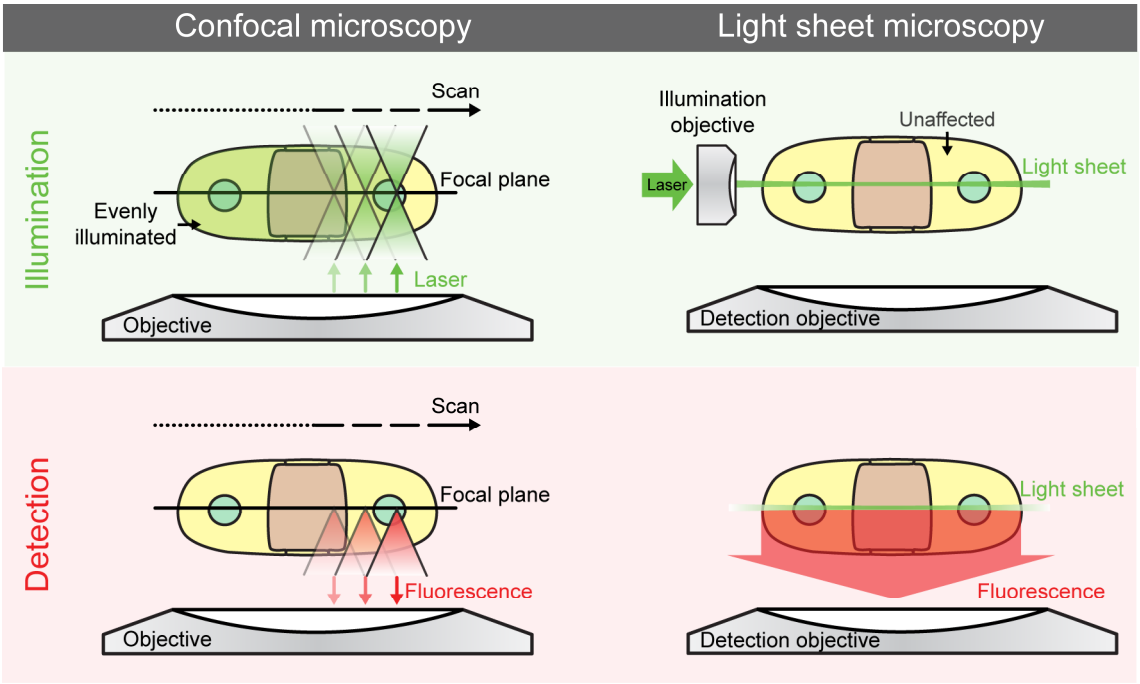

Figure 1.3 Image generation in confocal microscopy compared to light sheet microscopy. Light sheet microscopy features faster image acquisition and less photo-toxic effects than confocal microscopy. To acquire an image in confocal microscopy a tightly focused laser beam is scanned across the sample, thereby exposing the sample to light not only in the plane of interest but also above and below. In light sheet microscopy the sample is selectively illuminated only in the plane of interest. The raster scanning process in confocal microscopy limits the achievable time resolution and is slow compared to light sheet microscopy, where the complete field-of-view is imaged at once.

All these problems are avoided by the wide-field detection of LSFM and it is therefore ideally suited for high-speed applications.

Since in LSFM no parts of the specimen outside the light-sheet are illuminated, they are not subject to effects of light exposure. Photo-toxic effects are reduced compared to raster scanning illumination techniques like confocal microscopy [27], where the whole sample is exposed to the excitation light (**Figure 1.3**). Out-of-focus parts of the sample are photo-bleached or damaged even when an image of only a single plane is acquired. These negative effects scale with the number of images. For example the last image plane in a three dimensional stack of 100 images has already been exposed 99 times to excitation light. The minimization of photon exposure in LSFM is especially prominent when three dimensional image stacks are acquired, here the last image is as faultless as the first. This automatically allows longer observation times of sensitive specimens.

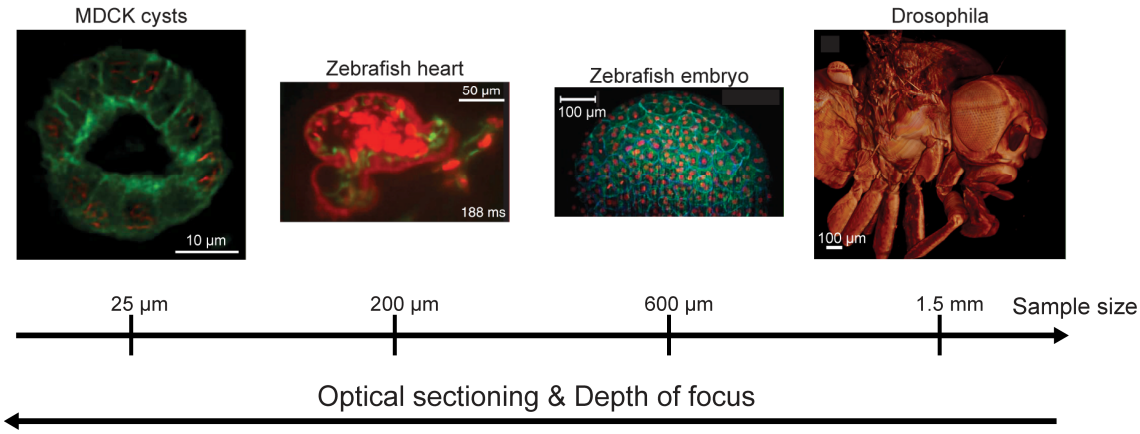

Figure 1.4 Correlation between sample size and required optical sectioning thickness and depth of focus. Different samples sizes require different light sheet dimensions for an imaging in toto. With increasing sample size, the depth of focus has to increase to achieve a large field-of-view. This automatically results in a larger optical sectioning thickness. Smaller samples require a small field-of-view and hence the optical sectioning thickness is reduced. Images left to right from [26,28,29,30].

Although the lateral resolution is the same with light sheet illumination as in epi-illumination, the situation is different for the axial resolution. In LSFM only a thin axial section of the focal plane is selectively illuminated. In many cases the thickness of the light sheet defines the axial resolution of the system (see Chapter 2.4.1). If the light sheet thickness is smaller than the axial extent of the detection point-spread-function (PSF), the illumination sheet will define the focal volume seen by the camera and not the detection objective lens. In this case, the effective axial resolution of the microscope is increased. Usually the light sheet thickness is between 1 and 10 µm (z-axis), depending on the field-of-view, and is created by focusing a Gaussian beam. The

focused light sheet extension is inverse proportional to the incoming Gaussian beam radius [25].

$$w_{0,yz} = \frac{2\lambda_0 f}{\pi\ n\ r_{yz}} \tag{1.5}$$

$w_{0,yz}$ is the focused 1/e²-beam radius along the *y*- or *z*- axis, λ_0 the used wavelength, *f* the focal length and r_{yz} the incident beam radius along the *y*- or *z*- axis. (for definition of the axes see **Figure 1.2**). The usable field-of-view can be defined as depth-of-focus *b* along the x-axis times the height of the light sheet (y-axis). Here, *b* is given according to:

$$b = 2z_0 = \frac{\pi\ n\ w_0^2}{\lambda_0} \tag{1.6}$$

z_0 is defined as the Rayleigh length of the focused Gaussian Beam, where the beam radius is $\sqrt{2}\ w_0$. It is obvious that the light sheet thickness (z-axis) and the field-of-view along the illumination axis are related to each other. Therefore both parameters have to be chosen carefully for the specimen of interest and a thin light sheet is not always favorable. For example, many applications, e.g. in developmental biology, require large field-of-views and long working distance objectives to image specimens millimeters in size (**Figure 1.4**).

Low numerical aperture (NA) objectives required to detect the complete field-of-view have a sufficiently large lateral resolution but suffer from a poor axial resolution (e.g. 80 µm for a NA of 0.1 in air). In such a case the volume illuminated by the light sheet is significantly thinner than the depth-of-focus of the detection lens and the axial resolution is considerably increased. For low numerical aperture detection lenses (NA < 0.8) the axial resolution in LSFM is usually increased in comparison to epi-fluorescence, two-photon and confocal microscopy [31]. However, even though the axial resolution in LSFM is unchanged for objectives with a higher NA, the optical contrast is strikingly enhanced (Chapter 2 & 3). The lateral resolution is the same as in a conventional epi-illumination microscope and is solely defined by the detection objective and emission wavelength used. Although the lateral resolution is not increased, in practice fine structures may be better discerned that would remain hidden in the out-of-focus haze of epi-illumination microscopy, due to the contrast enhancement of the optical sectioning effect.

Light sheet microscopy is especially well suited to observe biological specimens under biocompatible conditions and in three dimensions. LSFM allows three dimensional mounting of living specimens in an aqueous medium without the interference of hard solid surfaces, therefore mimicking more closely their natural environment. Usually for

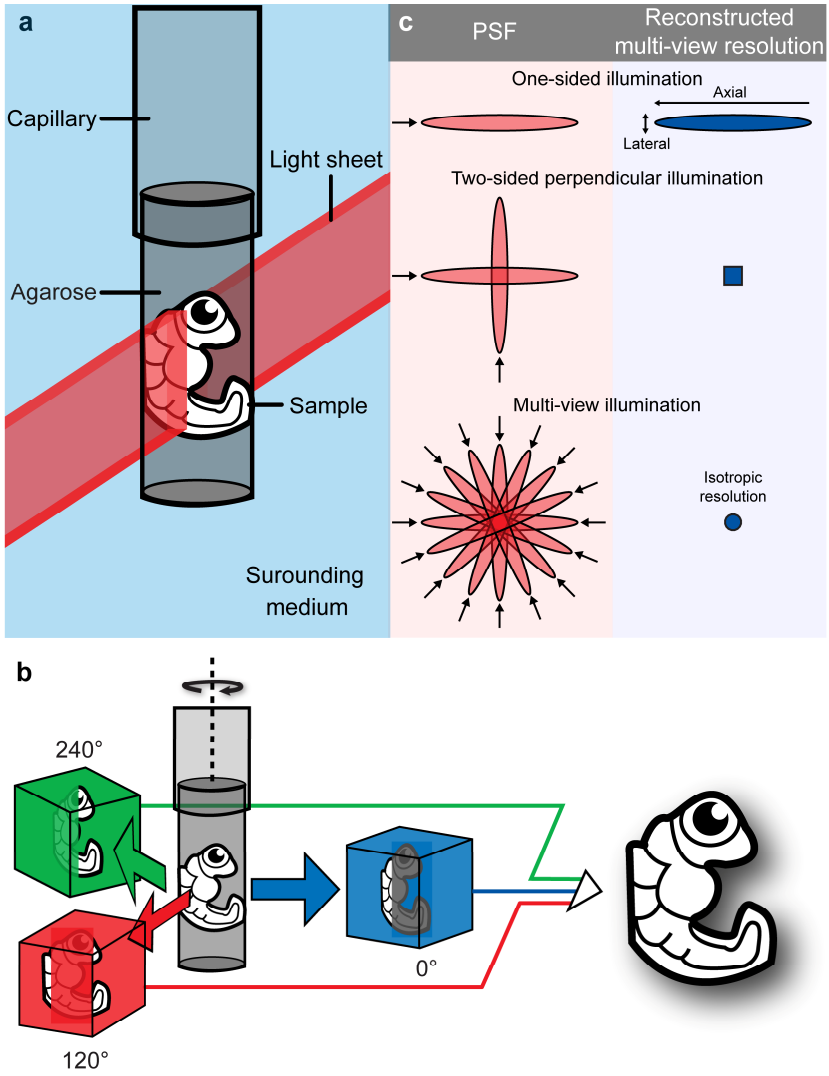

Figure 1.5 Multi-view reconstruction with light sheet microscopy. (**a**) Schematic representation of a biocompatible sample preparation in light sheet microscopy. Living zebrafish embryos are embedded in an agarose gel cylinder held by a glass capillary mounted from top. The embryo can develop in a three dimensional environment. (**b**) By rotating the sample, image stacks can be recorded from different angles. Thus, light scattering and absorption can be compensated by a subsequent computational multi-view reconstruction (MVR) of the sample. (**c**) In overlapping regions, MVR can be used to improve the resolution in the final image. For one-sided illumination the point spread function is typically elongated in axial direction, resulting in a poorer axial resolution. For two orthogonal images, the good lateral resolution in one image compensates for the poor axial resolution in the other image. Combining several images from different points-of-view leads to an isotropic resolution in the overlapping region. (a) and (b) modified from [32,33].

three dimensional mounting the specimen is embedded in a transparent gel, such as agarose, and held in place from above (**Figure 1.5a**). Such mounting allows an unrestricted view from all sides and often it is possible to rotate the sample. This is essential for multi-view reconstruction (MVR) imaging, an elegant imaging strategy in light sheet microscopy. Multiple three dimensional image stacks from different

directions are recorded and subsequently computationally fused to a single data set (**Figure 1.5b**). There are two major benefits of MVR [26]. First, in strongly scattering and absorbing tissue, the image quality can be improved by fusing images recorded from different angles. Second, in transparent samples and in regions where the data sets overlap, the resolution of the final image is improved and becomes isotropic (**Figure 1.5c**). For two image stacks recorded under different angles but with an overlapping area, the poor axial resolution of one dataset is compensated by the good lateral resolution of the other data set. Of course MVR is not limited to LSFM, but due to the beneficial optical properties of light sheet microscopy it performs especially well in combination with it. The optical advantages combined with the unique biocompatible mounting enables the recording of large biological specimens over long periods of time. For instance the evolution and growth of early zebrafish embryos under physiological conditions has been be visualized for several days [29].

1.5 Adaptations of light sheet microscopy

The principle of light sheet microscopy was already used in the so-called "ultramicroscope" for the investigation of colloidal particles at the beginning of the 20th century [34]. The adaptation of the technique to fluorescence microscopy is comparatively new, but it has intensely been developed from its introduction until now and is already used for numerous applications. There is no singular light sheet microscope design which is adapted in all the different laboratories. Usually the microscope is build around a certain application and therefore the designs differ significantly in three major points: (1) Light sheet generating technique. (2) The achievable field-of-view and optical sectioning thickness. Both are inversely proportional to each other and have to be finely balanced for optimal imaging conditions. (3) Sample preparations and mounting methods, which are very different between various experimental setups. Hence, often enough light sheet microscopes are specialized and only able to investigate samples of a certain size or even just a single organism.

Selective plane illumination microscopy (SPIM) is an implementation of LSFM that has found many applications. Using this technique, live fluorescently labeled medaka and drosophila embryos were imaged and reconstructed from multiple views [35]. High-speed applications such as time recordings of a beating zebrafish heart [36] as well as SPIM-fluorescence correlation microscopy (SPIM-FCS)[37] deep inside the specimen were realized with this design.

A cylindrical lens or a combination of cylindrical beam expander and objective lens generates the light sheet inside a buffer filled chamber. A water-dipping lens is focused onto the light sheet and detects fluorescence in the focal overlap region (**Figure 1.6**). The optical setup is usually built horizontally to the optical table and the sample is

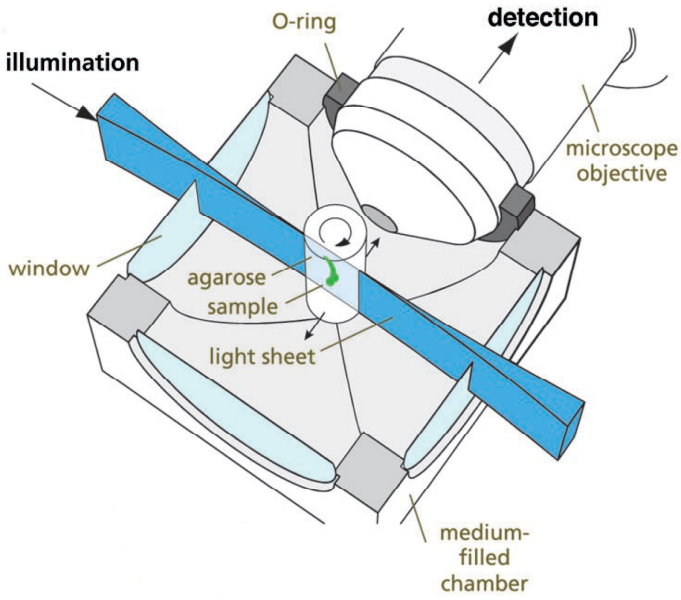

Figure 1.6 Selective plane illumination microscopy (SPIM). Schematic shows the SPIM illumination inside the sample chamber. The sample is embedded in a cylinder of agarose gel. The solidified agarose is extruded from a syringe (not shown) that is held in a mechanical translation and rotation stage. The agarose cylinder is immersed in an aqueous medium that fills the chamber. The excitation light enters the chamber through a thin glass window from the side. The microscope objective lens, which collects the fluorescence light, dips into the medium with its optical axis orthogonal to the plane of illumination. The objective lens can be moved axially to bring the illumination plane into focus. Sketch from [35].

immersed in the buffer solution from above. This geometry gives the user the possibility to rotate the sample parallel to the gravitational axis without any deformations of the sample. Multiple images can be recorded under different angles for multi-view reconstructions. Optionally the sample can also be illuminated from the opposing side to compensate for image degradation along the illumination axis in strongly scattering tissue. Multidirectional SPIM (mSPIM) is a variation of this principle to reduce the shadowing by pivoting the light sheet in the detection focal plane during each single image acquisition [38]. Due to this high-speed pivoting of the light sheet, an evenly illuminated field-of-view can be achieved. In SPIM, a stack of images is recorded by moving the sample through the light sheet stepwise.

The sample is usually embedded in a soft gel such as agarose. The refractive index of the embedding medium has to be carefully matched to the buffer medium. Otherwise refraction of the illumination beam occurs at the buffer-gel interface distorting the light sheet. For *in vivo* measurements the stiffness of the embedding gel has to be controlled as well. Especially for studying the development of organisms over long periods of time a too stiff gel might lead to abnormal evolution of the organism. Temperature, oxygen concentration, pH-value and other important parameters can be easily controlled in the buffer chamber. Because it features a large field-of-view, high spatiotemporal resolution

and high biocompatibility, SPIM is particularly well suited for three dimensional *in vivo* studies of large multi-cellular organisms over long periods of time. Although single cell studies have been performed with SPIM [39,40] it is difficult to perform single cell or single molecule studies with it, due to the laboriously sample mounting and the limited numerical aperture of the detection lens. Usually a higher lateral resolution and photon collection efficiency is required for these experiments.

Digital scanned light sheet microscopy (DSLM) is similar to SPIM in terms of microscope design, field-of-view and sample mounting, but differs significantly in the light sheet generation method. In DSLM a laser beam is focused and rapidly scanned up and down during exposure time, generating a virtual light sheet (**Figure 1.7**) [41]. The advantages of this technique are the uniform illumination intensity over the complete field-of-view and the easy light sheet height adjustment through computer controlled scan mirrors. Due to the sequential illumination in DSLM the beam illuminates only a fraction of the final image at once. Therefore the achievable acquisition time for a single image is limited by the image height and speed of the scanning mirrors and is larger than in SPIM. Furthermore, the local light intensity has to be about 300 times higher than in SPIM in order to achieve the same fluorescent yield across the final image in the same amount of time [26], which results in increased photo-bleaching.

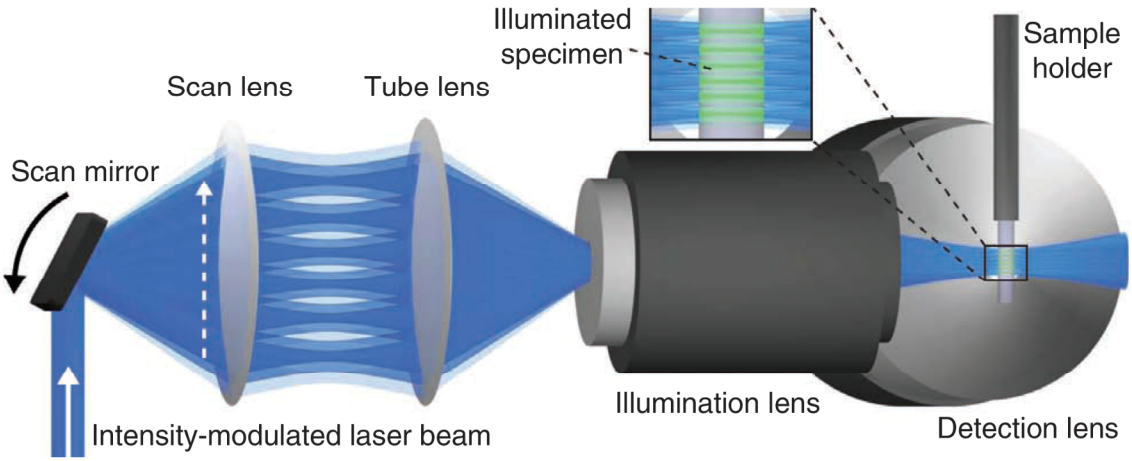

Figure 1.7 Digital scanned light sheet microscopy DSLM. The laser beam illuminates the specimen from the side and excites fluorophores along a single line. Rapid scanning of a thin volume and fluorescence detection at a right angle to the illumination axis provides an optically sectioned image. The scan lens converts the tilting movement of the scan mirror into a vertical displacement of the laser beam. The tube lens and the illumination objective focus the laser beam into the specimen, which is positioned in front of the detection lens. Optionally the intensity of the laser beam can be synchronized with the scanning process, thus creating a structured illumination profile in the focal plane of the detection lens. Sketch from [29]

A additional benefit of DSLM is the optional implementation of structured illumination (DSLM-SI) [29]. In DSLM-SI, the intensity of the illuminating laser beam is electronically modulated with an acousto-optical-tuneable-filter (AOTF) synchronized with the scanning process. With an appropriate AOTF setting this results in a high-quality sinusoidal intensity profile. Incoherent structured illumination provides the optical means for separating information (non-scattered signal photons) from background (scattered signal photons) in the recorded images, thus improving the contrast in the final image. To achieve this every plane has to be excited three times with a phase shifted illumination pattern and a new image I is calculated from each set ($I_{0°}$, $I_{120°}$ and $I_{240°}$, the index indicates the phase shift of the illumination grating) [42].

$$I = \sqrt{\frac{1}{2}\left((I_{0°} - I_{120°})^2 + (I_{120°} - I_{240°})^2 + (I_{240°} - I_{0°})^2\right)} \tag{1.7}$$

In this way the sample suffers under an increase in the number of excitation photons. Hence photo-bleaching and photo-toxic effects are increased as well. Of course, the time resolution is also decreased by a factor of three.

DSLM and DSLM-SI provide a large, easily adjustable width of the light sheet and a high biocompatibility and thus they cover the same range of applications like SPIM. In comparison to SPIM the image quality is improved due to the more homogeneous illumination profile and the stripe reduction effect in the scanning process (similar to mSPIM), especially when structured illumination is used. However, the scanning process limits the achievable time resolution. Since a single line is scanned at once DSLM is still faster than conventional confocal microscopy, but disqualifies for high-speed measurements, such as single molecule tracking. In general the photon exposure is higher in DSLM than in SPIM, in particular when structured illumination is used. This should be taken into account when photo sensitive samples are studied.

A different approach to light sheet microscopy is the so called "ultramicroscopy", which combines the optical sectioning of LSFM with an additional histological procedure that clears biological samples to complete transparency [43]. This histological technique allows three dimensional optical imaging of weak and fast photo-bleaching fluorescence signals deep inside the tissue. To obtain transparent biological samples the water of the organism has to be replaced with a liquid of the same refractive index as the clearing solution. The main goal of ultramicroscopy is the complete three dimensional reconstruction of large fixed biological specimen, such as mouse embryos or fruit flies and other fixed tissues a few millimeters in size.

The experimental setup differs from SPIM or DSLM setups (**Figure 1.8**). Since large samples are observed, the excitation light is increasingly attenuated as it penetrates the

sample. To compensate for this attenuation, a two-sided illumination is implemented. Two light sheets are generated and illuminate the sample from opposing directions. The sample has to be permanently kept in clearing solution rather than water and is enclosed in a glass chamber. The sample is mounted in an upright microscope on a motorized block, so that fluorescence is detected from above. The two light sheets illuminate the sample perpendicular from the side and are generated by cylindrical lenses and rectangular apertures. The use of lenses with unmatched refractive indices leads to spherical aberrations and astigmatism and consequently results in a less optimal optical sectioning. Furthermore, the rectangular apertures cause refractive effects which result in an uneven illumination profile. The clearing solution has a refractive index higher than water and is very aggressive. For this reason, no dipping objectives can be used. Due to the larger field-of-view the optical sectioning thickness is typically about 10 µm and only low magnification detection lenses can be utilized. They have a reduced lateral and axial resolution and lack a high photon collection efficiency and hence are unsuited for high resolution or sensitive signal-to-noise ratio applications.

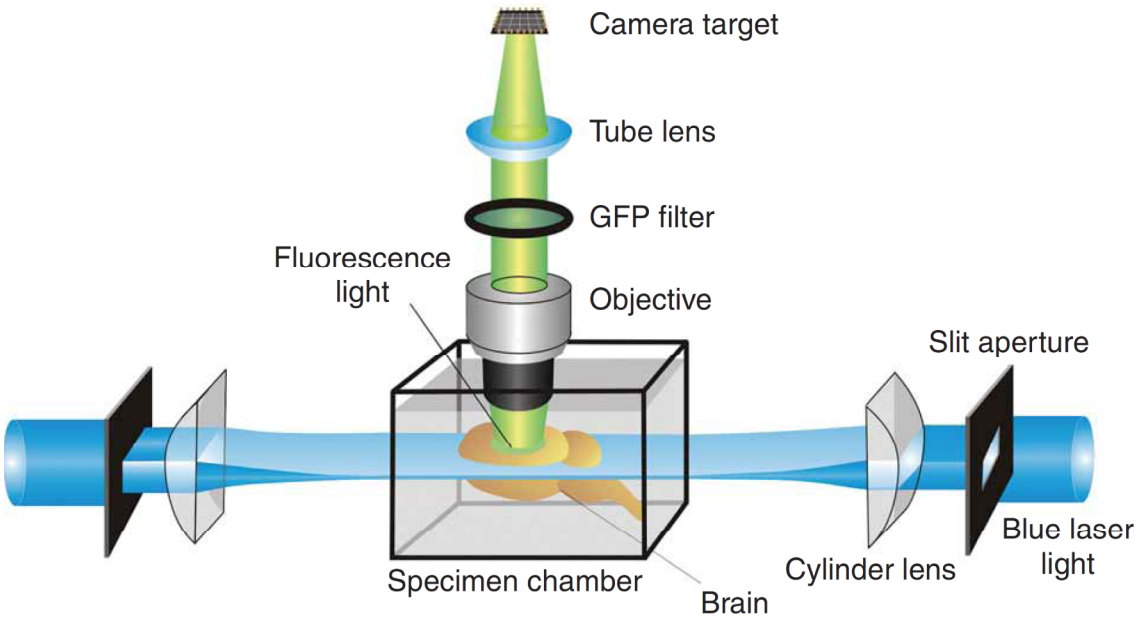

Figure 1.8 Ultramicroscopy. The sample is illuminated simultaneously from two sides by a thin sheet of light. The light sheet is created by slit apertures and cylindrical lenses. Fluorescent light is collected by the objective lens from above. The fixed specimen is placed in clearing solution inside a glass chamber. Stray light is blocked by a filter and the image is projected through the tube lens onto the camera target. Sketch from [43].

Objective-coupled planar illumination (OCPI) was realized to quickly acquire three dimensional image stacks of electrically active neurons in brain tissue [44]. The illumination optics are rigidly coupled to the detection objective, so that both can be translated synchronously. This minimizes motion induced vibrations, because the sample is left at rest. The light sheet is generated by collimating the output of a single-

mode optical fiber and then passing it through a cylindrical lens, creating a gradual waist whose line focus is positioned in the centre of the focal plane of the objective (**Figure 1.9**). Imaging i*n vivo* brain tissue suffers heavily from light scattering and absorption. To insure that neither the illumination beam nor emitted light propagates through long distances in tissue, the whole microscope is tilted so that both illumination and detection axes are 45° relative to a horizontally mounted sample (**Figure 1.9b**). By this means, the superficial layers of the sample are accessible to both illumination and imaging.

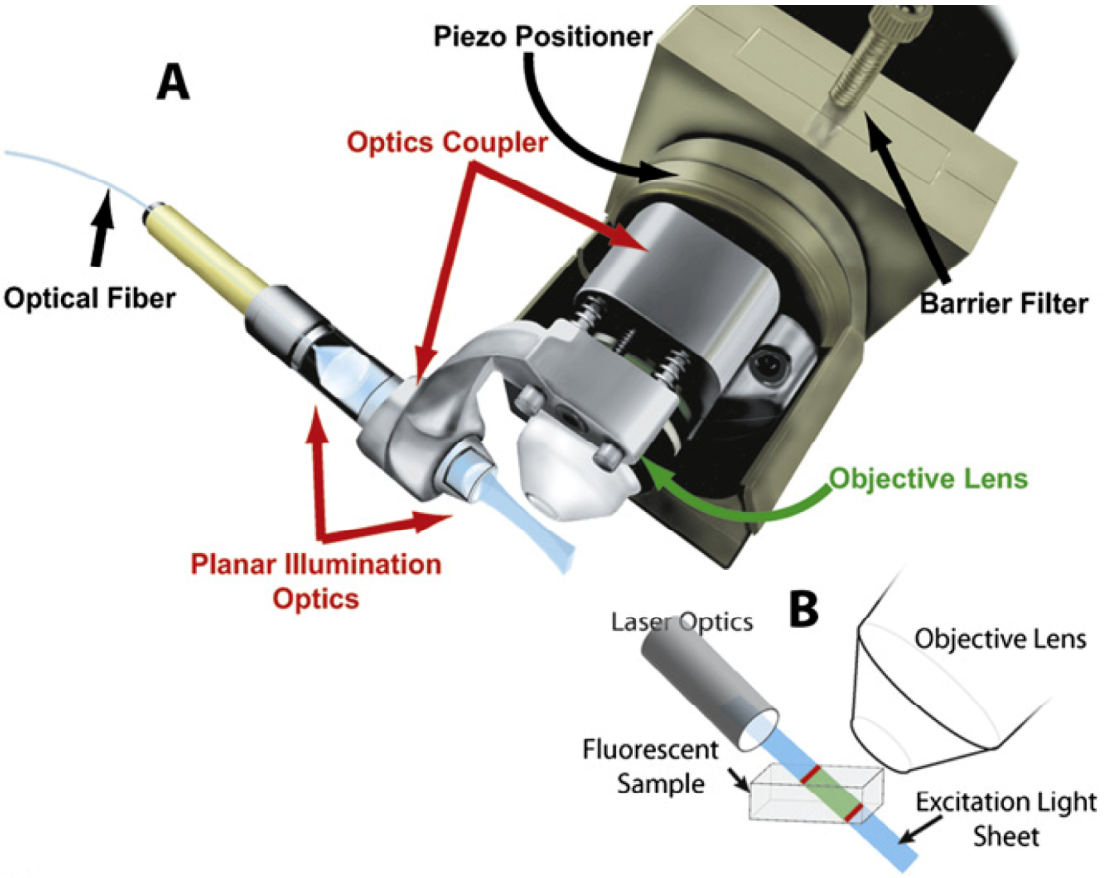

Figure 1.9 Objective coupled planar illumination (OCPI). (**A**) Excitation light from a laser arrives via optical fiber and is shaped by two lenses to form a thin sheet of light (3–5 µm thick in the field-of-view). Sectioning is accomplished by aligning the light sheet with the detection objective focal plane, preventing fluorescence excitation in out-of-focus regions. The illumination optics is coupled to the objective lens, maintaining alignment with the focal plane during z-axis scanning with a piezoelectric device. Objective lens and illumination optics are designed for water immersion. A rotating mount adaptor allows to change the orientation of the complete microscope (usually 45°) and adapting it to the needs of the preparation. (**B**) Schematic showing the orientation of tissue, objective, and illumination optics. Sketch from [44].

With this configuration thousands of active neurons in a three dimensional volume can be imaged simultaneously in only two seconds. At the same time the low photo-bleaching rate enables studies of neuronal networks over hours. A large field-of-view is required to visualize hundreds of neurons in a single plane, whereas previous studies had been limited to imaging of only ten neurons at the same time [44]. OCPI is at least a hundred-fold faster than two-photon or confocal microscopes with comparable field-of-views and in addition OCPI has an approximately hundred times smaller photo-bleaching rate. However, this experimental realization is rather inflexible. Neither the light sheet geometry nor the detection objective lens can be altered. Both are designed and matched for a certain purpose and difficult to exchange. Through this miniaturized illumination optics the achievable optical sectioning thickness is limited. The technique is not applicable for high resolution measurements like SPIM. Similar to the ultramicroscope, the detection objective has to visualize a large field-of-view and therefore only objectives with a low magnification and low NA are utilized. This results in a reduced lateral resolution and low photon collection efficiency.

1.6 Applications of light sheet microscopy

Light sheet based fluorescence microscopy (LSFM) already had a remarkable success in its various realizations in imaging complex three dimensional multi-cellular organisms *in vitro* and *in vivo*.

Selective plane illumination microscopy (SPIM) is especially well suited to study biologically complex transparent samples *in toto*. One of the first major studies conducted with SPIM utilized the optical sectioning and low photo-bleaching rates combined with *in vivo* imaging to visualize all muscles in a transgenic medaka embryo (**Figure 1.10a**) [35]. In further applications the high sensitivity and speed of SPIM was used for high-speed heart imaging inside medaka and zebrafish. Previously heart development had been analyzed using fixed sections. Obviously the dynamic development and function of the heart can only be analyzed in living tissue. Time recordings of beating zebrafish hearts with frame rates of up to 200 Hz enabled the three dimensional resolved *in vivo* optical mapping of the cardiac development (**Figure 1.10b**) [36]. In another example SPIM played a key role in identifying a third mode of blood vessel formation in zebrafish vascular development and characterization of the involved receptors [45].

Another remarkable success of light sheet microscopy was the quantitative analysis of over thousand cells tracked simultaneously mapping the entire early zebrafish embryogenesis over periods longer than 24 hours (**Figure 1.10c**) [41]. Here the benefits in field-of-view and image quality of the digital scanned light sheet microscopy (DSLM) were used. The quantitative reconstruction of early cell division patterns

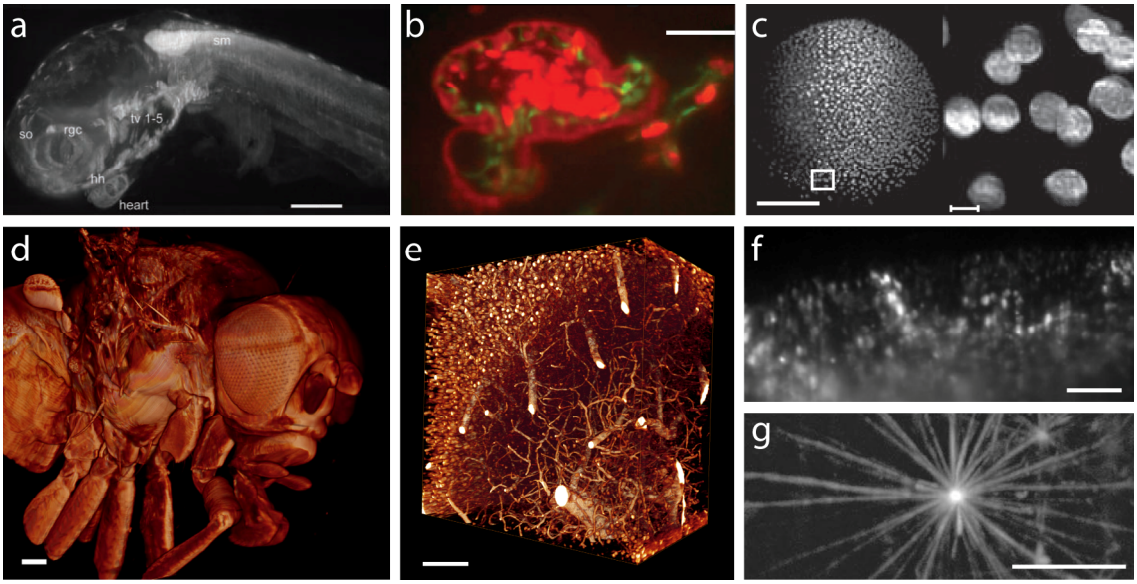

Figure 1.10 LSFM images. (**a**) Medaka embryo imaged with SPIM and processed by multi-view reconstruction. Maximum intensity projections of the fused data set. The high resolution throughout the entire fish allows identification of different tissues: rgc, retinal ganglion cells; so, superior oblique; hh, hyohyal; sm, somitic mesoderm; tv, transverse ventrals. Scale bar 200 µm. (**b**) High-speed recordings with SPIM of transgenic zebrafish heart beats expressing fluorescent proteins in the endocardium, myocardium and blood. Scale bar 50 µm. (**c**) DSLM imaging and reconstruction of zebrafish embryogenesis. Digital embryo reconstruction of a nuclear labeled wild-type zebrafish embryo at an early developmental stage. Scale bar 100 µm. Close-up on (c) demonstrating sub-cellular resolution of the developing embryo. Scale bar 10 µm. (**d**) Ultramicroscopy image after reconstruction of the surface of an entire Drosophila fly. Scale bar 100 µm. (**e**) Three dimensional display of the mouse hippocampus imaged with ultramicroscopy. The section is about 500 µm under the surface of the excised hippocampus. Scale bar, 100 microns (**f**) A single image of fluorescently labeled mouse vomeronasal sensory epithelium visualizing single neurons with OCPI. Scale bar, 100 microns (**g**) Maximum intensity projection showing a microtubule organizing center in an interphasic Xenopus laevis egg extract. Imaging was performed with SPIM. Scale bar 10 µm. Images (a) – (g) from [26,30,35,40,41,44,46].

revealed an initial symmetry break. A quantitative analysis provided a comprehensive model of early formations in zebrafish embryos.

Fixed tissue can be imaged at high resolution in histological sections. Three dimensional reconstructions from many such sections are laborious and require reliable registration algorithms. Alternatively, the sample can be fixed and optically cleared and imaged with ultramicroscopy *in toto*. Full three dimensional reconstructions of complete mouse brains and embryos were possible by a previous fixation and clearing of the comparatively large samples several millimeters in size [30,43,46]. Three dimensional high resolution images of dendritic trees and spines of populations of neurons in isolated hippocampi **(Figure 1.10e**) were obtained and details of the anatomy of fruit flies (**Figure 1.10d**) as well as mouse embryos visualized.

Unraveling the functions of the diverse neural types in a local network ultimately requires methods to record most or all of its cells simultaneously. Objective-coupled planar illumination (OCPI) was used to image thousands of mouse neurons in a stack of fifty planes with a large field-of-view of 700 µm x 100 µm and acquired in just two seconds with bleaching rates that were approximately a hundred times smaller than in confocal microscopy (**Figure 1.10f**) [44]. Fast responses in pheromone sensing neurons in the mouse were studied with frame rates of 200 Hz, at least 100-fold faster than previously achieved with single- or multi photon microscopy.

Light sheet microscopy is not only limited to large biological specimens. Performing single cell studies with SPIM on *Xenopus laevis* egg extracts revealed the dynamics and mechanics of microtubule growth (**Figure 1.10g**) [39,40]. Here the study profited from the three dimensional sample mounting in light sheet microscopy to measure microtubule dynamic instability and elasticity. A significant divergence between microtubule dynamics in two and three dimensions was demonstrated. A new kinetic model was proposed based on these physiologically more relevant experiments that allow microtubules to undergo an unconstraint growth in contrast to traditional studies, which had been performed on two dimensional surfaces.

A further advancement of the technique is the combination of SPIM with camera based fluorescence correlation spectroscopy (SPIM-FCS) to investigate particle numbers and diffusion coefficients. Multiple small observation volumes in a three dimensional environment were observed to record 4096 FCS spectra within seconds inside a zebrafish embryo at ultra low laser power [37]. This new FCS modality provides more measurements per time and more, less photo-toxic measurements per sample than confocal based methods, where typically one spectrum is recorded in the same acquisition time.

1.7 Thematic linkages

As exemplified above LSFM is a very flexible technique and can easily be adapted to a lot of applications in life sciences. However, the instrument of choice should carefully be considered, because the experimental realization has a great impact on key parameters like field-of-view, resolution and acquisition speed. For the case of single molecule tracking in living biological extended samples SPIM seems to be the most eligible candidate. SPIM provides the necessary temporal resolution to follow single molecules over longer periods of time unlike DSLM, where the acquisition time is limited by the scan process. In terms of spatial resolution it performs better than OCPI or ultramicroscopy, where only low NA lenses can be used. In comparison to ultramicroscopy it allows the observation of living samples.

The SPIM principle was the starting point for the work in this thesis, to construct a versatile light sheet microscope for imaging of live biological specimens and single molecule tracking deep inside living organisms. In chapter 2 the theory of light sheet illumination with an elliptical Gaussian beam is described and experimentally verified. The improved image contrast in thick specimens by imaging with light sheet microscopy compared to epi-illumination is demonstrated and experiments show the capability of light sheet microscopy to track and analyze single particles in aqueous solution. In chapter 3 a novel experimental realization of a light sheet microscope is shown and characterized. The power of the experimental setup is demonstrated by visualizing small, fast moving single molecules in aqueous solution, which were not accessible to single molecule tracking before. Furthermore the instrument was utilized to track single dextrane molecules and mRNA particles in the nucleus of living salivary gland cells of the *C.tentans* larvae, up to 200 µm deep within the specimen. In chapter 4 an improvement of the experimental setup is described, which allows the continuous adjustment of the light sheet dimensions by implementing a cylindrical zoom lens system in the illumination pathway. The performance of the zoom system is experimentally verified and its benefits in live biological specimen imaging demonstrated.

2 High-contrast single-particle tracking by selective focal plane illumination microscopy

Jörg G. Ritter, Roman Veith, Jan-Peter Siebrasse and Ulrich Kubitscheck. Opt Express 16: 7142-7152 [47]

2.1 Abstract

Wide-field single molecule microscopy is a versatile tool for analyzing dynamics and molecular interactions in biological systems. In extended three-dimensional systems, however, the method suffers from intrinsic out-of-focus fluorescence. We constructed a high-resolution selective plane illumination microscope (SPIM) to efficiently solve this problem. The instrument is an optical sectioning microscope featuring the high speed and high sensitivity of a video microscope. We present theoretical calculations and quantitative measurements of the illumination light sheet thickness yielding 1.7 µm (FWHM) at 543 nm, 2.0 µm at 633 nm, and a FWHM of the axial point spread function of 1.13 µm. A direct comparison of selective plane and epi-illumination of model samples with intrinsic background fluorescence illustrated the clear advantage of SPIM for such samples. Single fluorescent quantum dots in aqueous solution are readily visualized and tracked proving the suitability of our setup for the study of fast and dynamic processes in spatially extended biological specimens.

2.2 Introduction

Single molecule microscopy and single particle tracking are versatile tools for analyzing dynamic interactions in biophysical and biological systems in three dimensions (3D) without averaging over molecular ensembles [48]. Reduction of background fluorescence is of key importance to achieve a sufficiently high signal-to-noise ratio (SNR) of the intrinsically weak single-molecule signals. The use of high numerical aperture lenses and low fluorescent particle concentrations is mandatory, because otherwise the fluorescence of out-of-focus particles complicates the detection of single particles in the focal plane.

A further reduction of out-of-focus fluorescence can be achieved by using an illumination of the object plane perpendicular to the optical axis of the detection objective lens instead of the commonly used epi-illumination (**Figure 2.1**). This principle of an orthogonal illumination was already used in the so-called ultramicroscope for the investigation of colloidal particles at the beginning of the 20th century [34]. Meanwhile, the principle of a selective illumination of the focal plane was very successfully adopted to fluorescence microscopy in various ways (abbreviated here as SPIM for selective plane illumination microscopy) [35,38,43,49,50]. The

fundamental principle of SPIM is the exclusive illumination of a thin spatial region around the focal plane of the detection objective lens. Its combination with fluorescence produces an intrinsic optical sectioning effect, because fluorescent molecules are only excited and visualized within the illuminated focal plane. Unlike in a conventional epi-fluorescence microscope, no out-of-focus fluorescence is contributing to the image. In light-sheet based microscopy the sample is illuminated with a laser beam, which is shaped by a cylindrical lens telescope into a strongly elliptical beam profile. An illumination objective lens focuses this profile into the sample thereby creating the light sheet. The sample is usually moved by a scanner through this plane, which is imaged by a CCD camera. This elegant optical sectioning microscope combines the improved contrast and resolution of a confocal laser scanning microscope with the speed and sensitivity of a video microscope. Also, photo-bleaching is reduced, because only the imaged sample region is illuminated. Finally, due to the fact that the image is acquired in a parallel manner the imaging rate can be greatly increased compared to optical sectioning microscopes based on point or line scanning. All these features make SPIM the ideal imaging technique for the visualization and tracking of single molecules, particles or vesicles in biological or other microsystems.

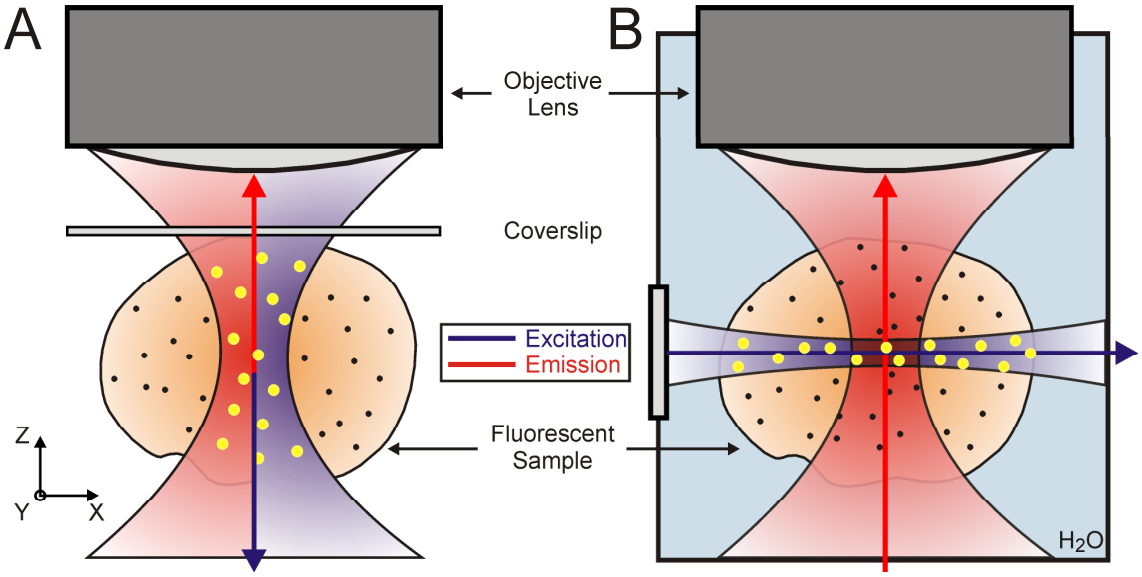

Figure 2.1 Comparison of epi-illumination and SPIM. In contrast to (**A**) epi-illumination microscopy the emission path in (**B**) SPIM is perpendicular to the excitation beam path. By selective illumination of the focal plane, no out-of-focus fluorescence is generated. This results not only in a strongly reduced background signal and higher resolution, but also in the optical sectioning capability of the instrument.

In this work we present the construction of a SPIM with a very thin light sheet and high axial resolution. The imaging properties of this microscope were calculated both by theory and ray tracing, and matched perfectly the experimental results. We

characterized the improved contrast of our SPIM and its capability of tracking fast fluorescent particles by measuring the diffusion coefficient of single quantum dots in aqueous solution.

2.3 Microscopic setup

Figure 2.2 shows a sketch of our microscopic setup. The fluorescent object is positioned within a water-filled chamber, and illuminated by a laser beam along the x axis, while the fluorescence emission imaged along the z axis. By translating the sample along the z axis, imaging of different optical slices in the xy-plane is possible.

The laser beam is expanded and shaped by a cylindrical Galilean beam expander. Out of the incoming circular-symmetrical Gaussian beam with a wavelength of 633 nm we produce a beam with an elliptical intensity profile with a $1/e^2$ diameter of 7.2 mm along the z-axis and of 1.6 mm along the y-axis. For green laser light (λ_0 = 543nm) we obtain 6.6 mm for the z-direction and 2.2 mm for the y-direction, respectively. The strongly elliptical Gaussian beam is then focused by a custom-designed long distance objective lens with high numerical aperture (NA 0.33) into a water chamber [51]. In this manner we achieved a sufficiently high irradiance of 1 to 10 kW/cm^2 even when using a low power laser (2 mW) for fluorescence excitation, and also limited the illumination region in order to avoid unnecessary photo-bleaching in the sample. The custom-made lens was designed to optimize the illumination sheet geometry for our specific sample chamber layout. Positioning of the thus created light sheet is done by a gimbal-mounted scanning mirror, which is placed in a plane conjugated to the back-focal plane of the illumination objective lens.

The fluorescent sample is mounted on a three axis sample scanner. It consists of three orthogonal stacked translation stages, where the z-axis is motorized (M105.1B translation stage with DC-Mike linear actuator M232-17 with 7 nm minimum step size from PI, Karlsruhe, Germany), and the x- and y-axis are manually adjustable (100 nm minimum step size). Usually, the sample is mounted in an open water chamber by a refractive index matched agarose cylinder (0.5%-1.0% agarose gel) pushed several millimeters out of a glass capillary [35]. Rotating and tilting of the sample for optimal imaging conditions is realizable. For dynamic measurements, e.g. mobility measurements of diffusing particles, the liquid is filled into a hollow agarose cylinder, which is sealed with silicone paste.

The fluorescence is collected by a water-dipping objective lens (Nikon, 60X NA 1.0) and imaged onto a cooled slow-scan CCD-camera (Photometrics, SenSys KAF-1401E with 1317x1035 pixels, pixel size 6.8 µm^2). For dynamic measurements an electron multiplying CCD-camera (EMCCD) is used (iXon BI DV-860, Andor Technologies,

Belfast, Ireland). To eliminate any scattered laser light a suitable long pass filter is placed in front of the camera. As laser sources we use a green 2 mW HeNe laser (LHGR-0200, Laser2000) emitting at 543 nm, and a 633 nm HeNe laser (Spectra Physics, Model 127, 35 mW). For most measurements 1 to 5 mW were more than sufficient.

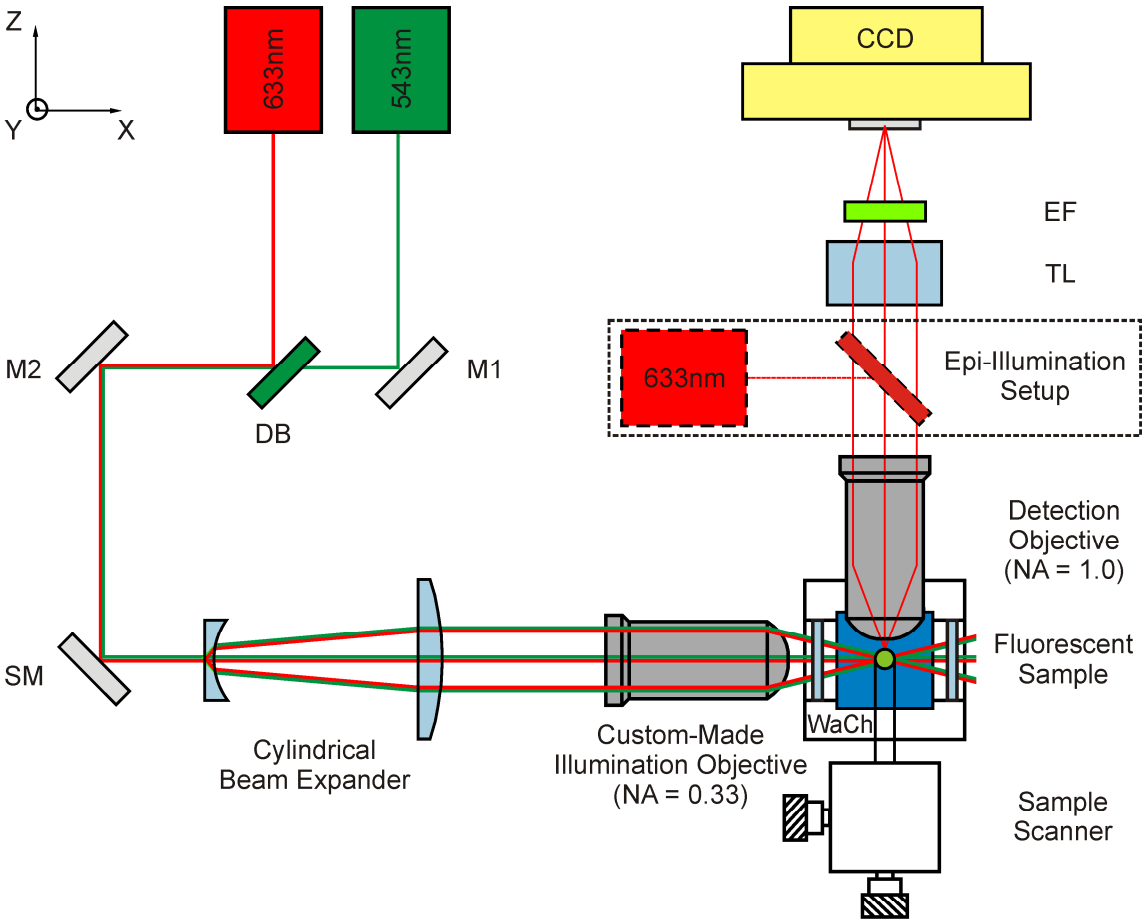

Figure 2.2 Schematic view of the high-resolution SPIM setup. Laser light is guided into a Galilean cylindrical beam expander by mirrors M1 and M2 and a dichroic beam splitter (DB). The beam expander transforms the circular-symmetrical Gaussian beam into an elliptical one. The illumination objective lens focuses the beam into a water chamber (WaCh), and creates a light sheet in the focal plane of the detection objective lens. Positioning of the light sheet can be done with the scanning mirror (SM), which is placed in a conjugated plane of the back focal plane of the illumination objective lens. The sample is moved by a three axis sample scanner, the z-axis is motorized. Fluorescence is collected by a water-dipping objective lens and imaged via a tube lens (TL) onto a CCD-camera. Scattered laser light is blocked by an emission filter (EF). By introducing a dichroic beam splitter into the detection beam path it is possible to use a standard wide-field illumination (dashed box).

2.4 Theory

An essential feature of SPIM is its axial resolution, which is determined by the thickness of the incident light sheet, the NA of the imaging objective lens and the wavelength of the fluorescence light. The objective lens in the excitation beam path focuses the laser beam into a hyperbolic light pattern with a Gaussian intensity distribution perpendicular to the propagation direction. The lateral dimensions of the Gaussian beam are defined by the $\geq 1/e^2$ intensity profile. The thickness of the profile increases with increasing distance to the focus. Twice the Rayleigh range defines the depth-of-focus (**Figure 2.3**). Within the depth-of-focus, along one axis a focused Gaussian beam can be approximated by a rectangle [25]. Therefore, an object positioned in this region is sectioned by a light sheet of almost constant thickness.

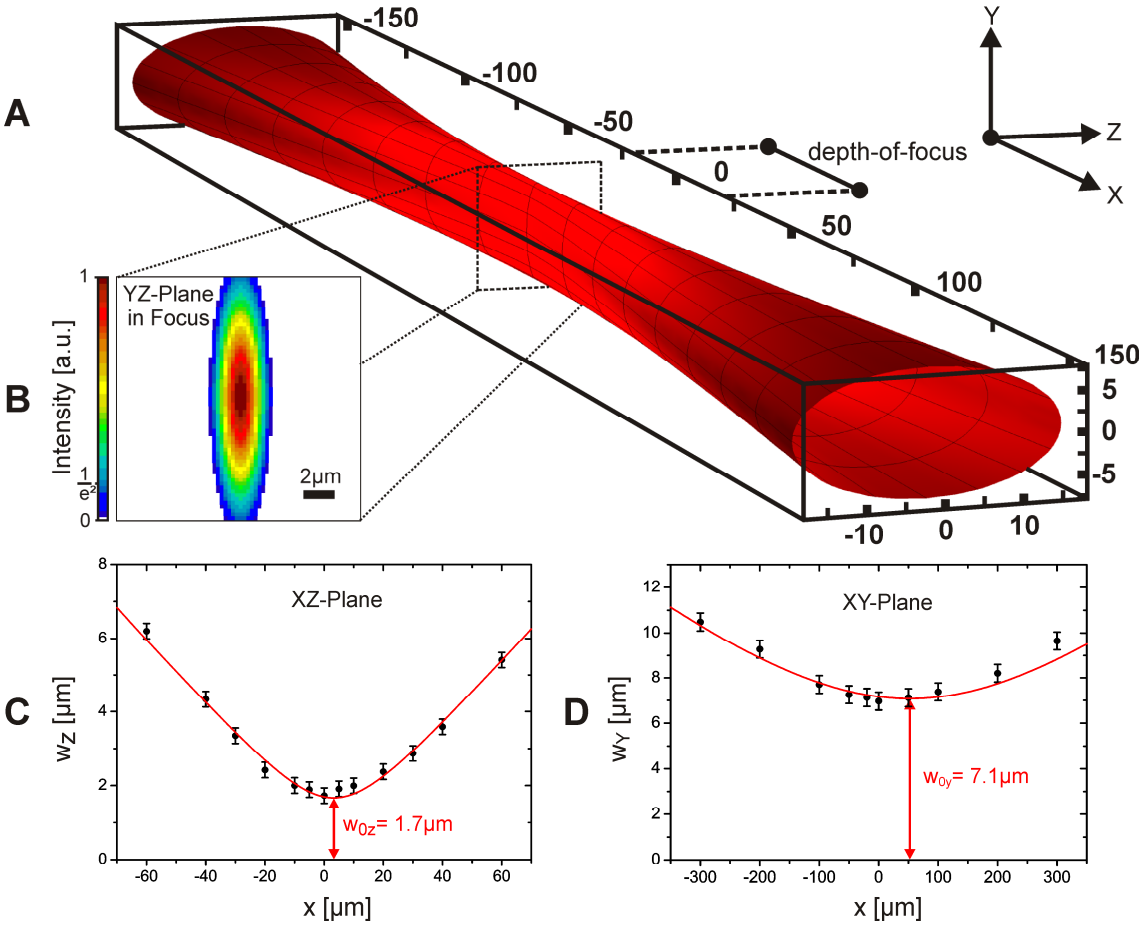

Figure 2.3 Illumination light sheet for λ_0 = 633nm in water (n = 1.33). (**A**) Dimensions ($1/e^2$ distance) and orientation of the light sheet along the illumination axis (x-direction) over a distance of 300 µm. The axial distance, in which the beam width is not greater than a factor of $\sqrt{2}$ of its focal value is known as the depth-of-focus. All units in µm. (**B**) A cut through the elliptical Gaussian intensity distribution of the light sheet at the focus of the detection objective lens. (**C**) and (**D**), experimental data and fit (red line) of the Gaussian beam width in the XZ- and XY-plane [9]. All data points were obtained by knife edge measurements (see section 4.1).

2.4.1 Extension of the light sheet

To discuss the slicing thickness and the resolution of the SPIM, a respective definition has to be chosen. The Rayleigh criterion corresponding to the distance between the central maximum and the first-order-minimum of a diffractive limited intensity distribution is often used. However, it is experimentally inconvenient to determine the first-order-minimum due to a high background or low signals. Other commonly used criteria to specify the width of an intensity profile are the full-width-at-half-maximum (FWHM) and the distance between the maximum intensity I_{max} and the distance, at which it decayed to $1/e^2$ I_{max}. For characterizing the focal thickness and the resolution we use the respective FWHM values.

Table 2.1: Calculated and measured values for the focal height and focal thickness of the light sheet

		λ_0 = 633 nm	λ_0 = 543 nm
$FWHM_Z$ [µm]	ABCD-Law	1.88	1.77
	Ray tracing	1.88	1.78
	Experiment	2.0 ± 0.3	1.7 ± 0.1
$FWHM_Y$ [µm]	ABCD-Law	8.43	5.12
	Ray tracing	8.44	5.20
	Experiment	8.3 ± 0.5	5.3 ± 0.2

In our microscopic setup we produce the illumination pattern approximating a light sheet by coupling an elliptical beam created by a cylindrical lens telescope into the illumination objective lens. The final thickness of the light sheet is depending on the width of the incident beam, the optical parameters of the objective lens, the wavelength and the surrounding medium. The thickness of the light sheet can be determined by ray tracing software or analytically [31,50]. Since the light sheet is formed by an (elliptical) Gaussian beam, the focal thickness can be calculated by the well-known ABCD-law of Gaussian beams in a very straightforward manner [52]. The ABCD-law is essentially a matrix description of beam propagation in optical systems. We were able to calculate all required parameters such as e.g. effective focal length, position of the back focal plane, outgoing beam width for our custom made objective lens by the ray tracing software OSLO Light (Lambda Research Corporation, Littleton, MA, USA). Then we used the ABCD-law to determine the thickness of the light sheet (z-extension), and obtained a FWHM of 1.7 µm and 2.0 µm for the excitation wavelengths 543 nm and 633 nm, respectively. The FWHM values of the light sheet height (y-extension) were 5.3 and 8.3

µm for 543 and 633nm, respectively. Additionally, we determined the focal thickness by the ray tracing program OSLO Light. Both approaches yielded identical results (**Table 2.1**), and agreed well with the experimental results (see below).

2.4.2 Calculation of the point spread function

Like in a confocal microscope, the point spread function (PSF) of a SPIM is determined by the product of the illumination intensity distribution *g(x,y,z)* and the imaging lens blurring function *d(x,y,z)*:

$$h(x,y,z) = g(x,y,z)d(x,y,z) \tag{2.1}$$

The illumination intensity distribution is given by the elliptical Gaussian beam profile of the light sheet. Hence, it can be written as follows:

$$g(x,y,z) = g_0(x)\exp\left(-\frac{y^2}{2\sigma_y^2}-\frac{z^2}{2\sigma_z^2}\right) \tag{2}$$

(2.2)

σ_y and σ_z represent the standard deviations of the Gaussian intensity distribution along the respective axes. The lens blurring function within focal plane of the imaging objective lens is given by the well known Airy formula:

$$d_{lat} = \left(\frac{2J_1(v)}{v}\right)^2 \tag{3}$$

(2.3)

Here, v is given by

$$v = \frac{2\pi}{\lambda_0} n\sqrt{x^2+y^2}\sin\alpha \tag{2.4}$$

J_1 is a first order Bessel function, n the refractive index, λ_0 designates the vacuum wavelength of the image forming light, and 2α is the opening angle of the imaging objective lens. Also, the axial extension of *d(0,0,z)* along the imaging axis is well known [53]:

$$d_{ax} = \left(\frac{\sin\left(\frac{u}{4}\right)}{\frac{u}{4}}\right)^2 \tag{2.5}$$

$$u = \frac{8\pi}{\lambda_0} n\cdot z\sin\left(\frac{\alpha}{2}\right)^2 \tag{2.6}$$

Here, the axial optical coordinate u is written in the form valid for objective lenses with high numerical apertures.

With these equations (Eq.1 – 6) the PSF can be written as:

$$h(x,0,0) = \left(\frac{2J_1\left(\frac{2\pi}{\lambda_0} n \cdot x \sin\alpha\right)}{\frac{2\pi}{\lambda_0} n \cdot x \sin\alpha} \right)^2 \tag{2.7a}$$

$$h(0,y,0) = \exp\left(-\frac{y^2}{2\sigma_y^2}\right) \cdot \left(\frac{2J_1\left(\frac{2\pi}{\lambda_0} n \cdot y \sin\alpha\right)}{\frac{2\pi}{\lambda_0} n \cdot y \sin\alpha} \right)^2 \tag{2.7b}$$

$$h(0,0,z) = \exp\left(-\frac{z^2}{2\sigma_z^2}\right) \cdot \left(\frac{\sin\left(\frac{2\pi}{\lambda_0} n \cdot z \sin^2\frac{\alpha}{2}\right)}{\frac{2\pi}{\lambda_0} n \cdot z \sin^2\frac{\alpha}{2}} \right)^2 \tag{2.7c}$$

The height of the light sheet is much greater than the lateral extent of d(x,y,z), and therefore the exponential term in **Eq. 2.7b** can be neglected. Hence, the PSF in x- and y-direction are approximately identical, and are defined solely by the lens blurring function of the detection objective lens.

These equations (**Eqs. 2.7a-c**) allow us to calculate theoretical estimates for the lateral and axial FWHM of the PSF of the SPIM setup as a measure of its optical resolution. For an imaging wavelength of λ_0 = 680 nm and an imaging objective lens with a NA of 1.0 we determined a FWHM of the PSF of 347 nm for the lateral and 1120 nm for the axial resolution, respectively, by a Taylor expansion of **Eqs. 2.7a-c**.

2.5 Experimental results

2.5.1 Light sheet characterization

To measure the true extension of the light sheet in the water chamber a knife edge test was used [54]. In the knife edge test a razor blade is moved by the sample scanner across the beam path, and the unblocked intensity is measured with a power meter. In this manner the integral of the intensity profile is obtained. For Gaussian intensity

profiles the data can be fitted with an error-function to determine the actual beam widths. In this manner we measured the beam widths along the illumination beam path (x-axis), and fitted the data with the function for the Gaussian beam propagation [25]. The results of this procedure were plotted in terms of the $1/e^2$ diameters of the small and wide waist of the elliptical beam in **Figure 2.3c & d**, respectively. From these data the FWHM values of the beam extensions were deduced, and listed in **Table 2.1**. The experimentally determined values are in excellent agreement with the theoretical estimates. Most importantly, we succeeded in obtaining a very small extension of the light sheet along the imaging axis.

The field-of-view with optimal contrast is suggested by the dimensions of the light sheet, which we define by the Rayleigh length along x- (21 µm) and the FWHM values of the y- (5.3 µm) and z-direction (1.7 µm) for 543 nm excitation light. For the red HeNe laser emitting at 633 nm, these dimensions were 29 µm x 8.3 µm x 2.0 µm.

2.5.2 Optical resolution

The 3D extension of the SPIM-PSF was measured with red fluorescent microspheres using excitation with 633nm He-Ne laser light. Microspheres with diameters of 40 nm and 200 nm (Invitrogen, Karlsruhe, Germany) were used for lateral and axial resolution measurements. The microspheres were embedded in agarose and acted as point-like light sources, which were moved in 100 nm steps along the optical detection axis while being imaged by the CCD camera. The intensity distribution within the focal plane and along the detection axis was plotted, and the data were approximated by Gaussian functions to determine the FWHMs of the lateral and axial resolution (see **Figure 2.4**).

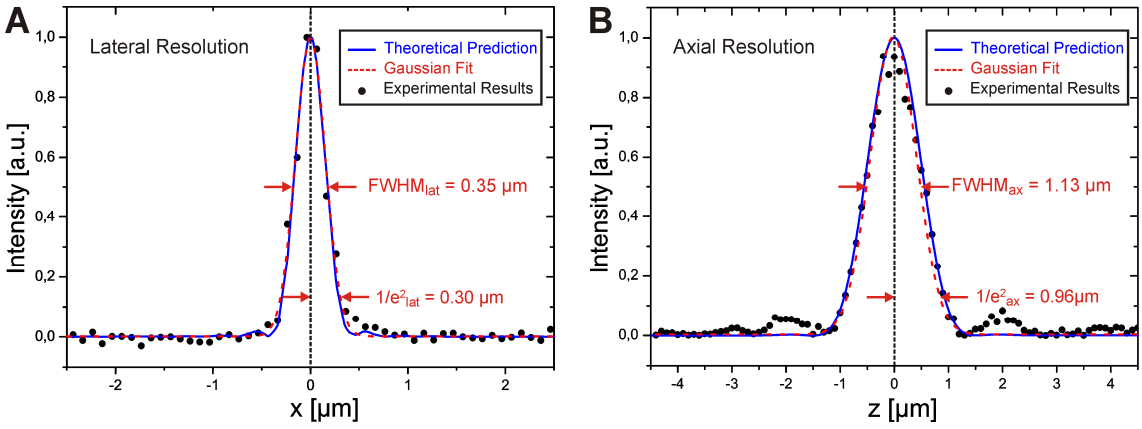

Figure 2.4 Comparison of calculated and measured PSF. Experimentally determined (**A**) lateral and (**B**) axial point spread functions. Fluorescent microspheres were illuminated with a 633 nm He-Ne Laser, and imaged with a water-dipping objective lens (NA 1.0). The data were fitted with a Gaussian function to determine the FWHM (red, dashed lines). The theoretical curves were calculated with Eqs. 7a and 7c for the lateral and axial PSFs, respectively.

We obtained 350 ± 40 nm and 1.13 ± 0.02 µm for the lateral and axial FWHM, respectively, for an emission wavelength of 680 nm. These results were in excellent agreement with the theoretical estimates (347 nm and 1120 nm, see above). We achieved an increase in axial resolution of more than 50% compared to previously presented results [50,55].

2.5.3 Contrast improvement by SPIM

One of the beneficial consequences of optical sectioning microscopy, and hence the perpendicular illumination-imaging configuration, is a significantly improved image contrast compared to a standard epi-illumination microscopy in thick specimen. We verified this feature by imaging a sample containing fluorescent microspheres on a homogeneous fluorescent background with both illumination geometries. To this end we prepared a sample of diluted fluorescent microspheres (Invitrogen, dark red, diameter 210 nm), which were fixed and mounted in 1% agarose containing varying concentrations of dextran molecules (500 kDa), which was covalently conjugated to Atto633 (Atto Tec, Siegen, Germany). The dye concentrations were determined by reference measurements in a confocal laser scanning microscope (LSM510 Meta, Zeiss, Jena, Germany). The specimen could be illuminated for extended time periods without

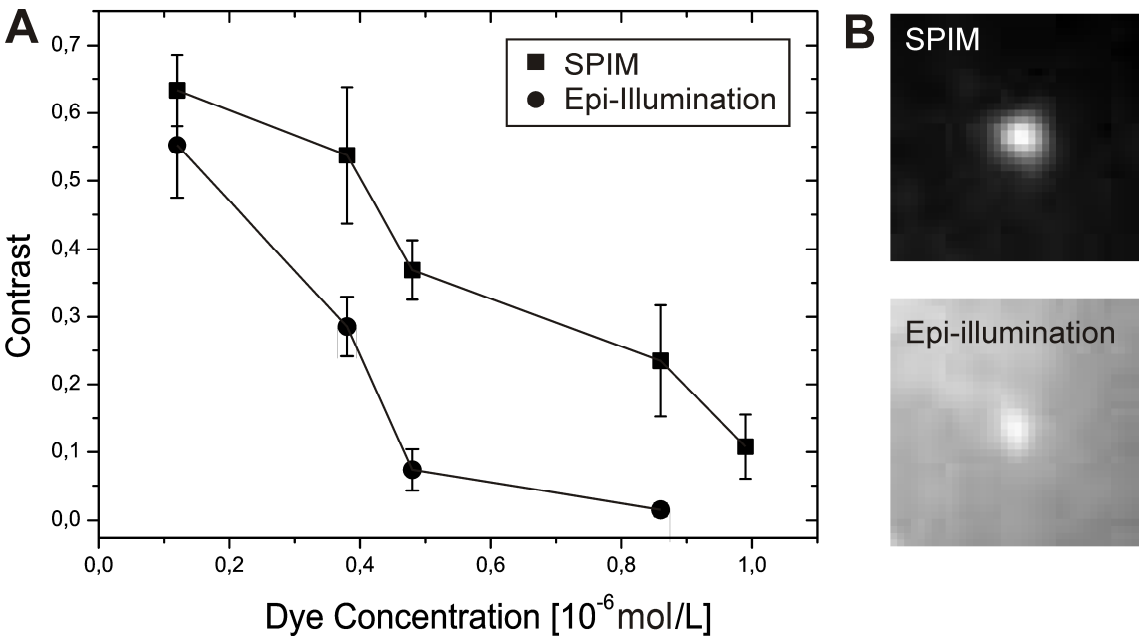

Figure 2.5 Contrast improvement in SPIM versus epi-illumination microscopy. (**A**) Contrast values of dark red fluorescent 210 nm microspheres were determined using SPIM and epi-fluorescence microscopy as a function of homogeneous dye (Atto633) concentration in sample. SPIM images showed a strong background reduction, leading to a distinct contrast improvement. The maximum fluorescent intensity was kept at the same level for both cases. (**B**) Example frames showing the beads upon SPIM and epi-illumination microscopy at a background dye concentration of 460 nM.

any significant photo-bleaching. Switching between SPIM and epi-illumination was achieved by inserting a dichroic beam splitter into the detection beam path (see **Figure 2.2**). Imaging was performed in both cases with the same NA 1.0 objective lens. Thereby we could image the same specimen region with both illumination configurations. Laser power was adjusted such that in both imaging modes approximately identical maximum fluorescence signals were obtained.

Contrast, C, is defined by the maximum fluorescent intensity of the signal, I_{max}, above background, I_{min}, divided by the sum of both values, or $C = (I_{max}-I_{min})/(I_{max}+I_{min})$. Datasets were acquired by moving the specimen axially trough the focal plane. Maximum intensities were determined at the beads´ brightest pixels, I_{min} was the averaged intensity of the background. For each data point at least 8 beads and background values were determined. The contrast values for both illumination types were plotted in **Figure 2.5** as a function of dye concentration up to 1 µM. Obviously, the image contrast was clearly superior when SPIM was used. At high fluorophore concentration, where imaging with epi-illumination becomes problematic, obtaining distinct signals with SPIM is still feasible. Two images demonstrating this effect for a dye concentration of 460 nM were shown in **Figure 2.5b**. Here, the contrast improvement by SPIM was especially striking. It should be noted that background fluorescence is strongly dependent on the sample characteristics. Consequently, the quantitative impact of the illumination geometry varies strongly with the specimen. In general, however, SPIM allows observation of single particles at higher concentrations, where in an epi-fluorescence microscope the single particle signals would be dominated by out-of-focus background fluorescence.

2.5.4 Imaging and tracking of quantum dots in aqueous solution

Previous realizations of SPIM focused onto the special imaging properties with regard to the obtainable resolution. We see an especially great potential in applying the technique to single particle tracking in 3D-extended samples, which suffer from inherently low SNR when epi-illumination is used. 3D particle tracking is based on three requirements, namely high resolution, high contrast and high imaging rates. To demonstrate the capabilities of our SPIM setup to meet these requirements we visualized the diffusion of nanometer-sized quantum dots in aqueous solution. As a sample we used streptavidin-conjugated red fluorescent quantum dots (λ_{em} = 655nm; Invitrogen) in 0.5% BSA buffer solution at a concentration of 200 pM. The liquid sample was mounted in a hollow agarose cylinder as described in section 2. For excitation we used the 633 nm He-Ne laser. Imaging was performed with a fast, electron-multiplying CCD camera (128x128 pixels, iXon DV 860 BI, Andor Technologies, Belfast, Ireland) supplemented with a 4X magnifier yielding a pixel size

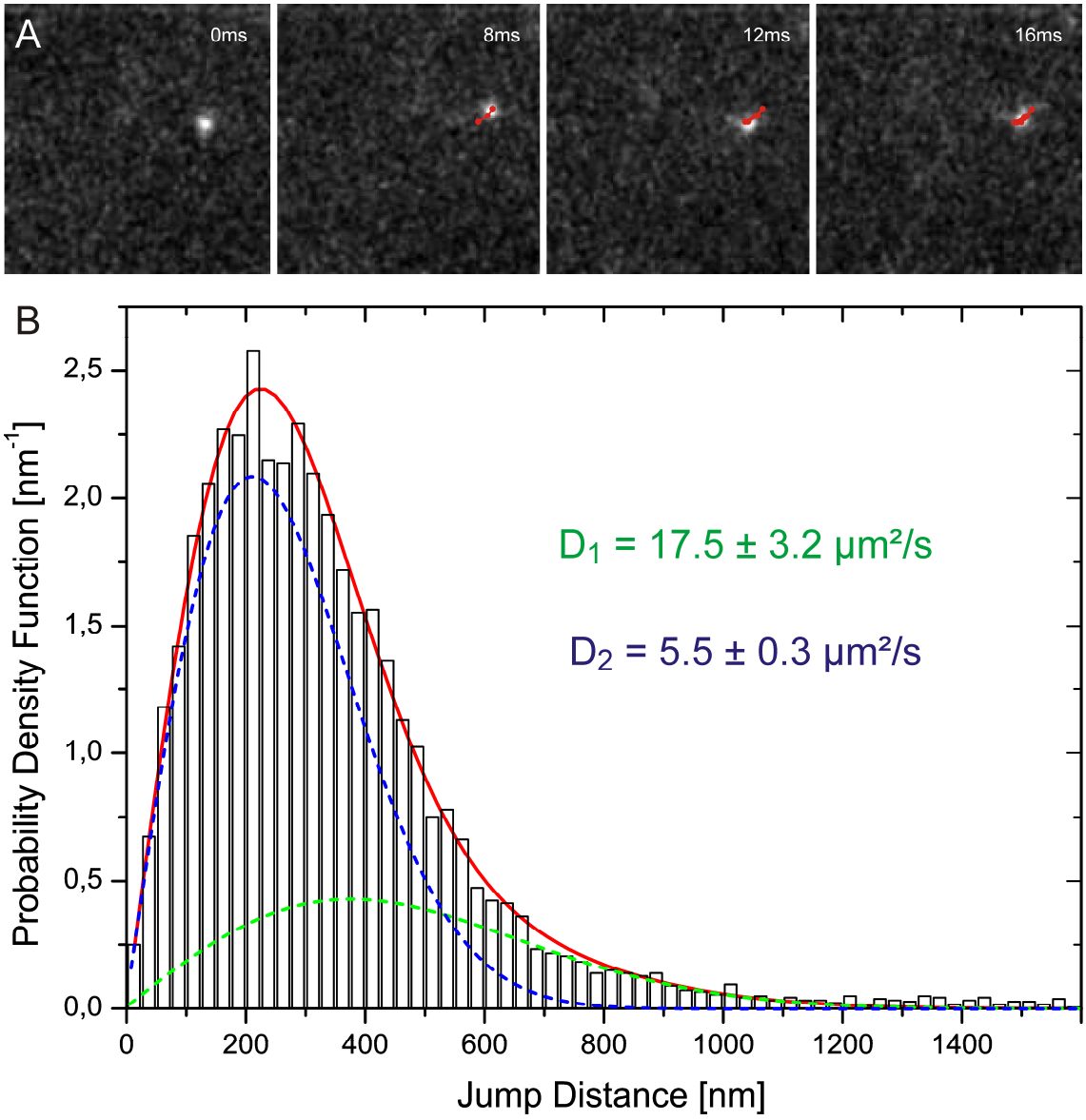

Figure 2.6 Diffusion of single quantum dots in aqueous solution (**A**) Single frames illustrating the diffusion of a red fluorescent quantum dot (λ_{em} = 655nm). The frames were acquired with an integration time of 4 ms. In each frame the position of the dot was determined, and assembled into the trajectory (shown in red). (**B**) A jump distance histogram was fitted (red) with the probability density function for determination of the diffusion coefficients. The histogram comprised two components, which were due to Qdot monomers (green) and Qdot aggregates (blue).

of 100 nm in the object plane. Movies from mobile quantum dots were acquired using SPIM with a single frame integration time of 4 ms at a frame rate of 243 Hz. Several example frames from a movie were shown in **Figure 2.6a**. To extract the diffusion coefficient from the image data we traced the diffraction-limited quantum dot signals using a commercial ImageJ plug-in for particle tracking (IL Tracker Version 1.01b), and analyzed the jump distance distribution of the quantum dots from frame to frame [56].

In **Figure 2.6b** we plotted the normalized frequency distribution in a histogram, and subsequently fitted the data by the following equation [56]:

$$p(r,\Delta t)=\sum_i \frac{A_i}{2D_i\Delta t} r\cdot\exp\left[-\frac{r^2}{4D_i\Delta t}\right] \tag{2.11}$$

The equation describes the jump distance probability density function for i diffusive species, where A_i is the fractional amount of each component. D_i is the respective diffusion coefficient and r the jump distance covered in the time interval Δt. In this manner we determined the diffusion coefficients of Qdots655 as $D_1 = 17.5 \pm 3.2$ µm²/s, which was in perfect agreement with earlier results [57]. It is well known that Qdots tend to aggregate in solution. Therefore, we detected a slow diffusing fraction with $D_2 = 5.5 \pm 0.3$ µm²/s besides the fast diffusing Qdots, which was presumably due to larger quantum dot aggregates. This experiment demonstrated the capability of the SPIM setup for single particle tracking in a very direct manner. Usually in single molecule tracking experiments in wide-field microscopy require very low sample concentrations, otherwise the background fluorescence inhibits detection of single particles.

2.6 Conclusions

We constructed an optical sectioning microscope based on selective focal plane illumination featuring an especially thin illumination slice. We used the ABCD-law of Gaussian beams and ray-tracing to calculate the characteristics of our illumination sheet, which were verified by quantitative measurements. Thus we demonstrated various improvements compared to previous reports, for instance an axial slicing FWHM of 1.7µm at λ_0 = 543nm and 2.0 µm at λ_0 = 633nm only, as well as a lateral resolution of 350 nm and an axial resolution of 1.13 µm, both at λ_0 = 680nm. The striking enhancement of the contrast suggests that SPIM is a valuable tool to observe the dynamics of single particles and molecules under critical conditions such as weak signals and high particle concentration. This was demonstrated by imaging and analyzing the rapid diffusive motion of single streptavidin-conjugated quantum dots in aqueous solution at a time resolution of 4 ms. Altogether, the development of this high-resolution SPI-microscope eliminated major problems in single molecule microscopy in 3D-extended specimen. Last not least, this instrument will allow the direct tracking of single particles within living cells in full three dimensions by keeping a selected particle in focus and adjusting the axial sample position using a feed-back loop.

Author Contributions

J.R. created the instrument concept; J.R. developed the optical design; J.R. derived and performed theoretical analysis; J.R., R.V. and J.P.S. designed experiments; J.R. performed and analyzed experiments; J.R. and U.K. wrote the manuscript.

3 Light sheet microscopy for single molecule tracking in living tissue

Jörg G. Ritter, Roman Veith, Andreas Veenendaal, Jan-Peter Siebrasse and Ulrich Kubitscheck. PLoS One 5: e11639 [58]

3.1 Abstract

Single molecule observation in cells and tissue allows the analysis of physiological processes with molecular detail, but it still represents a major methodological challenge. Here we introduce a microscopic technique that combines light sheet optical sectioning microscopy and ultra sensitive high-speed imaging. By this approach it is possible to observe single fluorescent biomolecules in solution, living cells and even tissue with an unprecedented speed and signal-to-noise ratio deep within the sample. Thereby we could directly observe and track small and large tracer molecules in aqueous solution. Furthermore, we demonstrated the feasibility to visualize the dynamics of single tracer molecules and native messenger ribonucleoprotein particles (mRNPs) in salivary gland cell nuclei of *Chironomus tentans* larvae up to 200 µm within the specimen with an excellent signal quality. Thus single molecule light sheet based fluorescence microscopy allows analyzing molecular diffusion and interactions in complex biological systems.

3.2 Introduction

The observation of single molecules in living cells allows the study of physiological key processes such as signal processing, intracellular transport and gene expression [24]. However, there are no experimental tools to perform such experiments in intact, large biological objects in three dimensions such as tissue or embryos [19]. The internal fluorescence background in such specimen is simply too high making single molecule imaging very problematic if not completely impossible. An elegant solution presents light sheet based fluorescence microscopy (LSFM), which is an adaptation of classical "Ultramicroscopy" [34] to fluorescence microscopy. Although LSFM is a new technique, it has intensely been developed from its invention until now and had already a remarkable success in imaging complex three dimensional (3D) multicelluar organisms, e.g. embryos, zebrafish or mouse embryos, *in vitro* and *in vivo* [26,30,35,36,41,43,44,46,49,50,59].

LSFM uses a thin, focused light sheet to illuminate the sample orthogonally to the detection pathway. Therefore only a narrow region near the object plane of the observation objective lens is illuminated and fluorophores outside this plane are not excited and do not generate a background signal. Furthermore, fluorophores outside the

focal plane are not photo-damaged as they would be upon epi-illumination. These instrumental characteristics produce an optical sectioning effect, improved contrast and allow very long observation times of sensitive samples [27].

However, LSFM is not limited to the optical sectioning of comparatively large samples. Here we demonstrate that single molecule imaging in solution and especially in living tissue substantially profits from using light sheet illumination, because single molecule experiments are extremely sensitive in terms of background fluorescence and photo-bleaching. Other optical sectioning schemes like total-internal-reflection microscopy (TIRF) [60] or highly inclined laminated optical sheet microscopy (HILO) [22,23] already became very successful in this field, but because of their limited penetration depth they are not suitable for single molecule tracking in extended 3D samples. Here, light sheet based microscopy would be an ideal solution for single molecule experiments in thick specimen [47,61]. We describe the development and application of a light sheet based fluorescence microscope, which combines the benefits of optical sectioning, the detection efficiency of high numerical aperture (NA) objective lenses (NA > 1.0) and parallel image acquisition. Thus it became possible to image the dynamics of single molecules with unprecedented speed and precision *in vitro* and *in vivo* deep within a living specimen. The utility of this instrument was first shown by imaging and tracking of different molecular species in buffer at the single molecule level and the imaging contrast was directly compared to data acquired with classical epi-illumination. The advantages for *in vivo* single molecule imaging in 3D-extended biological tissue were demonstrated by observing tracer molecules within salivary gland cell nuclei of *C. tentans* larvae. From this experiment we could determine the effective intranuclear viscosity, a parameter which affects the mobility of all molecules and particles in the nucleus. Then we studied the trafficking of single, native mRNA molecules in *C. tentans* salivary gland cell nuclei, which were made visible by a fluorescently labeled RNA binding protein, hrp36. This protein is the *C. tentans* homologue of the mammalian RNA binding protein hnRNP A1 [20,62]. Our new imaging approach yielded images of single RNA particles with a superb contrast, which allowed their tracing at high frame rates and at high spatial resolution about 100 to 200 µm deep within the salivary gland.

3.3 Results

3.3.1 Instrument design

Our instrument is quite different from other LSFMs, because several new design challenges had to be met. While most existing setups [36,41,59,61,63] use large specimen chambers together with water-dipping objectives mounted horizontally to image 3D extended specimen, we chose to exploit the stage of a commercial inverted

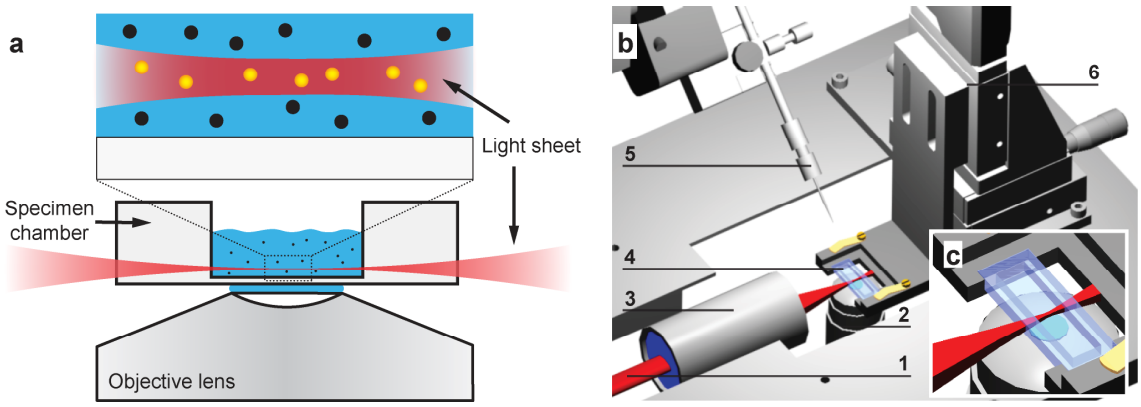

Figure 3.1 Concept and experimental realization of single-molecule light sheet based fluorescence microscopy. (**a**) The illuminating laser light sheet was focused into a glass sample chamber, whose bottom had standard cover slip thickness. Single molecule fluorescence was collected by a high NA water immersion objective and detected by a fast EMCCD. Due to the optical sectioning effect only fluorescence in the focal region was excited and no out-of-focus fluorescence contributed to the image (enlarged view). (**b**) Experimental realization on the stage of an inverse microscope. An elliptical laser beam (1) is focused by the illumination objective (3) into the sample chamber (4) creating the light sheet. Imaging occurred perpendicular to the illumination axis by a high NA lens (2). Specimen could be moved through the light sheet by a motorized translation stage (6). Optionally, specimen could be microinjected (5). (**c**) Enlarged view of the specimen chamber and the light sheet.

microscope. Furthermore, we used a high NA water immersion objective lens for imaging, which was needed to maximize the light detection efficiency (**Figure 3.1**). The custom-built sample chamber featured a glass bottom with standard coverslip thickness (0.17 mm), had glass walls such that the illumination light could be introduced from the side and was placed on a motorized stage (**Material & Methods**). The light sheet had to be created within the working distance of 280 µm of the detection objective and was produced by a dedicated illumination objective lens with a high NA in order to achieve a thin light sheet with an axial extension of only 3 µm full-width-at-half-maximum (FWHM). The high NA of the illumination objective resulted in a strong convergence of the focused beam and a corresponding short working distance of the illumination objective. A special long working distance illumination objective (10x; NA = 0.28; working distance, 33.5 mm; Mitutoyo, Japan) met all construction conditions. We built the light sheet illumination on a standard microscope body in order to increase its usability, because this allowed us to switch between fluorescence imaging exploiting the light sheet advantages and standard microscopy techniques like phase or differential interference contrast (DIC). We chose an inverted stage because the specimen chamber had to be accessible for a microinjection device (**Figure 3.1b**).

3.3.2 Light sheet characterization

The actual light sheet dimensions defined the field of view and optical sectioning capability of the microscope. To measure the light sheet dimensions a aqueous solution

of ATTO647N was filled into the sample chamber at a concentration of 100 µM. Its illumination directly revealed the 3D extensions of the light sheet, which were imaged and quantified (**Figure 3.2**). The minimal FWHM along the illumination axis was 19.7 ± 0.1 µm. Upon turning the elliptical illumination beam by 90° the thickness of the light

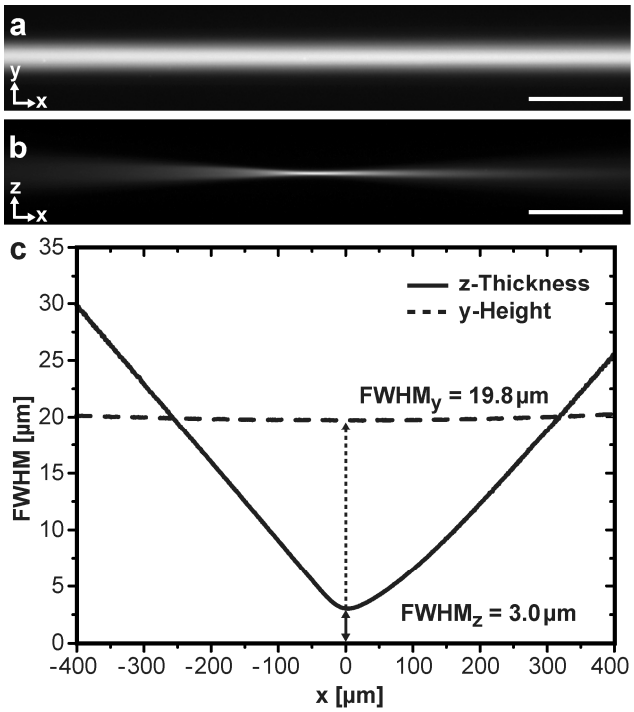

Figure 3.2 Dimensions of the light sheet. The red light sheet (λ = 638 nm) was formed in a solution with a 100 µM concentration of ATTO647N. It was imaged with a 10x NA 0.3 objective by a slow-scan CCD-camera (**Material & Methods**). Lateral (**a**) and axial (**b**) extension of the light sheet. Scale bars, 100 µm. (**c**) Full-width-at-half-maximum (FWHM) values of the light sheet along the illumination (x-) axis. Light sheet geometries of all excitation wavelengths were summarized in **Table 3.1.**

Table 3.1 Light sheet dimensions for different excitation wavelengths

λ [nm]	Axial width (z) [µm]	Y-height [µm]
637	3.0 ± 0.1	19.7 ± 0.1
532	3.0 ± 0.1	19.6 ± 0.1
488	2.9 ± 0.1	19.6 ± 0.1

sheet could directly be visualized and analyzed in a similar manner. Its axial width was 3.0 ± 0.1 µm FWHM for an excitation wavelength of 638 nm. The extension of the usable light sheet along the illumination axis can be defined by twice the Rayleigh length of the Gaussian beam, so that the field of view for optimal contrast was

approximately 84 µm x 20 µm. Similarly, for excitation wavelengths of 488 nm and 532 nm the axial FWHM values were determined as 2.9 ± 0.1 µm and 3.0 ± 0.1 µm, respectively (**Table 3.1**). The optical sectioning thickness was comparable for all three wavelengths as it was expected for an achromatic illumination.

3.3.3 Imaging of single molecules in solution

To demonstrate the sensitivity and speed of the instrument we investigated the mobility of single molecules in aqueous solution. An increased contrast was expected due to the lack of out-of-focus fluorescence, such that it should be possible to image and track smaller (and faster) molecules at the single molecule level than ever before [57].

For a quantitative comparison between LSFM and standard epi-illumination we compared the image contrast in image sequences of single, fluorescently labeled 500 kDa dextran molecules recorded at almost 100 Hz (**Figure 3.3** and **SI Movie 1**[64]). As expected the contrast was clearly superior (0.97) when the light sheet illumination was used versus epi-illumination (0.37) for the given tracer concentration (**Material & Methods**). The signal-to-noise-ratio (SNR) increased by a factor of 4 yielding a significantly improved localization precision [65].

Table 3.2 Diffusion constants of various probe molecules measured by single-molecule LSFM in aqueous solution

Molecules	Radius [nm]	D_{MSD} [µm²/s]	D_{FCS} [µm²/s]	D_{Theory} [µm²/s]
500 kDa dextran	26.5	8.2 ± 0.1	7.5 ± 0.8	8.1
Ovalbumin	2.4	88 ± 2	92 ± 5	89
Oligonucleotide	a = 5, b = 0.5	130 ± 14	120 ± 2	120

We imaged and analyzed three different molecular species with different sizes and shapes, namely 500 kDa dextran molecules with a Stokes radius of 26.5 nm [20], ovalbumin (MW 43 kDa) with a Stokes radius of 2.4 nm [57], and fluorescently labeled 30mer oligonucleotides (long-rod, with equatorial radii a = 5 nm and b = 0.5 nm [66]). The theoretically expected diffusion coefficients covered three orders of magnitude (**Table 3.2**). Respective image sequences were recorded at 483 Hz; in all cases we could observe and follow the trajectories of single probe molecules (**SI Movie 2**[64]). The mean-square-displacements (MSDs), $\langle x^2 \rangle$, were extracted from the single molecule trajectories and plotted as a function of time, t, to determine the diffusion constants, D, of the probe molecules according to $\langle x^2 \rangle = 4Dt$ (**Figure 3.3**). In this manner we found

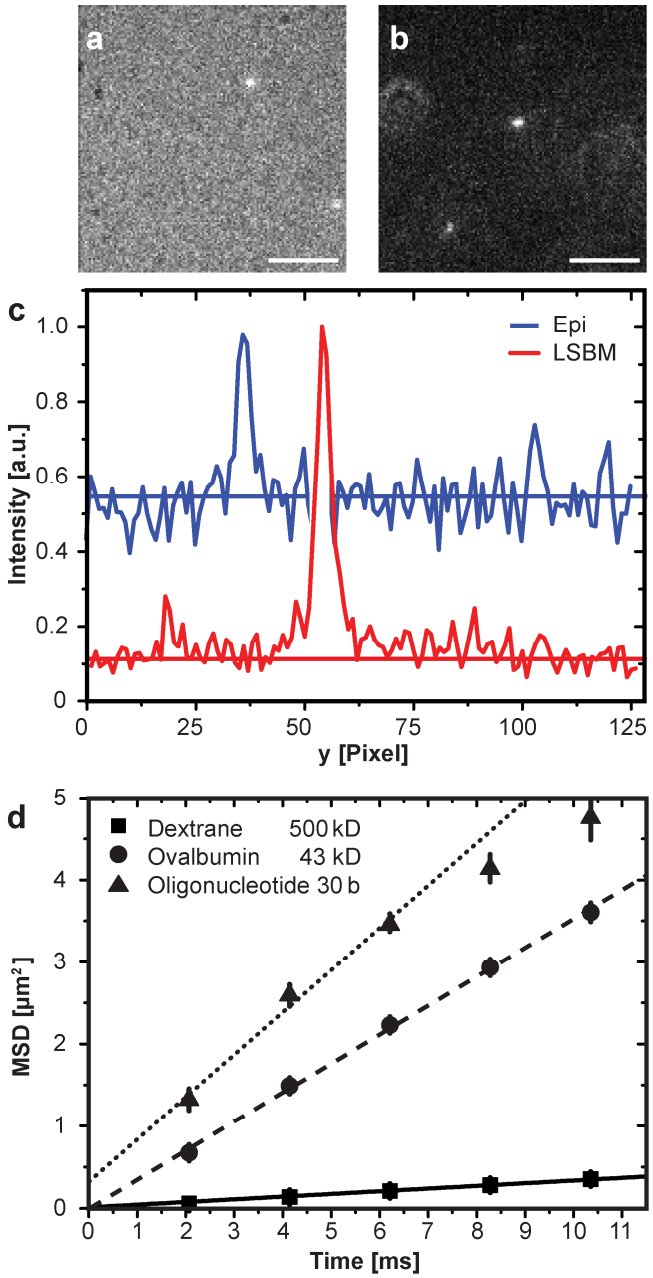

Figure 3.3 Single molecule visualization and tracking in solution. (**a**) Standard epi-illumination fluorescence image of single ATTO647-labelled dextran molecules (MW 500 kDa) diffusing in transport buffer acquired at an exposure time of 10 ms. Scale bar, 5 µm (**b**) The same sample was imaged upon light sheet illumination demonstrating the striking contrast improvement (see **SI Movie 1**[64]). Scale bar, 5 µm. (**c**) Intensity profile along a vertical line through the central pixels of the two brightest molecules shown in (a) and (b) illustrating the contrast improvement. (**d**) MSDs as a function of time for different molecules; dextran 500 kDa (boxes), ovalbumin (circles), and a 30mer oligonucleotide (triangles). Movies were recorded for all three species with 483 Hz. The data were fitted by lines to determine the diffusion coefficients. The error bars represent the standard deviation. The results were summarized in **Table 3.2**. (see **SI Discussion 3.6.1**).

diffusion coefficients for 500 kDa dextranes, ovalbumin and 30mer oligonucleotides of $D_{dextran}$ = 8.2 ± 0.1 µm²/s, D_{ova} = 88 ± 2 µm²/s and D_{30mer} = 130 ± 14 µm²/s. To validate these data we performed measurements by fluorescence correlation spectroscopy (FCS) (**Table 3.2**). In all cases we found an excellent correspondence between single molecule tracking, FCS and the theoretically estimated diffusion coefficients. These values measured at a viscosity of 1cP also served as references for the measurement of the effective viscosity within the nucleoplasm of salivary gland cell nuclei of *C. tentans* larvae.

3.3.4 In vivo tracking of single mRNP particles in the nucleus

In a next step we employed LSFM for *in vivo* imaging within a 3D extended biological specimen with large dimensions compared to plain monolayer culture cells. As a suitable model system we chose the salivary gland cell nuclei of larvae of the dipteran *C. tentans* [67,68,69]. This system was well suited to demonstrate the imaging capabilities of the single molecule LSFM, because the salivary glands are an intact, large and living tissue. The salivary glands have a complex structure and dimensions of roughly 700 µm x 2000 µm x 250 µm as sketched in **Figure 3.4a**. The gland cells contain large nuclei with diameters of 50-70 µm (**Figure 3.4a**). Each gland cell nucleus contains four polytene chromosomes being roughly 10 µm in diameter. Each polytene chromosome is made up of 8000 to 16000 perfectly aligned chromatids [69], which form a distinct chromosome band structure. The remaining nucleoplasm is devoid of chromatin [70]. This is an ideal system to study the regulation of mRNA trafficking without the possibly retarding effect of chromatin (see **SI Figure 3.5**).

Chromosome IV contains two especially active transcription sites, the so called Balbiani Rings (BRs) 1 and 2. Three genes with a length of up to 40 kb are transcribed here and are processed to large BR mRNA particles (BR mRNPs) with a diameter of roughly 50 nm, which move randomly in the nucleoplasm after their release from the gene. In the nucleoplasm of the salivary gland cell nuclei the BR mRNPs have a density of 10-100 particles per µm³ and form about 90% of the present mRNPs [71]. The glands were dissected out of the larvae and placed inside the specimen chamber for microscopy. In this large biological system visualization of single, fluorescently labeled BR mRNPs and tracking their movements was problematic, since the nuclei had a distance to the cover slip of 100 to 200 µm. In a conventional fluorescence microscope single molecule imaging at such a depth within the specimen is almost impossible, because the SNR is

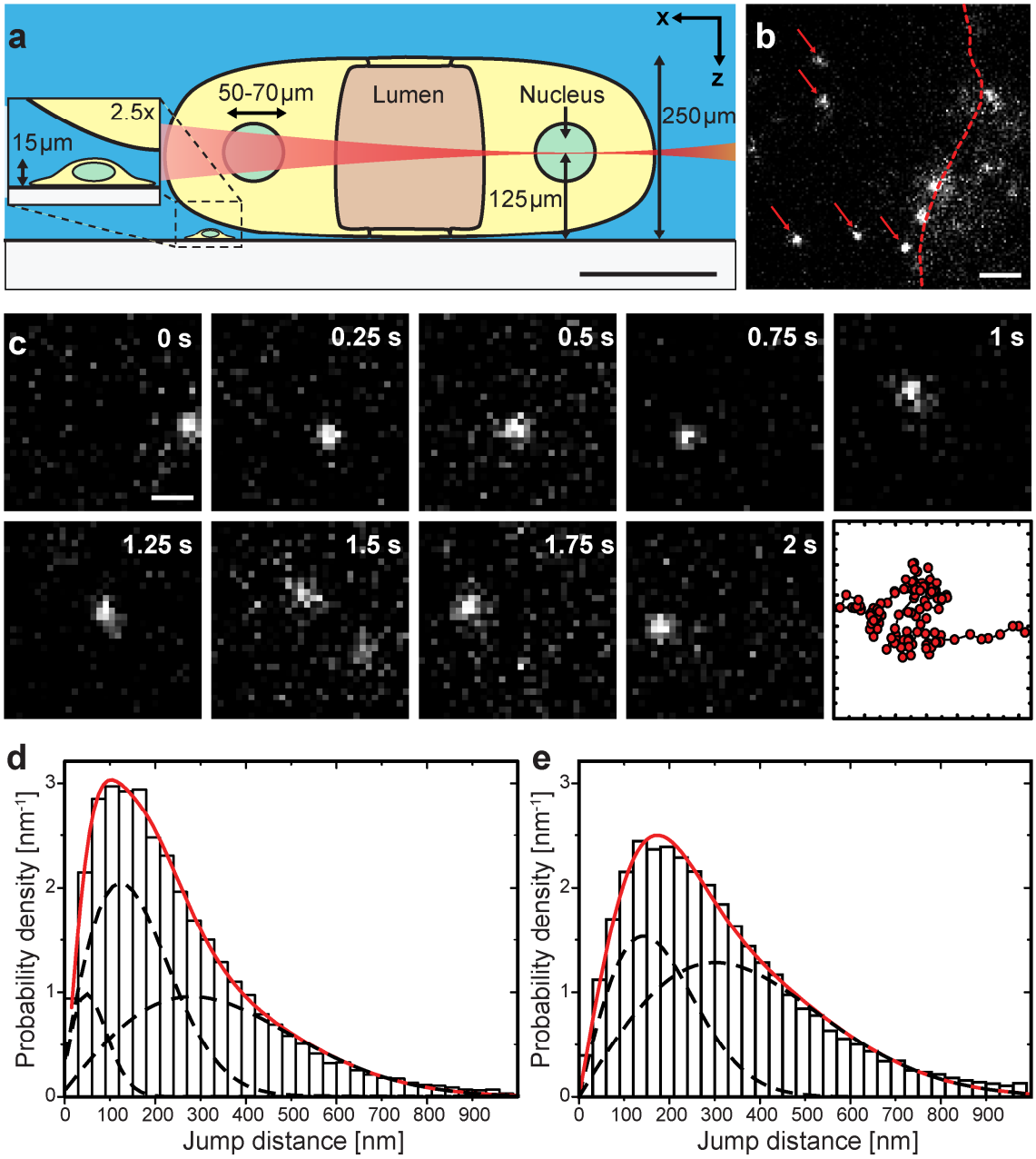

Figure 3.4 Single molecule tracking in the living salivary gland cell nucleus of the C.tentans larvae. (**a**) Scheme of the light sheet illumination of a salivary gland cell nucleus. The salivary glands are a living tissue with dimensions much larger than that of e.g. cell culture cells. Scale bar, 200 µm. (**b**) Typical image showing single diffusing BR mRNPs (red arrows) labeled with microinjected hrp36. The dashed line indicates the position of the nuclear envelope. Scale bar, 3 µm. (**c**) Time series of a moving mRNP particle marked by single ATTO647N-labelled hrp36 molecules inside the nucleus. The last panel shows the complete trajectory. Frame rate, 49.46 Hz; Scale bar 1 µm. **(d)** Normalized jump distance distribution of BR mRNP particles and microinjected 500 kDa dextran molecules (**e**) inside salivary gland cell nuclei for a time interval of 20 ms. The red line showed the complete fitting function and the dashed lines indicate the contributions of the single components (see **Material & Methods**). Fitting results were summarized in **Table 3.3**.

Table 3.3 Mobility of 500 kDa dextran molecules and mRNPs inside living salivary gland cell nuclei

	500 kDa dextran	**mRNP particle**
D_1 [µm²/s]	2.3 ± 0.2	2.0 ± 0.2
Fraction 1	64 ± 3 %	45 ± 3 %
D_2 [µm²/s]	0.5 ± 0.1	0.50 ± 0.05
Fraction 2	34 ± 3 %	45 ± 2 %
D_3 [µm²/s]	-	0.08 ± 0.01
Fraction 3	-	10 ± 1 %

low due to a high fluorescence background (see **SI Figure 3.6**). For labeling of the mRNPs we used the characteristics of the RNA-binding protein hrp36, which is an important structural component of BR mRNPs with about 120 copies contained in a single BR mRNP [72]. Hrp36 is part of the mRNPs from the genes in the nucleus to the polysomes in the cytoplasm and it is associated with the mRNPs even during passage of the particles through the nuclear pore complex. Within living salivary glands BRmRNPs are continuously formed in the nuclei, and therefore we could label the BR mRNPs by *in vivo* microinjection of fluorescent ATTO647N-labeled hrp36 (**Material & Methods**). The formation of BR mRNPs takes approximately 10 minutes. Localization and microinjection of the nuclei inside the salivary gland cells was performed using bright-field imaging, since the nuclei were easily distinguishable from the cellular interior.

Immediately after microinjection single hrp36 could not be imaged at a frame rate of 50 Hz, because this frame rate was not high enough to image single, small proteins. However, after about 10 min single hrp36 signals became visible. Presumably, they were then incorporated into the 50 nm sized BR mRNPs, which diffused at a much lower rate [20]. Hence, in this manner the movements of single, native BR mRNPs in the nucleoplasm could be studied. We compared the integrated signal intensity of BR mRNPs with that of single ATTO647N molecules, and concluded that the mRNPs carried single Atto647N-labeled hrp36 molecules. Due to its optical sectioning capability LSFM was especially well suited for this task. Only BR mRNPs in the focal region were illuminated and visualized (**Figure 3.4**). This resulted in excellent SNRs and clearly longer trajectories of the BR mRNPs (**Figure 3.4c** and **SI Movie 3**[64]) than in previous experiments [20]. In order to analyze the mRNP mobility, we determined the positions along the single particle trajectories with a localization precision of $\sigma = 40$

± 12 nm (**Material & Methods**), and plotted the jump distances between consecutive frames in histograms (**Figure 3.4d**). These histograms can be analyzed by a multi-component analysis. We found three different mobility fractions of the BR mRNPs. A fast fraction (45%) with a diffusion coefficient of D_1= 2.0 ± 0.2 µm²/s, a slower fraction (45%) with a D_2= 0.5 ± 0.05 µm²/s and a strongly retarded fraction (10%) with a D_3= 0.08 ± 0.01 µm²/s.

To compare the mRNP mobility with inert molecules of a similar geometrical size we microinjected fluorescent dextran molecules (MW 500 kDa) with a Stokes radius of 26.5 nm into salivary gland cell nuclei. Using LSFM it was straightforward to image these dextran molecules within the nuclei with an excellent signal quality, and to track them for extended time periods (**SI Movie 4**[64]). From the resulting trajectories we determined the jump distance histogram as described above. In contrast to the situation in buffer the analysis now revealed the existence of two different mobility components, a fast one (64%) with D_{fast}= 2.3 ± 0.2 µm²/s and a slower one (36%) with D_{slow}= 0.5 ± 0.1 µm²/s (**Figure 3.4e**). A comparison of D_{fast} with the diffusion coefficient measured in buffer solution yielded the effective nuclear viscosity in these cell nuclei as $\eta = 3.6 \pm 1$ cP corroborating previous FRAP and single particle tracking results [20]. We speculated that the occurrence of the second, reduced diffusion constant D_{slow} was due to the molecularly crowded intranuclear environment [73]. The comparison of dextran and mRNP mobility suggested that D_1 and D_2 were related to the diffusion of the mRNPs in the crowded nuclear interior, because they were almost identical to D_{fast} and D_{slow} of the tracer. However, the third, quite slow mRNP diffusion coefficient, D_3, was not observable for the inert dextran. We concluded that this mobility component was caused by interactions of the BR mRNPs with large intranuclear structures.

3.4 Discussion

Single molecule observation in large, living samples is problematic. Single molecule microscopy using conventional epi-illumination suffers from out-of-focus fluorescence, which reduces the SNR and decreases the localization precision. Illumination schemes like TIRF or HILO [22,23,60] are highly selective and yield good SNRs, but they are restricted to excitation volumes close to the glass-sample interface. Single-molecule LSFM allows optical sectioning deep inside biological tissue and the use of high NA water-immersion objective lenses, both beneficial for optimal signals. Biological, fluorescent molecules as small as a few nanometers were accessible to single molecule observation in aqueous solution, and we succeeded to track molecules with a diffusion coefficient of greater than 100 µm²/s. The LSFM is therefore an excellent tool to perform single molecule studies in living tissue. Moreover, the method has great potential for super resolution imaging and 3D tracking of single molecules in large, living specimens such as embryos at a millisecond time scale.

3.5 Materials and Methods

3.5.1 Optical setup

We used an Axiovert 200 (Carl Zeiss MicroImaging GmbH, Göttingen, Germany) and replaced the microscope stage with a custom-built stage, which allowed illumination perpendicular to the detection axis. The lateral position of the specimen chamber was adjusted by micrometer screws (BM11.16, Newport, Darmstadt, Germany), and axially by a motorized stage (M105.1B translation stage with DC-Mike linear actuator M232-17 from PI, Karlsruhe, Germany). The specimen chamber was made of BK7 glass and was especially manufactured for our purposes (Hellma, Müllheim, Germany). The internal dimensions of the chamber were 4 mm x 20 mm x 2 mm. The wall thickness was 2.5 mm and the bottom had standard cover slip thickness, 0.17 mm.

For fluorescence excitation three laser lines were used: A 488 nm DPSS laser (Sapphire-100, Coherent, Germany), a 532 nm solid state laser (LaNova50 Green, Lasos, Germany) and a 638 nm laser diode module (Cube635-25C, Coherent, Germany). All three laser lines were guided with dichroic beam splitters to an acousto-optical tunable filter (AOTF.nC 1001, Opto-Electronics, France). The AOTF selected laser lines, and defined illumination durations and intensity. After the AOTF the light was coupled into a mono-mode fiber (kineFlex, Point Source, Hamble, UK) and guided onto the optical table. Here the elliptical Gaussian illumination beam was formed by a cylindrical Galilean beam expander. It consisted of a convex cylindrical lens with a focal length of f = 250 mm and a concave lens with a focal length of f = -38.1 mm (CKX540-C and CKV522-C, Newport, Darmstadt, Germany). As illumination objective we used a plan apochromat 10x, NA 0.28 long working distance objective lens (Mitutoyo, Japan).

Fluorescence signals were collected with a 40x, NA 1.2 water immersion objective lens (C-Apochromat, Carl Zeiss MicroImaging GmbH, Göttingen, Germany), or a 10x, NA 0.3 objective lens (EC Plan-Neofluar, Zeiss). In the emission beam path respective narrow bandwidth notch filters were employed (Semrock, Rochester, USA). For imaging an EMCCD camera with 128x128 pixels was used (iXon BI DV-860, pixel size 24 µm, Andor Technologies, Belfast, Ireland). A 4x magnifier (Carl Zeiss MicroImaging GmbH, Göttingen, Germany) was added in front of the camera, which resulted in an objective field pixel size of 150 nm for the 40x, NA 1.2 objective lens. The dimensions of the light sheet were measured with a slow-scan CCD camera (Axiocam MRm, Carl Zeiss MicroImaging GmbH, Göttingen, Germany) with a pixel size of 645 nm for the 10x, NA 0.3 objective lens.

3.5.2 Determination of light sheet thickness

ATTO647N (ATTO-TEC GmbH, Siegen, Germany) was diluted in buffer at a concentration of 100 µM and filled into the specimen chamber. Upon laser excitation a homogenous image of the light sheet was created (**Figure 3.2**). In standard configuration the extension in the y-direction of the light sheet was imaged. Rotating the cylindrical lenses by 90° rotated the elliptical illumination beam, and therefore the z-width of the light sheet could be imaged. Images were taken for all excitation laser lines. Excitation of the ATTO647N by 488 and 532 nm occurred due to a small absorption band in the blue-green range of the dye spectrum. The light sheet was imaged by a 10x NA 0.3 objective (EC Plan-Neofluar, Zeiss) and detected by an Axiocam MRm (Carl Zeiss MicroImaging GmbH, Göttingen, Germany). For both y- and z-directions the FWHM of every vertical pixel line in the image was plotted versus the position on the illumination axis, which allowed the determination of the light sheet waists (**Figure 3.2**).

3.5.3 Single molecule imaging and analysis

For imaging of single molecules in solution the molecules were diluted to a final concentration of 100 pM in transport buffer. Fluorescence signals were detected with a 40x, NA 1.2 water immersion objective lens at room temperature. All movies were recorded at a frame rate of 483.09 Hz corresponding to an exposure time of 2 ms per frame. Fluorescence was excited by the 638 nm laser line.

Before tracking a background subtraction and 3x3 Gaussian filtering was performed on the image stacks. Single molecule signals were identified by the threshold algorithm of the tracking software Diatrack v3.03 (Semasopht), which was also used for trajectory definition. To exclude occasionally occurring aggregates of ovalbumin or oligonucleotides from the analysis unusually bright signals and unusually slow moving particles were excluded from the analysis.

From the resulting trajectories the mean-square-displacement (MSD) was calculated and plotted versus time t. The data were fitted according to $\langle x^2 \rangle = 4Dt$ to determine the diffusion coefficient D. This was done with Origin 8.0 PRO (OriginLab Corporation, Northampton, USA).

To calculate the theoretical diffusion coefficient we used the Stokes-Einstein equation [74].

$$D = \frac{k_B T}{f} \tag{3.1}$$

Here D is the diffusion coefficient, k_B the Boltzmann constant, T the temperature and f the frictional drag coefficient. For a sphere with radius r such as the 500 kDa dextran and ovalbumin, f is defined as [74]:

$$f_{sphere} = 6\pi\eta r \tag{3.2}$$

For a randomly moving ellipsoid, such as the 30b oligonucleotide, it is defined as:

$$f_{ellipsoid} = \frac{6\pi\eta a}{\ln \frac{2a}{b}} \tag{3.3}$$

η is the viscosity of the medium, a and b the semi-major and -minor axes of a prolate ellipsoid of revolution. The according radii were obtained from the literature (500 kDa dextran [20,75] and oligonucleotide [66]) or calculated according to the equation [57] (ovalbumin):

$$r = \sqrt[3]{\frac{3M / N_A}{4\pi\rho}} \tag{3.4}$$

Here M is the molar mass, N_A the Avogadro constant and ρ refers to the protein density (1.2 g cm^{-3}) [76].

The contrast C of image sequences of 500 kDa dextran molecules was determined according to this definition.

$$C = \frac{I_{max} - I_{min}}{I_{max} + I_{min}} \tag{3.5}$$

I_{max} designates the intensity of a molecule in focus above background I_{min}. I_{max} was determined by fitting a 2D-Gaussian to the signals. I_{min} was determined by measuring the mean intensity in areas where no molecules were seen. All image sequences were recorded with an exposure time of 10 ms, which equates to frame rate of 98.91 Hz.

3.5.4 In vivo imaging and analysis

Imaging of the 500kDa dextran molecules and the labeled mRNP particles in salivary gland cell nuclei of *C. tentans* larvae were performed with a 40x, NA 1.2 water immersion objective lens at room temperature. Image integration time was 20 ms corresponding to a frame rate of 49.46 Hz. Fluorescence was excited by the 638 nm laser line.

All image stacks were analyzed with the tracking software Diatrack v3.03 (Semasopht). Background subtraction and Gaussian filtering was performed before signal identification. To localize the particle, every particle signal was fitted by a 2D Gaussian. Sequences of single, localized events were combined to trajectories.

The determination of the 2D-localization precision of moving BR mRNPs in the salivary gland cells was achieved using the equation [7],

$$\sigma = \sqrt{\frac{s^2}{N} + \frac{a^2}{12N} + \frac{8\pi s^4 b^2}{a^2 N^2}} \tag{3.6}$$

where s is the standard deviation of the point-spread function, a the pixel size, b the standard deviation of the background and N the total number of photons contributing to a signal. To determine the latter value the average number of the integrated intensity values for a signal was determined. Finally the total number of photons per signal was calculated considering the count-to-photoelectron conversion factor for the used iXon camera [77].

Out of the trajectories the jump distance from one frame to the next frame was calculated for every trajectory. These jump distances were plotted in a normalized histogram (**Figure 3.4d & e**) and fitted according to the following equation [56]:

$$p(r,\Delta t) = \sum_i \frac{A_i}{2D_i\Delta t} r \cdot \exp\left[-\frac{r^2}{4D_i\Delta t}\right] \tag{3.7}$$

This equation represents the theoretical jump distance probability density function for i diffusive species. A_i is the fractional amount of a single species and D_i the respective diffusion coefficient. r is the jump distance covered in the time interval Δt. In a complex medium like a cell nucleus a single, distinct diffusion coefficient was not expected and the equation above allowed a multi-component analysis of the *in vivo* data. The calculations and data fitting were performed by Origin 8.0 PRO (OriginLab Corporation).

We measured a reference diffusion coefficient in aqueous solution (1 cP) and also the diffusion coefficient in the nucleoplasm. For the calculation of the viscosity of the nucleoplasm we used Eq. 3.1.

3.5.5 Microinjection of C.tentans salivary glands

Chironomus tentans were raised as described [20]. Salivary glands were isolated from fourth instar larvae and microinjected with an Eppendorf injection and micromanipulation setup using a holding pressure of 25 hPa and manual injection procedure.

3.5.6 Buffer and reagents

Phosphate buffered saline (PBS) was prepared from a commercially available stock solution (Biochrom AG, Berlin, Germany). Transport buffer contained 20 mM HEPES/KOH, pH 7.3, 110 mM potassium acetate, 5 mM sodium acetate, 2 mM magnesium acetate, 1 mM EGTA, and 2 mM DTT. Amino-derivatized dextran (molecular mass 500 kDa; Invitrogen, Germany) was dissolved in 0.1 M $NaHCO_3$, pH 8, and fluorescence labeled with a 5-fold excess of ATTO647 succidinimidyl ester (ATTO-TEC GmbH, Siegen, Germany). Chicken egg Ovalbumin (molecular mass ~43 kDa; Sigma-Aldrich, Germany) was solved in PBS containing 1mM TCEP (tris(2-carboxyethyl)phosphine; Sigma-Aldrich, Germany) and labeled with ATTO647N maleimide (ATTO-TEC GmbH, Siegen, Germany). Preparation of ATTO647N-labeled hrp36 was according to [20]. All labeling reactions were set up at room temperature for 2 hours and free dye was removed by gel filtration on a BioRad-P6 desalting column (MW cut off 6 kDa; BioRad, Munich, Germany). Labeled probes were finally size-fractionated on a Superose 12 column to remove aggregates and smaller fragments. The 2'-O-methyl RNA oligonucleotide homologue to the repetitive portion of the BR 2.1 mRNA was obtained from IBA BioTAGnologies (Göttingen, Germany). It comprised 30 bases (ACT TGG CTT GCT GTG TTT GCT TGG TTT GCT) and contained a 5' fluorescence label (ATTO647N). To check for purity the oligo was resolved on a 15% polyacrylamide gel prior to use.

3.5.7 Fluorescence correlation spectroscopy

FCS measurements were performed using a Zeiss Confocor I microscope setup. For calibration of the beam width ATTO647N-maleimide dye molecules (MW 870 Da; ATTO-TEC GmbH, Siegen, Germany) in buffer were used. The diffusion coefficient of ATTO655-maleimide dye (MW 810 Da) has been measured previously with high precision [78], and a diffusion coefficient of 400 µm²/s was determined. Since both dyes were comparable in molecular weight, we assumed a diffusion coefficient of 400 µm²/s for ATTO647N-maleimide as well. This assumption was corroborated by the characteristic diffusion times for the two dyes of 63 and 62 µs, respectively. Calibration of the beam width was done prior to the measurements. Before a single FCS run, a z-scan was recorded to ensure that the measurement was performed in the solution not close to the coverslip. Data analysis was performed using FCS ACCESS (Evotec, Hamburg, Germany). The theoretical autocorrelation curve for 3D diffusion of up to 3 mobility components is,

$$G(t) = 1 + \left(1 + \frac{T}{1-T} e^{-t/\tau_t}\right) \sum_{j=1}^{3} \frac{f_j}{N} \frac{1}{1 + t/\tau_{D,j}} \frac{1}{\sqrt{1 + t/\tau_{D,j}\kappa^2}} \tag{3.8}$$

where f_j are the fractions corresponding to the different diffusion times $\tau_{D,j}$, N is the total number of fluorescent molecules, T is the ratio of triplet state, τ_t is the triplet time and κ is the axial $1/e^2$-beam radius of the laser beam divided by the lateral $1/e^2$-beam radius. κ was usually close to 5. τ_D is related to the diffusion coefficient by

$$D = \frac{w^2}{4\tau_D} \tag{3.9}$$

where w is the lateral $1/e^2$-beam radius of the laser spot. Laser illumination was performed with 633 nm light.

ATTO647-labeled 500 kDa dextran molecules were diluted 1:1000 from the stock in PBS, followed by centrifugation at 22000 x g for 45 minutes. Before measuring, a MatTek dish (MatTek Corp., Ashland, USA) was coated with bovine serum albumin (10g/L). After removing the coating solution, 300 µL dextran solution was added and covered with a coverslip to prevent evaporation. Single FCS runs with 10 to 30 seconds were performed and average values were calculated. ATTO647N-labeled ovalbumin was diluted in transport buffer 1:1000 from stock solution, and centrifuged at 22000 x g for 30 minutes. Single FCS runs of 60 seconds length were performed and average values were calculated. ATTO647N-labeled Oligonucleotides were diluted 1:105 from stock concentration (1 nmol/µL) with PBS, and measured as described for ovalbumin.

Acknowledgments

Constructive discussions with Dr. Heinrich Spiecker and Volker Andresen from LaVision BioTec (Bielefeld, Germany) are gratefully acknowledged.

Author contributions

J.R. created the instrument concept; J.R. and A.V. developed the optical design; J.R., J.P.S. and U.K. designed experiments; J.R., J.P.S. and R.V. performed and analyzed experiments; J.R. and U.K. wrote the manuscript.

3.6 Supporting Information

3.6.1 SI Discussion:

In the case of the oligonucleotides distinct deviations from the linear behavior were observed for times greater than 6 ms (**Figure 3.3**). This behavior was due to the limited size of the observation field. The camera field of view was only 19.2 x 19.2 µm in size, and therefore longer single molecule trajectories were only observable in cases when the respective molecules were confined in this area (1) [57].

3.6.2 SI Figures

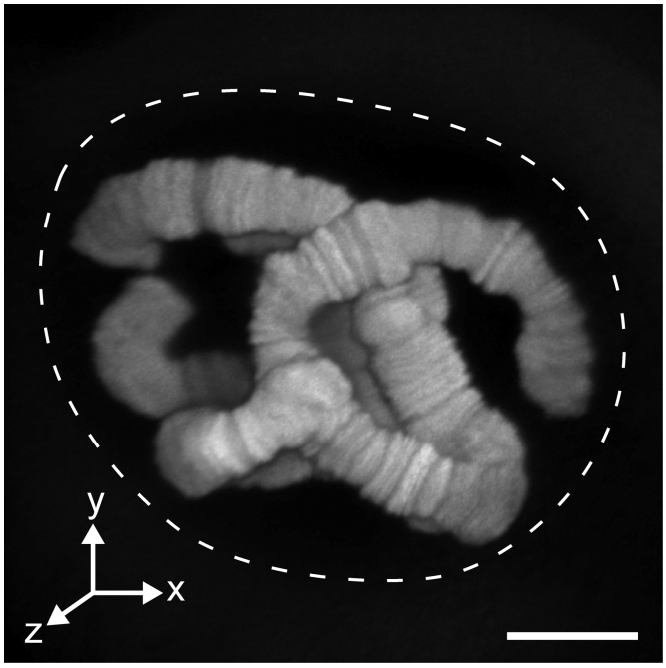

SI Figure 3.5 3D-reconstruction of the polytene chromosomes and their distribution inside the nucleus of the salivary gland cells of the C.tentans larvae. Inside the nucleus the entire DNA is located in the polytene chromosomes, leaving the nucleoplasm chromatin free. Dashed line indicates the border of the nucleus. Images were taken with a confocal microscope. Scale bar, 15 µm.

SI Figure 3.5 Material & Methods

For staining of the polytene chromosomes with propidium iodide the larvae the fixation of the glands was carried out in -20°C cold methanol for 10 minutes, followed by permeabilization with TritonX100 (Carl Roth, Karlsruhe, Germany) for 10 minutes at room temperature. After rinsing with PBS three times, the sample was incubated with propidium iodide (1µg/mL) (Sigma-Aldrich, Germany) for 30 minutes at room temperature. Again the sample was rinsed three times with PBS for 10, 10 and 60 minutes at room temperature. Finally the stained glands were sealed with Vectashield (Vector Laboratories, Burlingame, USA) and an LSM 510 Meta and a NA 1.4 oil immersion objective (Zeiss, Göttingen, Germany) was used for imaging. 3D reconstruction was done with the freely available BioimageXD (www.bioimagexd.net).

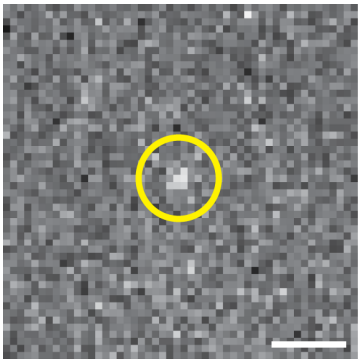

SI Figure 3.6 hrp36 labeled BR mRNP imaged upon epi-illumination. ATTO647N-labelled hrp36 proteins were microinjected into the nucleus of a salivary gland cell. After 10 min the hrp36 proteins were incorporated within mRNPs. The yellow circle indicates the position of the mRNP. Exposure time 20 ms; scale bar 1.5µm.

3.6.3 SI Movies

SI Movie 1[64]

On the left panel, freely diffusing 500 kDa dextranes diluted in PBS were imaged with epi-illumination at room temperature. On the right panel the same sample was imaged with LSFM. Both movies were recorded with 98.91 Hz and displayed with 30 Hz. For both movies the same camera and laser power settings were used. Field of view is 19.2 µm×19.2 µm.

SI Movie 2[64]

Three different species of freely diffusing single molecules in buffer were imaged with 483.09 Hz and displayed with 30 Hz. On the left panel 500 kDa dextran molecules with an diffusion coefficient of $D_{dextran}$ = 8.2 µm²/s are shown, in the center panel 43 kDa ovalbumin molecules with D_{Ova} = 88 µm²/s and on the right panel 30mer oligonucleotides with a D_{30mer} = 130 µm²/s. The movies were filtered with a 3×3 Gauss kernel and contrast enhanced. Field of view for each panel is 19.2 µm×19.2 µm.

SI Movie 3[64]

Hrp36 was microinjected in the nucleus of a salivary gland cell of a C.tentans larva. After 10 min hrp36 proteins were incorporated into mRNPs and became visible at the employed imaging rate of 49.46 Hz. The movie is displayed with 30 Hz. Field of view is 19.2 µm×19.2 µm.

SI Movie 4[64]

The 500 kDa dextran was microinjected in the nucleus of a salivary gland cell of a C.tentans larva and immediately imaged at a frame rate was 49.46 Hz. The movie is displayed with 30 Hz; field of view, 19.2 µm×19.2 µm.

4 A cylindrical zoom lens unit for adjustable optical sectioning in light sheet microscopy

Jörg G. Ritter, Jan-Hendrik Spille, Tim Kaminski and Ulrich Kubitscheck.
Biomed Opt Express 2: 185-93 [79]

4.1 Abstract

Light sheet microscopy became a powerful tool in life sciences. Often, however, the sheet geometry is fixed, whereas it would be advantageous to adjust the sheet geometry to specimens of different dimensions. Therefore we developed an afocal cylindrical zoom lens system comprising only 5 lenses and a total system length of less than 160 mm. Two movable optical elements were directly coupled, so that the zoom factor could be adjusted from 1x to 6.3x by a single motor. Using two different illumination objectives we achieved a light sheet thickness ranging from 2.4 µm to 36 µm corresponding to lateral fields of 54 µm to 12.3 mm, respectively. Polytene chromosomes of salivary gland cell nuclei of *C.tentans* larvae were imaged *in vivo* to demonstrate the advantages in image contrast by imaging with different light sheet dimensions.

4.2 Introduction

Light sheet microscopy is a versatile tool for imaging of intact fluorescent biological objects in three dimensions. The fundamental principle of light sheet microscopy is the illumination of the sample by a thin, focused light sheet perpendicular to the detection axis. In this manner only the focal plane of the detection objective is illuminated and no out-of-focus fluorescence compromises the signal quality. The optical sectioning effect results in an excellent contrast and low photo-toxicity [27,32].

The light sheet technique is applicable to various specimens ranging from single cells to complete insect and mouse embryos [26,29,37,59,64,80,81,82]. These specimens cover several orders of magnitude in diameter and require widely differing light sheet geometries for appropriate illumination. Usually light sheet microscopes are therefore highly specialized to observe a certain specimen type. In most cases a fixed light sheet geometry limits the observable sample size. A complete mouse embryo requires a light sheet configuration that is several orders of magnitude larger than that required for a single cell nucleus [58,83]. However, a large lateral field-of-view automatically produces a large axial extension of the sheet due to the laws of Gaussian beam optics [25]. Similarly, very thin light sheets yield optimal optical sectioning but have small usable field-of-views. It is important to carefully adjust both parameters to achieve optimal imaging quality in each experiment. The focused beam waist is inversely proportional to the radius of the incident illumination beam. Hence, for a continuous

and flexible adjustment of the focal waist an afocal cylindrical zoom beam expander can be used to modify the extension of the focus range. Neither power loss nor refractive distortions of the beam profile occur as it would happen by use of vertical and horizontal slit apertures for beam diameter definition [43].

Here we present a cylindrical zoom lens system for light sheet shaping, so that various specimens of different sizes can be observed using a single light sheet microscope. The system comprises only 5 commercially available cylindrical lenses and features a compact system length of 160 mm only. A zoom range from 1.0x to 6.3x magnification of the incident beam in one dimension is achieved. The system performance using different zoom factors was demonstrated by imaging fluorescently labeled nuclei and polytene chromosomes in salivary gland cells of *Chironomus tentans* larvae.

4.3 Results

4.3.1 Optical Setup

The light sheet microscopic setup is shown in **Figure 4.1**. Multiple laser lines (L1-L3 / λ_0 = 488 nm, 532 nm and 638 nm / Sapphire-100, Coherent, Germany, LaNova50 Green, Lasos, Germany and Cube635-25C, Coherent, Germany) were combined by appropriate dichroic mirrors and were guided through an acousto-optical-tunable-filter (AOTF, AOTF.nC 1001, Opto-Electronics, France). The AOTF controlled the transmitted intensity and selected the desired wavelength. Behind the AOTF the light was coupled into a mono-mode fiber (kineFlex, Point Source, Hamble, UK) and guided to the microscope. Deviations from the Gaussian TEM_{00}-mode were removed by a spatial filter, which consisted of two achromatic lenses (f = 30 mm) forming a 1:1 Keplerian telescope with a small pinhole (d = 25 µm) at the focal point.

The key component of the illumination beam path was the cylindrical zoom unit, which comprised five cylindrical lenses (C1-C5, see **Table 4.1**; from Thorlabs, USA). The three convex lenses were fixed, and the two concave lenses were movable (**Figure 4.2a & b**). The two concave lenses C2 and C4 were mounted on a micrometer stage and directly coupled. Thus the distance between the two lenses remained constant and the zoom factor Z could be modified by a single motor. A light sheet was generated inside a small water chamber by focusing the resulting elliptically shaped Gaussian beam with the illumination objective (10x Mitutoyo Plan Apochromat with NA 0.28) [58] or an achromatic lens (focal length 85 mm, Edmund Optics). Since the focused spot size was inversely proportional to the incoming beam diameter [25], the zoom unit regulated the light sheet thickness and length. The cylindrical lens C6 was arranged perpendicular to the zoom unit and affected only the width of the light sheet. The beam was focused into the back focal plane of the illumination objective, which therefore formed together with

lens C6 a Keplerian telescope resulting in a collimated width (along the y-axis) of the light sheet inside the water chamber (**Figure 4.2c**). A vertical slit (VS) was used to control the width of the light sheet from 20 µm to 120 µm full width at half maximum (FWHM).

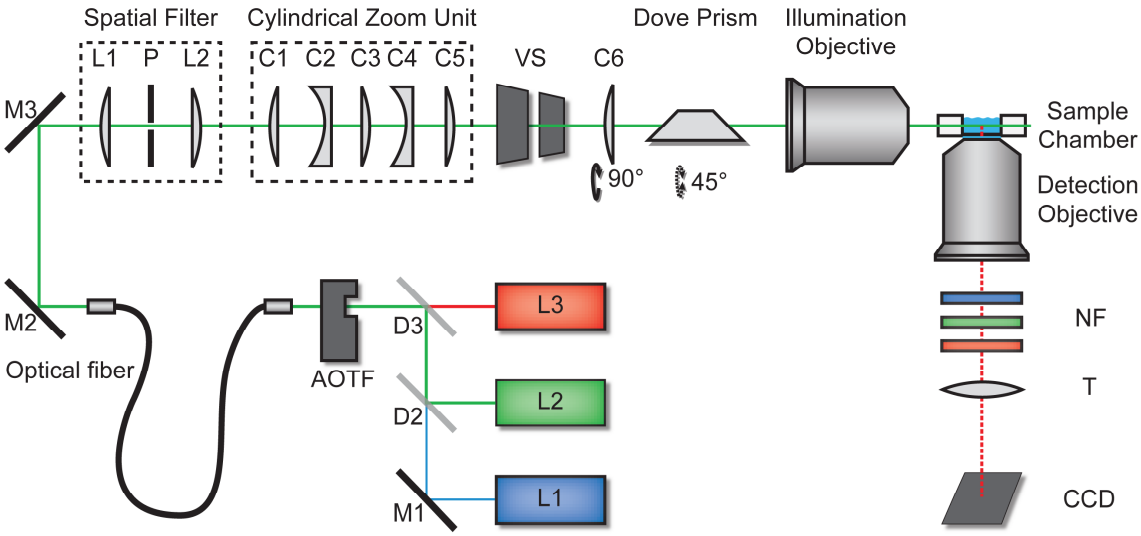

Figure 4.1 Light sheet microscope setup. Laser light (L1 - L3) was guided into the illumination beam path via dichroic beam splitters (D1 and D2), an optical fiber and mirrors. Laser wavelength and intensity was controlled by an acousto-optical-tunable-filter (AOTF). The two achromatic lenses L1 and L2 (f = 30 mm) and the pinhole P formed a spatial filter. The cylindrical zoom unit consisted of five lenses (C1 - C5). A further cylindrical lens (C6) oriented perpendicular to the zoom lens unit focused the beam into the back-focal-plane of the illumination objective, which focused the light sheet into the sample chamber. A vertical slit (VS) was used to control the width of the light sheet. The sample could be moved by a three-axis motorized sample scanner and the illumination objective was motorized along the optical axis. The detection unit comprised the detection objective, small bandwidth notch filters (NF), tube lens (T) and CCD-camera.

Fluorescence light emitted from the sample was collected by the detection objective lens and imaged onto a CCD camera (Clara, pixel size (6.45 µm)² or iXonDU897, pixel size (16 µm)², Andor Technologies, Belfast, Ireland). Excitation laser light was removed by Notch filters (NF, Semrock, Rochester, USA). Three motorized stages (M112-12s, PI, Karlsruhe, Germany) were used to adjust the sample chamber position in all three spatial dimensions, and a fourth stage was used for positioning the illumination objective along the optical axis. This was necessary because the air spacing between this objective and the water chamber changed when the sample chamber was moved in x-direction along the illumination axis. This caused a displacement of the focal position of the sheet of about 34 µm per 100 µm movement of the chamber that had to be corrected. Furthermore, the position of the focus shifted for the different zoom configurations due to spherical aberration introduced by focusing with an air objective through glass walls into a water chamber. For the complete zoom range the focus shift

was approximately 300 µm. This could also be corrected by an appropriate positioning of the illumination objective.

Table 4.1 Cylindrical lenses of the zoom unit

Lens [Thorlabs catalogue]		Focal length [mm]
C1	LJ1934L1	150
C2	LK1006L1	-22.2
C3	LJ1075L1	25
C4	LK1085L1	-20
C5	LJ1640L1	130
C6	LJ1934L1	150

The setup was realized using a commercial inverted microscope (Nikon TI-U, Düsseldorf, Germany). Installation of the sheet illumination in a commercial microscope stage increased usability of the setup, and allowed to readily exchange detection objectives or to use different contrast modes.

4.3.2 Zoom lens system

The light sheet thickness was inversely proportional to the incoming beam diameter at the illumination objective [25], which was defined by the variable afocal cylindrical beam expander (**Figure 4.2.**). The design of the zoomable beam expander was based on work by Winterot et al. 2005 [84]. The optical layout of the zoom unit with important parameters like focal lengths and lens-to-lens distances were developed by ray tracing simulations with OSLO Light Version 6.4 (Lambda Research Corporation, Littleton, MA, USA) using only commercially available lenses. Variation of the zoom factor was achieved by a joint motion of two linked concave lenses, which could be moved over a total range of 25 mm.
Table 4.2 shows exemplary distances between the various lenses for three different zoom positions. The installation length of the zoom lens unit was less than 160 mm, and the total zoom was designed to achieve a magnification range of 1x to 6.3x.

To verify the theoretical ray tracing results we imaged the beam after passing the zoom lens system for different stage positions of the movable lenses. For this purpose a CCD camera was placed behind lens C5. From the recorded images (**Figure 4.3a**) we determined the diameter of the beam along the elongated axis by fitting the intensity profiles with a Gaussian function (**Figure 4.3b**). The zoom factor Z was calculated by

comparing the results to the incoming beam diameter, which was determined by the same method. We repeated the measurements five times and calculated a mean zoom factor for the different stage positions (**Figure 4.3c**). The zoom factor ranged from Z = 1.00 ± 0.03 to Z = 6.3 ± 0.2. The measured curve was in excellent agreement with the ray tracing calculations.

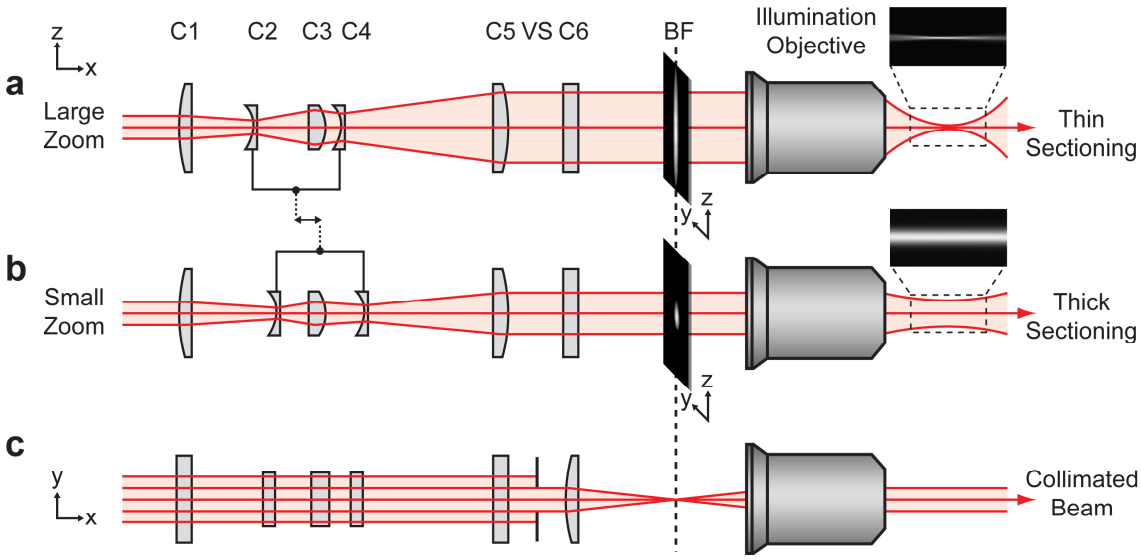

Figure 4.2 Cylindrical zoom beam expander. The configurations for a large zoom (**a**) and a small zoom (**b**) are shown. For a large zoom the beam diameter incident at the illumination objective is large in z-direction and hence the optical sectioning thickness is decreased compared to a small zoom. Lenses C2 and C4 are coupled and mounted together on a micrometer stage (not shown), so that a single motion readjusts the zoom factor. (**c**, top view) The incident beam diameter along y-direction is limited by a vertical slit aperture (VS), which defines the lateral width of the light sheet. The beam is focused into the back-focal-plane (BF) of the illumination objective by cylindrical lens C6. Exemplary images of the produced light sheets were shown on the right hand side (see **4.3.3**).

Table 4.2 Lens to lens distance for three different zoom factors

Distance [mm]	1x	3x	6x
C1 → C2	48.54	34.11	23.63
C2 → C3	10.73	25.16	35.64
C3 → C4	26.54	12.11	1.63
C4 → C5	58.56	72.99	83.47
C2 → C4	37.27	37.27	37.27

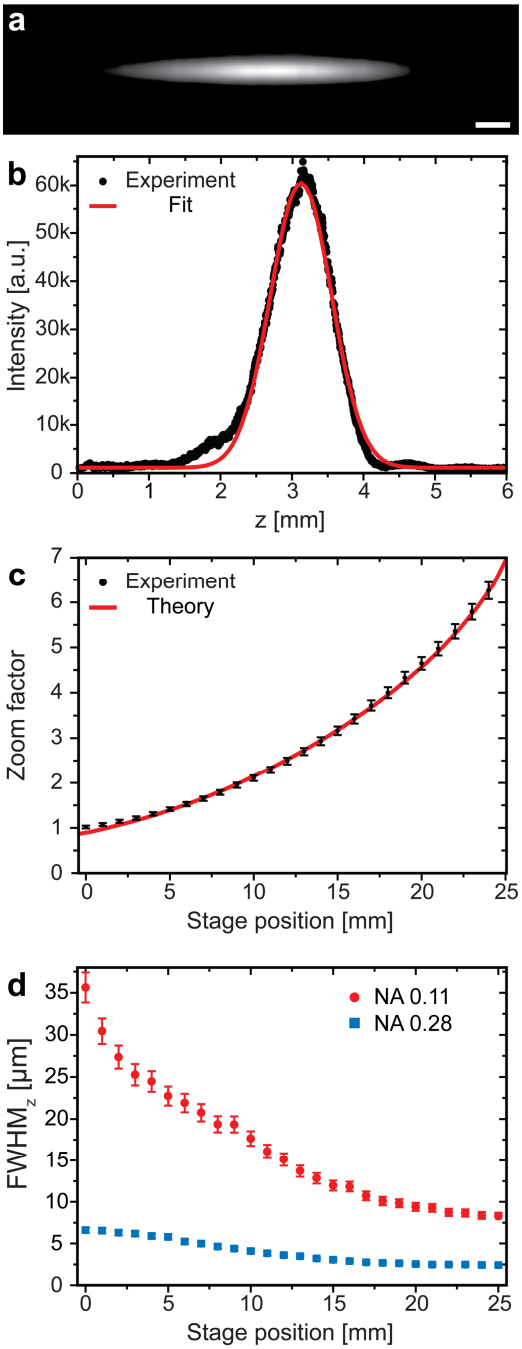

Figure 4.3 Measured zoom range of the cylindrical zoom lens and corresponding light sheet thickness. (**a**) Beam cross section behind the zoom unit Scale bar 100 µm. (**b**) Intensity profile along the central horizontal pixel line in the intensity profile shown in (a). The red line shows the Gaussian fit to the measured data. (**c**) The zoom factor was calculated for different stage positions of the movable zoom lenses by comparing output to input beam diameter. Standard deviation, 3% (error bars). The red line shows the expected result obtained by ray tracing calculations. (**d**) Measured optical sectioning thickness for an achromatic NA 0.28 (blue squares) and an NA 0.11 (full red dots) illumination objective lens. Standard deviation, 5 % (error bars).

4.3.3 Optical sectioning thickness

The actual light sheet dimensions could directly be visualized by illumination and imaging of a homogeneously fluorescent sample such as ATTO647N dye in buffer solution as shown in **Figure 4.2**. The lateral beam width could directly be obtained by imaging using a 10x objective lens. However, in order to determine the optical sectioning thickness the incident beam had to be rotated by 90°. This was conveniently achieved by placing a dove prism in front of the illumination objective. Rotating the prism by 45° resulted in a beam rotation of 90°. From images recorded in this configuration we deduced the axial extension of the light sheet by fitting a Gaussian function to the intensity values along each pixel line perpendicular to the optical axis. The minimal extension corresponded to the optical sectioning thickness [58].Five images were recorded for each stage position and the mean FWHM and its standard deviation were calculated. For the NA 0.28 illumination objective the FWHM of the optical sectioning range was found to be $\Delta z_{FWHM} = 2.4 \pm 0.1$ µm ($Z = 6.3$) to $\Delta z_{FWHM} = 6.6 \pm 0.3$ µm (Z=1.0) for an excitation wavelength of $\lambda_0 = 638$ nm (**Figure 4.3d**). This corresponded to a lateral depth of focus of 54 µm to 410 µm. Generally, the optical sectioning thickness is dependent on the NA of the illumination optics. Therefore the optical sectioning thickness and the observable field of view can further be extended by altering the different illumination optics. With an illumination objective lens of 0.11 NA (focal length, 85 mm) the optical sectioning range was determined as $\Delta z_{FWHM} = 8.3 \pm 0.4$ µm ($Z = 6.3$) to $\Delta z_{FWHM} = 36 \pm 2$ µm (Z=1.0) for an excitation wavelength of $\lambda_0 = 638$ nm (**Figure 4.3d**). The corresponding lateral depth of focus ranged from 650 µm to 12.3 mm.

4.3.4 Live imaging with different zoom configurations

To demonstrate the effect of the zoom unit in live biological specimen we imaged salivary gland cell nuclei of *Chironomus tentans* larvae. Salivary gland cells contain large nuclei with diameters of about 60 µm located up to 300 µm deep inside the salivary glands. Each gland cell nucleus contains four polytene chromosomes with a diameter of about 10 µm. Each chromosome comprises 8000 to 16000 perfectly aligned chromatids, which form a characteristic chromosome band structure [69]. To visualize this band structure we microinjected ATTO647N-labelled hrp36 into the nuclei of living gland cells. Hrp36 was bound to nascent mRNA [72] during mRNP formation, and therefore labeled active transcription sites. Use of a small zoom factor Z = 1.0 providing a large field-of-view and large optical sectioning thickness allowed a rapid localization of labeled polytene chromosomes. The light sheet extension along the y-axis was set to the maximum value of FWHM 120 µm (**Figure 4.4a & c**). After locating the chromosomes we increased the zoom factor to Z = 6.3, what improved axial resolution

and image contrast (**Figure 4.4c & d**). The typical band structure of a polytene chromosome and a Balbiani Ring transcription site were well resolvable. The illumination shadows often encountered in light sheet microscopic images [38] were removed by a wavelet filter [85].

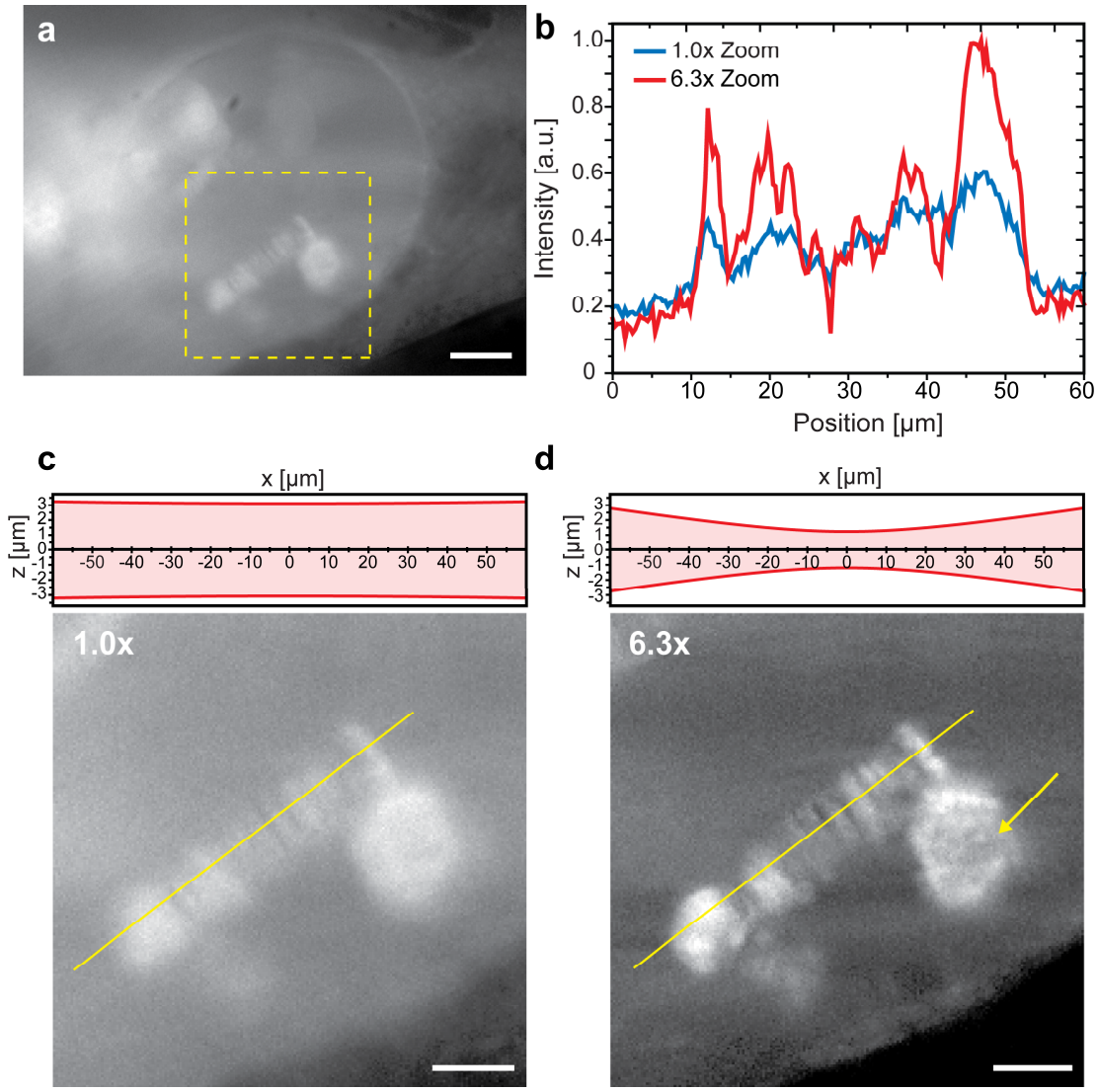

Figure 4.4 Live imaging with different zoom configurations. Polytene chromosomes of *C. tentans* larvae salivary gland cell nuclei imaged at different zoom factors. (**a**) Overview image at zoom 1.0x of the complete nucleus to locate the fluorescently labeled polytene chromosomes. Scale bar, 20 µm. (**b**) Intensity plots along the yellow lines in (c) and (d) demonstrated the improved contrast for a higher zoom factor yielding a smaller optical sectioning thickness. (**c**) and (**d**) Magnified views of the marked region in (a) at different zoom factors. The FWHM optical sectioning thickness along z was indicated above the images. The field-of-view in (d) was limited in comparison to (a) and (c), but the image contrast was increased revealing structures, which were hidden before. The typical band structures of the polytene chromosomes as well as the Balbiani Ring transcription site (yellow arrow) became well discernible. Scale bar 10 µm. Images were taken with 20x, 0.5 NA Nikon CFI Planfluor and imaged by a iXon EMCCD-camera with a 2.5x magnifier resulting in an effective pixel size of 320 nm.

4.4 Discussion

Light sheet microscopy has been shown to be advantageous for the imaging of various specimens ranging from single cell nuclei to complete fixed or living animal embryos. Such specimens differ significantly in size and therefore require greatly differing light sheet geometries for illumination. In this paper we introduced a variable light sheet concept comprising a cylindrical illumination zoom lens system and different illumination objective lenses. This concept provides the necessary flexibility to the illumination geometry of a light sheet microscope, because it allows the observation of biological samples with different sizes using a single instrument. It has several advantages over alternative beam shaping methods.

An alternative method for beam shaping of light sheets is to utilize slit apertures. By using rectangular slit apertures in the beam path [3,43,86] a significant amount of the illumination power is lost. Also, diffraction effects distort the excitation beam resulting in an uneven illumination profile and a reduced optical sectioning thickness. Diffractive effects are negligible for focal waists with FWHM values > 10 µm as it is the case in our setup for the light sheet width in y-direction.

A quite different approach to light sheet generation is digital scanned laser light-sheet fluorescence microscopy (DSLM) [41]. Here, a laser beam is focused to a single line and rapidly scanned up and down during image acquisition thus generating a virtual light sheet. The advantages of this technique are the uniform illumination intensity over the complete field-of-view and a simple adjustment of the light sheet width through computer controlled scanning mirrors. But in DSLM only the light sheet width is scanned and can be adjusted, but the optical sectioning thickness stays constant. This technique is especially suited to observe large specimen and can also be used for structured illumination for contrast enhancement [29], but the scan speed is to slow for applications like single molecule tracking, which require very high imaging rates [9,58].

We could already adapt our setup to a large variety of specimen due to a light sheet thickness ranging from 2.4 µm to 6.6 µm. The corresponding optimal field-of-view ranged from 54 µm to 410 µm. Axial and lateral illumination widths could be further extended by using illumination objective lenses with lower numerical apertures. We demonstrated this by replacing the 0.28 NA illumination objective by an 0.11 NA objective lens achieving light sheet thicknesses from 8.3 µm to 36 µm with a corresponding field-of-view of 650 µm to 12.3 mm. Since the used illumination objective lenses were designed to operate in air, the glass and water interface introduced a certain amount of spherical aberration. Thus it was not possible to translate the six-fold increase in beam diameter achievable in the zoom lens system into a corresponding reduction of the light sheet thickness. To take advantage of the full zoom range, either a

very low NA objective, for which the spherical aberrations would be even less significant, or an especially corrected objective, which considers the unique illumination geometry, must be used [47]. In our current setup the width of the light sheet (y-direction) was adjustable in the range of 20 – 120 µm, which could easily be extended by lateral scanning or by choosing a focusing lens (C6) with a greater focal length, which would have to be traded against a greater system length for the illumination optics. Generally, reduction of the illumination field diminishes unwanted photon exposure and reduces light scattering.

Despite the encountered limitation we found the zoom lens concept to greatly expand the versatility of light sheet microscopes.

Acknowledgments

This project was funded by grant of the German Research Foundation to U.K. (Ku 2474/7-1) and by the German Ministry for Economics and Technology (ZIM KF2297601AK9). Thanks to Eugen Baumgart for the shadow reduction in the images. Constructive discussions with Dr. Heinrich Spiecker and Volker Andresen from LaVision BioTec (Bielefeld, Germany) are gratefully acknowledged.

Author contributions

Conceived and designed the experiments: JGR, JHS, UK. Performed the experiments: JGR, JHS, TK. Analyzed the data: JGR. Wrote the paper: JGR and UK. Created the instrument concept: JGR. Developed the optical design: JGR.

5 Summary and Conclusion

5.1 Summary: High-contrast single particle tracking by SPIM

The work in this thesis demonstrated that light sheet based fluorescence microscopy (LSFM) and single molecule tracking are an ideal combination. LSFM provides an optical sectioning effect and the resulting enhancement of the signal-to-noise-ratio combined with the high acquisition speed of video microscopy are both key features for successful single molecule visualization and tracking. In the first experimental setup described in detail in Chapter 2 [47] the technical requirements to realize this aim had to be explored. The setup used for this purpose was similar to the SPIM setup described by Huisken et al. 2004 (Chapter 1.5) [35]. Although his setup was successful in multi-view reconstruction of medaka embryos it had not been used to image single molecules. For this, it lacked the necessary optical sectioning thickness (reported 6 µm) and detection objective numerical aperture (reported NA 0.3). Huisken et al. (2004) [35] used a cylindrical lens to focus the beam inside a water chamber, thus generating a 6µm thick light sheet in the focal plane of the detection objective. The achievable light sheet thickness was limited by the resolving power of the cylindrical lens and by the spherical aberration introduced by two refractive index changes: first at the air-glass interface and second at the glass-medium interface.

To capture the intrinsically weak single molecule signals, especially the illumination and detection optics had to be redesigned. A high detection NA was required for maximal photon collection efficiency. Moreover, to enhance the signal-to-noise-ratio, the background fluorescence had to be reduced to a minimum which required a light sheet as thin as possible. Therefore a new illumination concept had to be developed. The laser light was expanded by a cylindrical lens telescope and subsequently focused by an specifically designed illumination objective [51,87]. The custom-made illumination objective took the specific sample chamber geometry into account and minimized the aberration introduced by the air-glass and glass-water interface. Furthermore it featured a long working distance, so that illumination and detection objective could be mounted perpendicular to each other without spatial obstructions. With this newly developed illumination beam path an optical sectioning thickness of full-width-at-half-maximum 1.7 µm (FWHM) was achieved. Further optimizations of the setup included a change of the detection objective and imaging camera. Since the setup is designed to use water-dipping objectives for detection, the maximal available NA is limited to 1.0 and was chosen for optimal photon collection efficiency in this setup. To realize a high acquisition speed an electron-multiplying CCD (EMCCD) camera employed for imaging.

To predict the light sheet dimensions and resolution of the microscope an analytical description was required. To describe the light sheet dimensions the ABCD-law for Gaussian beams was applied to the illumination geometry and cross-checked by ray tracing calculations. These theoretical estimates were verified by experimental measurements with the knife edge method. For an analytical description of the lateral and axial resolution of the microscope the general point-spread-function (PSF) for light sheet microscopes was derived. The derived theoretical expression was tested by measuring the lateral and axial resolution by imaging sub-resolution microspheres. The results were in excellent agreement with the theoretical estimates and showed an improvement in axial resolution of 50% compared to previously presented results [31,50].

A LSFM key feature is the improved image contrast compared to conventional epi-illumination. To characterize this improvement the image contrast of fluorescent microspheres was measured with both illumination techniques with increasing fluorescent background. It was shown that, as expected, LSFM performs always better than standard epi-illumination in terms of contrast. It was still possible to discriminate single microspheres with LSFM, where under epi-illumination the signals vanished in the out-of-focus fluorescence.

Finally, the suitability of this setup for single particle tracking was demonstrated by visualizing the diffusion of fluorescent quantum dots in aqueous solution. From the recorded movies the diffusion coefficients of the single quantum dots were determined, and corresponded to previously reported results [57]. However, the developed instrument did not yet meet the experimental requirements for a versatile light sheet microscope, which is capable to visualize single molecules deep inside a living biological specimen.

First of all it was not sensitive enough to detect single fluorophores due to a relatively low detection NA. It was capable to image single particles, such as microspheres carrying multiple fluorophores or bright, semiconductor quantum dots. Unfortunately, for water dipping objectives the maximal possible NA was already implemented. Therefore a complete new reconstruction of the microscope and sample mounting was required to take advantage of high NA immersion objectives for optimal photon collection efficiency η_{Ph}, since η_{Ph} is proportional to NA².

$$\eta_{Ph\,Objective} \approx T_{\lambda} NA^2 \tag{5.1}$$

Here, T_{λ} is the transmittance of the objective at the wavelength λ. In the experiment design the sample was embedded in a gel like agarose mounted from above inside a medium filled chamber. Although this sample mounting technique had its benefits such

as biocompatibility through the lack of hard surfaces and the potential three dimensional development of the specimen as well as the possibility to rotate the sample for multi-view reconstruction, it was not practical for single molecule studies. Furthermore, on account of this specialized mounting procedure standard established laboratory protocols and techniques for sample preparation could not easily transferred or were rendered completely useless.

A simple reason why this strategy was unsuited for single molecule studies was that the volume of the medium filled chamber was too large. To reach detectable concentrations of single molecules in this chamber the volume had to be restricted in a complicated manner (**Figure 5.1**) as it had been done for instance in the quantum dot experiments. Alternatively large and expensive amounts of the precious sample had to be diluted in the chamber. More importantly, biological specimens mounted inside the chamber and embedded in the gel were hardly accessible for outside micromanipulation, for example by microinjection. Microinjection of fluorescently labeled marker proteins is a common technique to deliver marker molecules to their desired designation inside the living specimen, without interfering with the biochemistry of the specimen. Hence, modifications in the sample mounting were required to allow an easy measurement of single molecules in solution and leave the sample accessible for micromanipulation.

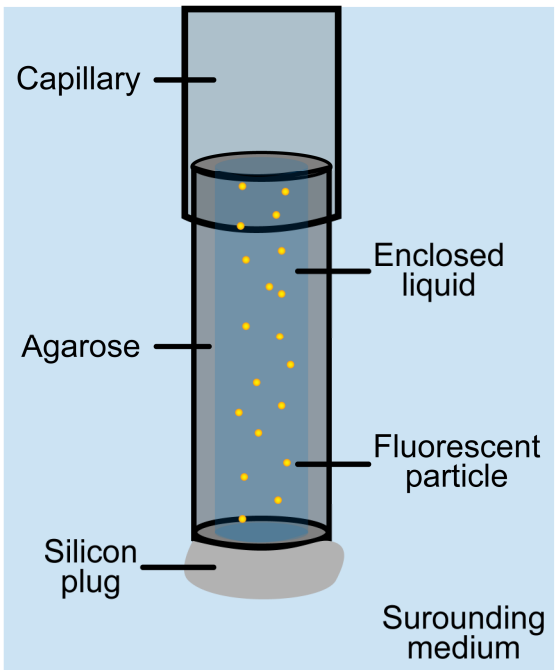

Figure 5.1 Mounting of a liquid sample in the first experimental setup. The liquid with the fluorescent particles was placed inside a hollow agarose cylinder. To contain the liquid and avoid a dilution with the surrounding medium a silicon plug seals the cylinder.

Finally. overview images are often required for orientation and sample positioning, since single molecule signals do not reveal structures that can guide the experimentator to the right spot in the sample. But this requires a brightfield illumination, which was not implemented in this setup. Additionally, due to the large magnification the high NA objective, the field-of-view was very small. To achieve larger field-of-views, optionally for overview or recording images, the detection objective should be exchangeable. This was not possible during an ongoing experiment since a water-dipping objective was used. The perfect solution would be an objective revolver for fast switching of the detection objective as it is common in commercial microscopes. Again, this demanded a complete reconstruction of the microscope and sample mounting.

5.2 Summary: Light sheet microscopy for single molecule tracking in living tissue

The next generation of the light sheet based fluorescence microscope (LSFM) addressed the challenges, which emerged during the experiments with the first microscope. Four major goals were set for the experimental realization: (1) Utilization of high numerical aperture objectives (NA > 1.0) to maximize the light detection efficiency and reach single fluorophore sensitivity. This required a complete reconstruction of the sample mounting and holder, since high NA objectives are designed to observe through a 0.17 mm thick cover slip. (2) Increased usability by constructing the sample holder on a commercial inverted microscope. (3) Multi-color illumination. (4) Application of the light sheet microscope to single molecule tracking in living biological tissue.

To achieve these goals a new experimental setup was required. A miniaturized sample chamber was constructed, which was completely made out of glass so that the illumination light could be introduced from the side. Additionally, it featured a cover slip thick glass bottom (0.17 mm). The sample chamber was mounted on a motorized stage and installed on an inverted microscope. This new design solved several problems of the first setup and lead to a significant increase in usability. High NA objectives (NA > 1.0) could be used, since all commercially available objectives require a cover slip in their beam path. The new sample chamber was basically a small cover slip with walls, so that the complex sample mounting procedure with embedding the sample in a gel and all involved problems vanished. Instabilities of the gel, like swelling or dropping out of the holder were non existent. The chamber was open on top and hence accessible for microinjection. Standard established lab protocols could be used without any further modifications. The volume of the chamber was only 160 µl, so that no large amounts of precious sample were required, but it was still large enough so that biological organisms could be placed inside. Since no water-dipping objectives were used, the objective could be easily changed without disturbing a measurement. By constructing it on an inverted microscope the objective revolver for fast objective changes and brightfield

illumination for overview images were automatically included. By these means a switching between light sheet illumination and standard microscopy techniques like phase or differential interference contrast (DIC) was possible as well.

The custom made illumination objective had to be replaced for two reasons. First, it was optimized for the illumination geometry of the first setup, which now was significantly changed. Second, two color experiments were not possible, because the objective was not color-corrected and introduced a chromatic focal shift of several hundred micrometers, which is two to three times larger than the depth-of-focus along the z-axis. A special objective from the company Mitutoyo met all construction conditions like a sufficiently large NA (NA 0.28), long working distance (33.5 mm) and color correction.

With this new experimental setup a new method to characterize the light sheet dimensions was needed, since knife edge tests in such a small chamber were laborious. The solution was to fill a fluorescent dye solution into the sample chamber and visualize the light sheet dimension upon illumination directly. By turning the cylindrical lenses of the illumination beam path by 90° and thus rotating the elliptical Gaussian beam it was straightforward to visualize and measure the light sheet thickness of FWHM 3 µm.

To demonstrate the sensitivity and acquisition speed of the instrument the mobility of single molecules in aqueous solution was investigated. A quantitative comparison of the image contrast in recordings of diffusing single fluorescently labeled dextrane molecules between LSFM and conventional epi-illumination demonstrated the superior imaging capabilities of LSFM. Due to the lack of out-of-focus fluorescence it was possible to image and track smaller (and faster) molecules than ever before with a diffusion coefficient up to 130 µm²/s. Three different species of single molecules with various sizes and shapes were analyzed: 500 kDa dextrane molecules, 43 kDa ovalbumin protein and 30b long oligonucleotides, covering two orders of magnitude in diffusion coefficients. The diffusion coefficients obtained by single molecule tracking were validated by fluorescence correlation spectroscopy (FCS) measurements. All results were in excellent agreement to theoretical predicted diffusion coefficients.

In the final step LSFM was employed for *in vivo* imaging within a three dimensionally extended biological specimen. The intranuclear movement of fluorescently labeled native mRNA particles in the nucleoplasm of the salivary gland cells of the *C.tentans* larvae could be studied. In this large biological system single mRNA particles marked with only one fluorescent dye were visualized and tracked 100 – 200 µm deep inside the gland cells. In a conventional fluorescence microscope single molecule imaging at such a depth within the specimen would be extremely difficult and would require exceedingly low probe concentrations, because the signal-to-noise-ratio is low due to a

high fluorescence background. To compare the mRNA particle mobility with inert molecules of similar geometrical size fluorescent dextrane molecules were microinjected in salivary gland cell nuclei as well. The diffusion coefficients from mRNA particles and dextrane molecules were analyzed and several mobile fractions could be identified. By comparison with the data from the previous single molecule measurements in buffer the effective intranuclear viscosity was determined.

Single molecule sensitivity was achieved and the principle of LSFM was successfully applied for visualizing the mobility of single molecules and particles deep inside living tissue with unprecedented signal-to-noise-ratio in this second setup. However, the instrument was a specialized solution optimized for the imaging in the salivary gland cells of the *C.tentans* larvae. The light sheet dimensions were fixed and therefore the usable field-of-view was constant. But different biological samples demand different optical sectioning thicknesses and field-of-views. The optical requirements for imaging cultured cells (diameter 15 µm) or larger tissue like salivary glands (diameter 500 µm) differ a lot. To image the specimen completely, in the first case the light sheet extensions have to be orders of magnitude smaller compared to the latter case. Hence, it is essential to adjust the light sheet dimensions in an easy and flexible way.

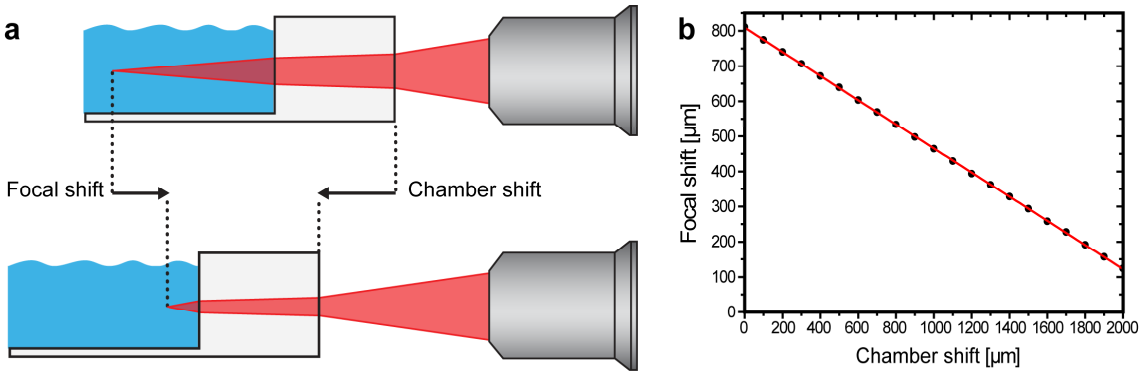

Figure 5.2 Focal position displacement during chamber movement. (**a**) The focal position was shifted when the chamber was moved along the illumination axis, because the light had to pass through different thicknesses of the air and water volume. In the light beam are different refractive angles at the refractive surfaces indicated. (**b**) The focus position was measured versus the chamber shift and fitted linearly. The slope was determined to -0.34. This means, when the sample was moved 100 micrometers along to the optical axis away from the illumination objective, this resulted in a focal shift of only 34 µm to the illumination axis as indicated in (a).

Another problem was introduced by the new sample chamber. The setup suffered from a focal shift of the light sheet, while the sample chamber was moved along the illumination axis (**Figure 5.2**). This is a critical problem, since the sample had to be moved to the desired location for the experiment and the illumination and detection optics had to remain unchanged. Both optics were fixed in their position once the focal

overlap was adjusted (Chapter 1.4). The problem arouse, because the illumination light had to pass several interfaces (air-glass and glass- water) after it passed through the illumination objective. By moving the sample along the illumination axis the thicknesses of the air and water regions were changed, which caused a displacement of the focus position (**Figure 5.2**). For example, when the sample was moved 100 micrometers along to the optical axis, this resulted in a focal shift of 34 µm (**Figure 5.2b**), which is in the range of the depth-of-focus for a 2-3 µm thick light sheet.

5.3 Summary: A cylindrical zoom lens unit for adjustable optical sectioning in LSFM

The instrument discussed above demonstrated the experimental realization and successful application of the light sheet illumination to sensitive single molecule experiments in living tissue. Although the LSFM technique is applicable to various experiments and specimens, a fixed light sheet geometry limits the observable sample size. However, to obtain a larger field-of-view for bigger samples automatically lead to a larger light sheet thickness (**Figure 1.4**), since the depth-of-focus and the sheet thickness are related by the laws of Gaussian beam optics. Therefore it was required to tune the dimensions of the light sheet to achieve optimal image quality in each single experiment. The focused light sheet extension is inverse proportional to the incoming beam radius [25].

$$w_0 = \frac{2\lambda_0 f}{\pi\ n\ r} \tag{5.2}$$

w_0 is the focused 1/e²-beam radius, λ the used wavelength, f the focal length and r the incident beam radius. For a continuous and flexible adjustment of the focal extensions a cylindrical zoom beam expander had been utilized. In comparison to vertical and horizontal slit apertures used for beam alteration it had the advantages that no power loss or refractive effects occurred.

Furthermore, as explained above the previous instrument suffered from a lateral focal shift of the light sheet, while the sample was moved along the illumination axis (**Figure 5.2**). To prevent this an appropriate repositioning of the illumination objective had to be introduced, which could be achieved by a motorization of the illumination objective. The appropriately coupled movement of sample chamber and illumination objective can easily be software controlled. Moreover, the complete motorization of the sample chamber was an advancement, from which the experimental setup generally profited. The stability and usability of the complete setup was enhanced and any physical contact of the user during sample positioning was excluded.

In this third light sheet microscope the illumination optics were optimized for adjusting the light sheet dimensions at will. The key component in the illumination beam path was an afocal cylindrical zoom beam expander which allowed the continuous adjustment of the beam diameter along a single axis The cylindrical zoom beam expander was especially designed by ray tracing calculations. It had a zoom range from 1x to 6.3x and a compact build length of less than 160 mm. A special feature was the adjustment of the zoom factor with a single motor, because the moving optical elements were rigidly coupled together, unlike in a normal zoom objective, where the optical elements are moved independently and over unequal distances.

The performance of the cylindrical zoom objective was experimentally verified and in excellent agreement with the ray tracing calculations. The optical sectioning thickness could be adjusted from 2.4 to 6.6 µm with a NA 0.28 illumination objective. The range was further extended by changing the illumination lens. With an achromatic lens with an NA of 0.11 the optical sectioning ranged from 8.4 µm to 36 µm. This resulted in an available depth-of-focus range from 54 µm to 12.3 mm. The light sheet width could be adjusted with a vertical slit aperture from 20 µm to 120 µm. The advantages of the zoom unit were demonstrated in live biological specimen by imaging salivary gland cell nuclei of *Chironomus tentans* larvae. A small zoom factor provided a large field-of-view and large optical sectioning thickness which allowed a rapid location of the labeled polytene chromosome structure. After localization, imaging at a higher zoom factor restricted the field-of-view, what significantly improved the axial resolution, the image contrast and allowed a more detailed view of the structure.

5.4 Conclusions

Up to now, there had no experimental tools been available to perform single molecule measurements in biological, three dimensionally extended samples. The work in this thesis introduced a light sheet microscope to perform such experiments and some limitations of existing microscopy techniques, for example poor signal-to-noise-ratios, were overcome. The experimental realization of light sheet based fluorescence microscopy developed during the work for this thesis is capable of optical sectioning several hundred micrometer deep inside biological samples. Combined with the parallel image acquisition the introduced light sheet microscope is so far unmatched in terms of sensitivity and acquisition speed for higher penetration depths. It was possible to track fast single molecules in buffer solution which were not accessible to single molecule tracking before. Furthermore, the technique was applied to imaging the dynamics of single molecules with unprecedented speed and precision *in vivo* ~200 µm deep within a living heavily light scattering specimen. In this way the superior image quality of LSFM at high acquisition speeds compared to other microscopy techniques was demonstrated. Moreover, the method has great potential for 3D super resolution imaging of larger

living specimens (chapter 6.2). Another possible application, which becomes only now realizable, is 3D tracking of single molecules over long periods of time by continuously re-adjusting the focal position and thus keeping the molecule of interest in the field-of-view.

But a higher degree of flexibility in the light sheet dimensions was necessary for a truly versatile tool. With the implementation of the adjustable light sheet optics the microscope is not anymore limited to a single size range of samples and the light sheet thickness can be chosen for optimal imaging conditions. Three different experimental realizations of light sheet microscopes have been conceptualized, designed, and built during this thesis. Each instrument generation increased in complexity, but lead to an improved image quality and usability, finally succeeding in the aim to build a versatile and powerful tool. This realization of light sheet microscopy has the potential to reveal new dynamic single molecule interactions *in vivo* and enables new studies and experiments of intracellular processes.

6 Future developments

The previous chapters described advances in light sheet based fluorescence microscopy (LSFM) and its application to sensitive single molecule experiments in living tissue. Certainly the light sheet illumination principle is under continuous development and further improvements can be envisioned.

6.1 Multi-angle illumination light sheet microscopy

A common problem from which all light microscopes suffer is the interaction of the excitation light with the sample, especially in inhomogeneous samples. (e.g. tissue, embryos). However, because of the illumination from the side optical artifacts due to scattering or absorption of the light are more pronounced in LSFM, causing stripes and shadows along the illumination axis. Obviously, longer optical pathways within the sample aggravate the situation. These stripes make it difficult to accurately analyze images generated by light sheet microscopy. An even illumination of the field-of-view can be achieved by pivoting the light sheet in the detection focal plane (**Figure 6.1**)[38].

To realize this experimentally a high-speed galvanic mirror can be inserted in the illumination pathway [38]. The light sheet is scanned over an angle of 10° with a frequency of more than 1 kHz, thereby shadowing should be significantly reduced at typical image exposure times of 5-20 ms. This can be further improved by the additional application of a stripe reducing filter, such as a appropriate wavelet filter [85]. The combination of a hardware and software stripe reduction should render the final images stripe free.

There are further challenges for LSFM imaging in larger, dense samples: The attenuation of the excitation light along the illumination axis and a loss of optical sectioning thickness along the illumination axis. The excitation light is partially absorbed during its propagation through the sample, which results in a loss of excitation power and therefore fluorescence deeper in the sample. Moreover, light might be scattered along the detection axis z, which will lead to a inhomogeneous illumination profile. Ultimately this results in a widening of the light sheet and a loss of optical sectioning. Both effects lead to a progressive image degradation from the entry site along the illumination axis. This degradation can be counteracted by illuminating the sample with two partially overlapping counter-propagating beams hitting the sample from both sides [38,43]. To implement this in the currently realized LSFM setup a second, identical illumination pathway has to be build and the sample holder must be optical accessible from two opposite sides.

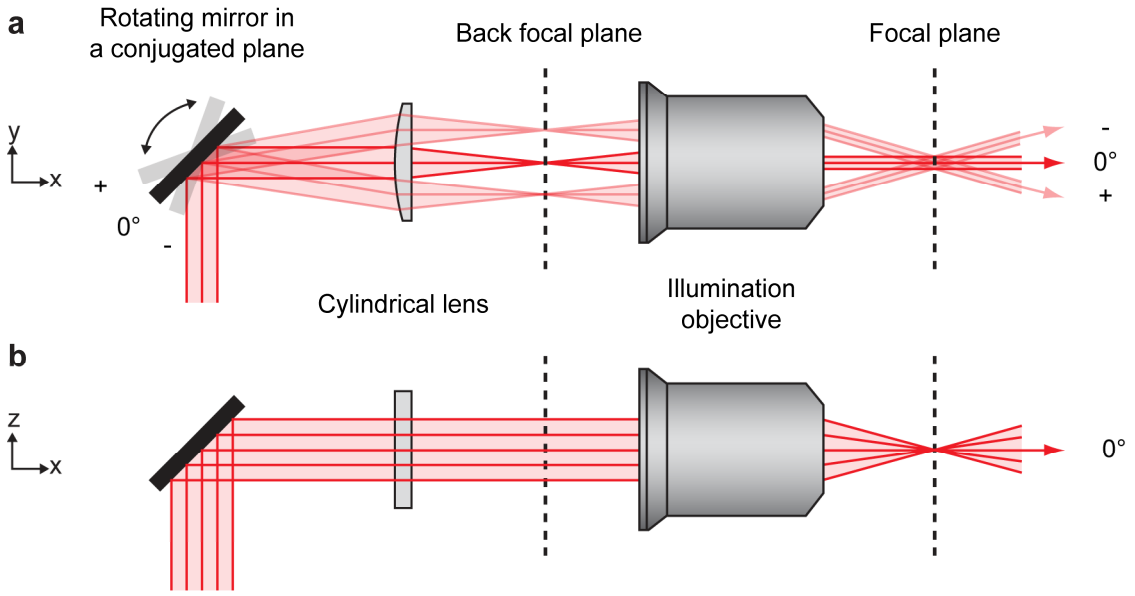

Figure 6.1 Multi angle light sheet illumination. (**a**) Fast pivoting of the light sheet in the x-y plane and subsequent focusing by a cylindrical lens into the back focal plane of the illumination objective results in a collimated multi angle illumination in the focal plane. The pivoting mirror has to be telecentrically placed in a conjugated plane to the focal plane. (**b**) Along the x-z plane the mirror stays fixed and the collimated beam is focused in the focal plane, thus generating the light sheet.

6.2 Super-resolution experiments with light sheet microscopy

The spatial resolution of far-field optical microscopy, classically limited by the diffraction of light to ~250 nm, is substantially larger than typical molecular length scales (1 - 50 nm), leaving many biological problems beyond the reach of light microscopy. To overcome this limit, a new type of high resolution light microscopy has been developed. Photoactivated localization microscopy (PALM) [88] and stochastic optical reconstruction microscopy (STORM) [3] take advantage of the fact that single molecules can be localized with sub-diffraction limited precision. Super resolution microscopy uses stochastic activation or switching of fluorescent probes to temporally separate otherwise spatially overlapping diffraction limited images of individual molecules. The position of individual molecules can be localized with sub-diffraction resolution and from these positions high-resolution images can be reconstructed. Using this concept, three-dimensional, multicolor fluorescence imaging of molecular complexes, cells and tissues with ~20 nm lateral and ~50 nm axial resolution can be achieved [89].

Super-resolution microscopy requires excellent contrast to achieve such high resolutions, because the localization precision of an individual molecule is strongly

dependent on the signal-to-noise-ratio. For this reason, the concept has been only applied to systems close to a surface utilizing optical sectioning illumination techniques like total internal reflection microscopy (TIRF) [21] or highly inclined laminated sheet microscopy (HILO) [22,23]. Although some studies imaged biological structures at super-resolution in three dimensions, they severely lacked depth-of-focus and the axial observation distance was limited to a few µm, due to the illumination schemes used [90,91,92]. So far the studies avoided the optical challenges of three dimensional imaging in extended biological samples.

Light sheet microscopy is an ideal illumination technique to realize super resolution imaging in three dimensionally extended samples. It provides the necessary optical sectioning effect and thus an excellent single molecule detection sensitivity in three dimensions, a key prerequisite for precise single molecule localization in stochastic super resolution microscopy.

Preliminary experiments demonstrated the high potential of this strategy by imaging the polytene chromosomes in the salivary gland cell nucleus *of C.tentans* larvae (see Chapter 4.3.4). A specific labeling strategy was used to achieve activation and localization. The fluorophore ReAsH only becomes fluorescent when it binds to a tetracysteine motif. (**Figure 6.2a**) This feature allows sensitive localization of proteins containing the tetracysteine-tag by fluorescence microscopy. Combined with photo-bleaching, like in PALM, it can be utilized for stochastic imaging.

Hrp36 containing the tetracysteine binding motif was microinjected in the salivary gland cells of the *C.tentans* larvae. Hrp36 was bound to the nascent mRNA within minutes (see Chapter 3.3.4). Subsequent microinjection of the labeling reagent ReAsH allowed sensitive localization of the hrp36 proteins since the dye became only excitable when it was bound to the recombinant protein (**Figure 6.2b**). The idea was, that the hrp36 was imaged when it was bound to the mRNA ideally at the transcription site or the polytene chromosomes. At this places the hrp36 proteins were densely bound, so that several hundred hrp36 proteins could be found within the area of one resolution limit (~ 1 µm²). After excitation of a bound ReAsH fluorophore the hrp36 became visible. The fluorophore was then rapidly photo-bleached and the hrp36 returned to a dark state. A neighboring hrp36 protein was then imaged upon binding of a ReAsH fluorophore. Optionally, but more unlikely, the photo-bleached fluorophore can be replaced by a new fluorophore. This process was repeated many times until enough events were imaged (typically several thousand events). The procedure is a statistical process and on average only a single hrp36 protein should be visible within the area of one resolution limit at the same time. This required a fine balance of the concentrations of the available fluorophores and the proteins with a tetracysteine binding motif.

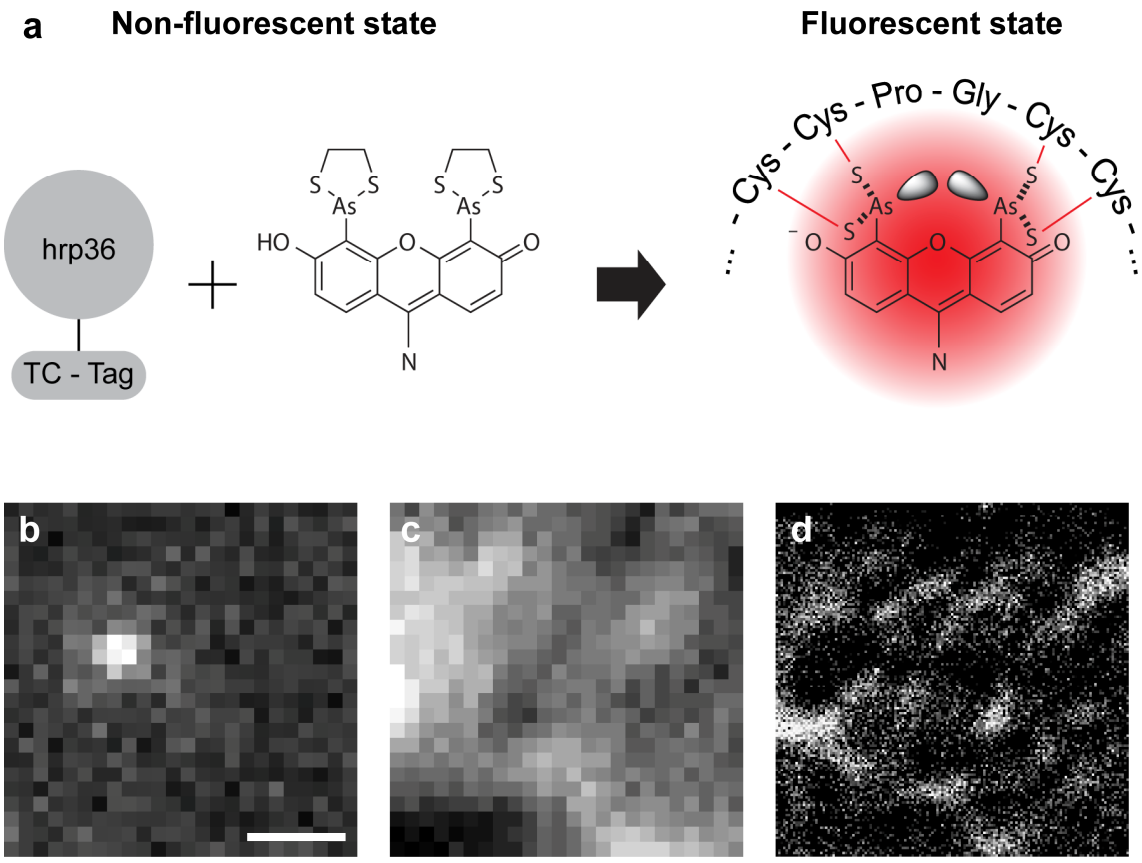

Figure 6.2 Super-resolution imaging with ReAsH labeling in the cell nucleus of salivary gland cells. (**a**) Hrp36 carries the tetracysteine motif (TC) and becomes fluorescent upon binding to the ReAsH fluorophore. (**b**) Imaged single fluorescent hrp36 protein inside the salivary gland cell nucleus of the *C.tentans* larvae. Localization of thousands of such images allowed subsequent high resolution reconstruction. Scale bar, 1 µm (**c**) Summed image stack resulted in spatially overlapping images of individual hrp36 proteins. (**d**) Reconstructed image of thousands of individual hrp36 localizations like in (b). The typical polytene band structure became visible.

The final image could be subsequently reconstructed from all individual hrp36 localizations. (**Figure 6.2d**). The reconstructed image showed the polytene band structure as it was expected. However, these were initial steps and no true sub-diffraction resolution was achieved. For this more care has to be taken in terms of drift correction and stabilization of the sample, which limited in these experiments the achievable average localization accuracy.

Super-resolution fluorescence microscopy allows to image molecular interactions in cells and cell-cell interactions in tissue at the nanometer scale. Light sheet microscopy is a promising illumination technique for super-resolution imaging in three dimensions. In the near future the imaging of live cells and tissue in three dimensions with a resolution at the true molecular length scale might be possible due to the virtues of light sheet microscopy.

Literature

[1] Pawley JB (2006) *Handbook of confocal microscopy*. Berlin: Springer.

[2] Willig KI, Kellner RR, Medda R, Hein B, et al. (2006) *Nanoscale resolution in GFP-based microscopy*. Nature Methods 3: 721-723.

[3] Bates M, Huang B, Zhuang X (2008) *Super-resolution microscopy by nanoscale localization of photo-switchable fluorescent probes*. Curr Opin Chem Biol 12: 505-514.

[4] Giancoli DC (2000) *Physics*. Prentice Hall: Pearson Education.

[5] Dobrucki JW, Feret D, Noatynska A (2007) *Scattering of exciting light by live cells in fluorescence confocal imaging: phototoxic effects and relevance for FRAP studies*. Biophys J 93: 1778-1786.

[6] Sprague BL, McNally JG (2005) *FRAP analysis of binding: proper and fitting*. Trends Cell Biol 15: 84-91.

[7] Thompson RE, Larson DR, Webb WW (2002) *Precise nanometer localization analysis for individual fluorescent probes*. Biophys J 82: 2775-2783.

[8] Pampaloni F, Stelzer EH, Leicht S, Marcello M (2010) *Madin-Darby canine kidney cells are increased in aerobic glycolysis when cultured on flat and stiff collagen-coated surfaces rather than in physiological 3-D cultures*. Proteomics 10: 3394-3413.

[9] Wang X, Wohland T, Korzh V (2010) *Developing in vivo biophysics by fishing for single molecules*. Dev Biol 347: 1-8.

[10] Abbott A (2003) *Cell culture: biology's new dimension*. Nature 424: 870-872.

[11] Brandenburg B, Zhuang X (2007) *Virus trafficking - learning from single-virus tracking*. Nat Rev Microbiol 5: 197-208.

[12] Baker A, Sauliere A, Dumas F, Millot C, et al. (2007) *Functional membrane diffusion of G-protein coupled receptors*. Eur Biophys J 36: 849-860.

[13] Hilario J, Kowalczykowski SC (2010) *Visualizing protein-DNA interactions at the single-molecule level*. Curr Opin Chem Biol 14: 15-22.

[14] Kues T (2001) *Visualisierung einzelner Proteinmoleküle und Analyse ihrer Trajektorien in intakten Zellkernen mittels Weitfeld-Fluoreszenzmikroskopie*. Bremen: Universität Bremen.

[15] Haustein E, Schwille P (2007) *Fluorescence correlation spectroscopy: novel variations of an established technique*. Annu Rev Biophys Biomol Struct 36: 151-169.

[16] Joo C, Balci H, Ishitsuka Y, Buranachai C, et al. (2008) *Advances in single-molecule fluorescence methods for molecular biology*. Annu Rev Biochem 77: 51-76.

[17] Grunwald D, Spottke B, Buschmann V, Kubitscheck U (2006) *Intranuclear binding kinetics and mobility of single native U1 snRNP particles in living cells*. Mol Biol Cell 17: 5017-5027.

[18] Lommerse PH, Snaar-Jagalska BE, Spaink HP, Schmidt T (2005) *Single-molecule diffusion measurements of H-Ras at the plasma membrane of live cells reveal microdomain localization upon activation*. J Cell Sci 118: 1799-1809.

[19] Schaaf MJ, Koopmans WJ, Meckel T, van Noort J, et al. (2009) *Single-molecule microscopy reveals membrane microdomain organization of cells in a living vertebrate*. Biophys J 97: 1206-1214.

[20] Siebrasse JP, Veith R, Dobay A, Leonhardt H, et al. (2008) *Discontinuous movement of mRNP particles in nucleoplasmic regions devoid of chromatin*. Proc Natl Acad Sci U S A 105: 20291-20296.

[21] Axelrod D (2001) *Total internal reflection fluorescence microscopy in cell biology*. Traffic 2: 764-774.

[22] Konopka CA, Bednarek SY (2008) *Variable-angle epifluorescence microscopy: a new way to look at protein dynamics in the plant cell cortex*. Plant J 53: 186-196.

[23] Tokunaga M, Imamoto N, Sakata-Sogawa K (2008) *Highly inclined thin illumination enables clear single-molecule imaging in cells*. Nat Methods 5: 159-161.

[24] Lord SJ, Lee HL, Moerner WE (2010) *Single-molecule spectroscopy and imaging of biomolecules in living cells*. Anal Chem 82: 2192-2203.

[25] Saleh BEA, Teich MC (2007) *Fundamentals of Photonics*. West Sussex: Wiley&Sons.

[26] Huisken J, Stainier DY (2009) *Selective plane illumination microscopy techniques in developmental biology*. Development 136: 1963-1975.

[27] Vermot J, Fraser SE, Liebling M (2008) *Fast fluorescence microscopy for imaging the dynamics of embryonic development*. Hfsp J 2: 143-155.

[28] Verveer PJ, Swoger J, Pampaloni F, Greger K, et al. (2007) *High-resolution three-dimensional imaging of large specimens with light sheet-based microscopy*. Nat Methods 4: 311-313.

[29] Keller PJ, Schmidt AD, Santella A, Khairy K, et al. (2010) *Fast, high-contrast imaging of animal development with scanned light sheet-based structured-illumination microscopy*. Nat Methods 7: 637-642.

[30] Jahrling N, Becker K, Dodt HU (2009) *3D-reconstruction of blood vessels by ultramicroscopy*. Organogenesis 5: 145-148.

[31] Engelbrecht CJ, Stelzer EH (2006) *Resolution enhancement in a light-sheet-based microscope (SPIM)*. Opt Lett 31: 1477-1479.

[32] Reynaud EG, Krzic U, Greger K, Stelzer EH (2008) *Light sheet-based fluorescence microscopy: more dimensions, more photons, and less photodamage*. Hfsp J 2: 266-275.

[33] Krzic U (2009) *Multiple-view microscopy with light-sheet based fluorescence microscope*. Heidelberg: Ruperto-Carola Universität Heidelberg.

[34] Siedentopf H, Zsigmondy R (1903) *Über die Sichtbarmachung und Größenbestimmungvon ultramikroskopischer Teilchen, mit der besonderen Anwendung auf Goldrubingläser*. Annalen der Physik 4: 1-39.

[35] Huisken J, Swoger J, Del Bene F, Wittbrodt J, et al. (2004) *Optical sectioning deep inside live embryos by selective plane illumination microscopy*. Science 305: 1007-1009.

[36] Scherz PJ, Huisken J, Sahai-Hernandez P, Stainier DY (2008) *High-speed imaging of developing heart valves reveals interplay of morphogenesis and function*. Development 135: 1179-1187.

[37] Wohland T, Shi X, Sankaran J, Stelzer EH (2010) *Single plane illumination fluorescence correlation spectroscopy (SPIM-FCS) probes inhomogeneous three-dimensional environments*. Opt Express 18: 10627-10641.

[38] Huisken J, Stainier DY (2007) *Even fluorescence excitation by multidirectional selective plane illumination microscopy (mSPIM)*. Opt Lett 32: 2608-2610.

[39] Keller PJ, Pampaloni F, Lattanzi G, Stelzer EH (2008) *Three-dimensional microtubule behavior in Xenopus egg extracts reveals four dynamic states and state-dependent elastic properties*. Biophys J 95: 1474-1486.

[40] Keller PJ, Pampaloni F, Stelzer EH (2006) *Life sciences require the third dimension*. Curr Opin Cell Biol 18: 117-124.

[41] Keller PJ, Schmidt AD, Wittbrodt J, Stelzer EH (2008) *Reconstruction of zebrafish early embryonic development by scanned light sheet microscopy*. Science 322: 1065-1069.

[42] Neil MA, Juskaitis R, Wilson T (1997) *Method of obtaining optical sectioning by using structured light in a conventional microscope*. Opt Lett 22: 1905-1907.

[43] Dodt HU, Leischner U, Schierloh A, Jahrling N, et al. (2007) *Ultramicroscopy: three-dimensional visualization of neuronal networks in the whole mouse brain*. Nat Methods 4: 331-336.

[44] Holekamp TF, Turaga D, Holy TE (2008) *Fast three-dimensional fluorescence imaging of activity in neural populations by objective-coupled planar illumination microscopy*. Neuron 57: 661-672.

[45] Herbert SP, Huisken J, Kim TN, Feldman ME, et al. (2009) *Arterial-venous segregation by selective cell sprouting: an alternative mode of blood vessel formation*. Science 326: 294-298.

[46] Leischner U, Zieglgansberger W, Dodt HU (2009) *Resolution of ultramicroscopy and field of view analysis*. PLoS One 4: e5785.

[47] Ritter JG, Veith R, Siebrasse JP, Kubitscheck U (2008) *High-contrast single-particle tracking by selective focal plane illumination microscopy*. Opt Express 16: 7142-7152.

[48] Siebrasse JP, Grunwald D, Kubitscheck U (2007) *Single-molecule tracking in eukaryotic cell nuclei*. Anal Bioanal Chem 387: 41-44.

[49] Voie AH, Burns DH, Spelman FA (1993) *Orthogonal-Plane Fluorescence Optical Sectioning - 3-Dimensional Imaging of Macroscopic Biological Specimens*. Journal of Microscopy-Oxford 170: 229-236.

[50] Buytaert JA, Dirckx JJ (2007) *Design and quantitative resolution measurements of an optical virtual sectioning three-dimensional imaging technique for biomedical specimens, featuring two-micrometer slicing resolution*. J Biomed Opt 12: 014039.

[51] Alt W (2002) *An objective lens for efficient fluorescence detection of single atoms*. Optik 113: 142-144.

[52] Millonni PW, Eberly JH (1989) *Lasers*. West Sussex: Wiley&Sons.

[53] Born M, Wolf E (1997) *Principles of Optics*. Cambridge: Cambridge University Press.

[54] Wright D, Greve P, Fleischer J, Austin L (1992) *Laser beam width, divergence and beam propagation factor - an international standardization approach*. Optical and Quantum Electronics 24: S993-S1000.

[55] Engelbrecht CJ, Greger K, Reynaud EG, Krzic U, et al. (2007) *Three-dimensional laser microsurgery in light-sheet based microscopy (SPIM)*. Opt Express 15: 6420-6430.

[56] Kues T, Dickmanns A, Luhrmann R, Peters R, et al. (2001) *High intranuclear mobility and dynamic clustering of the splicing factor U1 snRNP observed by single particle tracking*. Proc Natl Acad Sci U S A 98: 12021-12026.

[57] Grunwald D, Hoekstra A, Dange T, Buschmann V, et al. (2006) *Direct observation of single protein molecules in aqueous solution*. Chemphyschem 7: 812-815.

[58] Ritter JG, Veith R, Veenendaal A, Siebrasse JP, et al. (2010) *Light sheet microscopy for single molecule tracking in living tissue*. PLoS One 5: e11639.

[59] Buytaert JA, Dirckx JJ (2009) *Tomographic imaging of macroscopic biomedical objects in high resolution and three dimensions using orthogonal-plane fluorescence optical sectioning*. Appl Opt 48: 941-948.

[60] Axelrod D (1981) *Cell-substrate contacts illuminated by total internal reflection fluorescence*. J Cell Biol 89: 141-145.

[61] Friedrich M, Nozadze R, Gan Q, Zelman-Femiak M, et al. (2009) *Detection of single quantum dots in model organisms with sheet illumination microscopy*. Biochem Biophys Res Commun 390: 722-727.

[62] Visa N, Alzhanova-Ericsson AT, Sun X, Kiseleva E, et al. (1996) *A pre-mRNA-binding protein accompanies the RNA from the gene through the nuclear pores and into polysomes*. Cell 84: 253-264.

[63] Ermolayev V, Friedrich M, Nozadze R, Cathomen T, et al. (2009) *Ultramicroscopy reveals axonal transport impairments in cortical motor neurons at prion disease*. Biophys J 96: 3390-3398.

[64] http://www.plosone.org/article/info%3Adoi%2F10.1371%2Fjournal.pone.0011639

[65] Kues T, Peters R, Kubitscheck U (2001) *Visualization and tracking of single protein molecules in the cell nucleus*. Biophys J 80: 2954-2967.

[66] Watson JD, Crick FH (1953) *Molecular structure of nucleic acids; a structure for deoxyribose nucleic acid*. Nature 171: 737-738.

[67] Case ST, Daneholt B (1978) *The size of the transcription unit in Balbiani ring 2 of Chironomus tentans as derived from analysis of the primary transcript and 75 S RNA*. J Mol Biol 124: 223-241.

[68] Daneholt B (2001) *Assembly and transport of a premessenger RNP particle*. Proc Natl Acad Sci U S A 98: 7012-7017.

[69] Wieslander L (1994) *The Balbiani ring multigene family: coding repetitive sequences and evolution of a tissue-specific cell function*. Prog Nucleic Acid Res Mol Biol 48: 275-313.

[70] Daneholt B (2001) *Packing and delivery of a genetic message*. Chromosoma 110: 173-185.

[71] Singh OP, Bjorkroth B, Masich S, Wieslander L, et al. (1999) *The intranuclear movement of Balbiani ring premessenger ribonucleoprotein particles*. Exp Cell Res 251: 135-146.

[72] Wurtz T, Kiseleva E, Nacheva G, AlzhanovaEricsson A, et al. (1996) *Identification of two RNA-binding proteins in balbiani ring premessenger ribonucleoprotein granules and presence of these proteins in specific subsets of heterogeneous nuclear ribonucleoprotein particles*. Molecular and Cellular Biology 16: 1425-1435.

[73] Richter K, Nessling M, Lichter P (2008) *Macromolecular crowding and its potential impact on nuclear function*. Biochim Biophys Acta 1783: 2100-2107.

[74] Berg H (1993) *Random Walks in Biology*. Princton: Princeton Universiy Press.

[75] Gorisch SM, Wachsmuth M, Toth KF, Lichter P, et al. (2005) *Histone acetylation increases chromatin accessibility*. J Cell Sci 118: 5825-5834.

[76] Andersson KM, Hovmoller S (1998) *The average atomic volume and density of proteins*. Zeitschrift Fur Kristallographie 213: 369-373.

[77] Ulbrich MH, Isacoff EY (2007) *Subunit counting in membrane-bound proteins*. Nat Methods 4: 319-321.

[78] Müller CB, Loman A, Pacheco V, Koberling F, et al. (2008) *Precise measurement of diffusion by multi-color dual-focus fluorescence correlation spectroscopy*. Epl 83: 46001.

[79] Ritter JG, Spille JH, Kaminski T, Kubitscheck U (2010) *A cylindrical zoom lens unit for adjustable optical sectioning in light sheet microscopy*. Biomed Opt Express 2: 185-193.

[80] Jahrling N, Becker K, Schonbauer C, Schnorrer F, et al. (2010) *Three-dimensional reconstruction and segmentation of intact Drosophila by ultramicroscopy*. Front Syst Neurosci 4: 1.

[81] Preibisch S, Saalfeld S, Schindelin J, Tomancak P (2010) *Software for bead-based registration of selective plane illumination microscopy data*. Nat Methods 7: 418-419.

[82] Reynaud EG, Tomancak P (2010) *Meeting report: first light sheet based fluorescence microscopy workshop*. Biotechnol J 5: 798-804.

[83] Saghafi S, Becker K, Jahrling N, Richter M, et al. (2010) *Image enhancement in ultramicroscopy by improved laser light sheets*. J Biophotonics.

[84] Winterot J, Huettel P (2005) Microscope with an afocal zoom system. In: AG CZ, editor.

[85] Munch B, Trtik P, Marone F, Stampanoni M (2009) *Stripe and ring artifact removal with combined wavelet--Fourier filtering*. Opt Express 17: 8567-8591.

[86] Huang B, Wang W, Bates M, Zhuang X (2008) *Three-dimensional super-resolution imaging by stochastic optical reconstruction microscopy*. Science 319: 810-813.

[87] Ritter JG (2006) *Fluoreszenzmikroskopische Aufnahme optischer Schnitte durch selektive Beleuchtung der Objektebene*. Bonn: Rheinische Friedrich-Wilhelms-Universität Bonn.

[88] Shroff H, White H, Betzig E (2008) *Photoactivated localization microscopy (PALM) of adhesion complexes*. Curr Protoc Cell Biol Chapter 4: Unit 4 21.

[89] Schermelleh L, Heintzmann R, Leonhardt H (2010) *A guide to super-resolution fluorescence microscopy*. J Cell Biol 190: 165-175.

[90] Huang B, Jones SA, Brandenburg B, Zhuang X (2008) *Whole-cell 3D STORM reveals interactions between cellular structures with nanometer-scale resolution*. Nat Methods 5: 1047-1052.

[91] Shtengel G, Galbraith JA, Galbraith CG, Lippincott-Schwartz J, et al. (2009) *Interferometric fluorescent super-resolution microscopy resolves 3D cellular ultrastructure*. Proc Natl Acad Sci U S A 106: 3125-3130.

[92] Juette MF, Gould TJ, Lessard MD, Mlodzianoski MJ, et al. (2008) *Three-dimensional sub-100 nm resolution fluorescence microscopy of thick samples*. Nat Methods 5: 527-529.

Acknowledgments

First and foremost I offer my sincerest gratitude to my supervisor, Prof. Ulrich Kubitscheck, who has supported me throughout my thesis with his patience and knowledge and gave me the room to work in my own way. One simply could not imagine oneself a better or friendlier supervisor.
I gratefully acknowledge Prof. Rudolf Merkel for his advice, fascinating discussions and for taking over the co-supervision of the thesis. In addition, I am grateful to Prof. Jörn Piel and Prof. Thorsten Lang for their kindness to become members of the thesis committee.
I would like to acknowledge the support from LaVision BioTec, especially the help of Dr. Heinrich Spiecker and Volker Andresen.

In my daily work I have been honored with a friendly and cheerful group of fellow students. Some of them I call my friends. One of them is Andreas Veenendaal, with whom I had the honor to share the office. Thanks for the pleasant time and the hilarious discussions. Together we were a great team having our successes in the lab with our "sensible tools", as well as in various competitions. I owe my deepest gratitude to Katharina Scherer as a trustworthy, kick-ass friend, who helped me to navigate through some rough waters. Her humor and directness have been a constant source of cheer and comfort. I wish to thank Jan-Hendrik Spille, a supportive lab mate and "boßeln"-importer, who is never shy for a decent competition. Unforgettable are our controversial debates about god and the world during lunch time. It is a pleasure to thank Tim Kaminski, who was not only great help with the biological samples, but he also cheered me up with his always positive, uncomplicated attitude. His endless stream of ideas was always inspiring and lead to long entertaining sessions together with Katharina, Jan and Andreas in the "career center". To all four I am thankful, that in the midst of all their activity they accepted to be members of the reading committee.
Collective acknowledgments are also owed to my colleagues in the workgroup biophysical chemistry, whose presence refreshed, helped and created memorable moments. In particular I would like to thank Jan-Peter Siebrasse.

Where would I be without my family? My parents deserve special mention for their infinite support. My Father in the first place is the person who put the fundament of my learning character, supporting my intellectual pursuit ever since I was a child. My Mother is the one who sincerely raised me with her caring and gently love. Michael, thanks for being a supportive and caring brother.

Words fail me to express my gratefulness to my wife Kirsten whose dedication,
love and persistent confidence in me, has taken the load off my shoulders.

Eidesstattliche Erklärung

Hiermit erkläre ich, dass ich die vorliegende Arbeit ohne unzulässige Hilfe Dritter und ohne Benutzung anderer als der angegebenen Hilfsmittel angefertigt habe. Die aus anderen Quellen direkt oder indirekt übernommenen Daten und Konzepte sind unter Angabe der Quelle gekennzeichnet.

Die Arbeit wurde bisher weder im In- noch im Ausland in gleicher oder ähnlicher Form einer anderen Prüfungsbehörde vorgelegt.

Bonn März 2011

Jörg Ritter